THEORETICAL AND EXPERIMENTAL INVESTIGATIONS ON TURBINE AERODYNAMICS AND HEAT TRANSFER

PART I: DEVELOPMENT OF A NEW UNSTEADY TRANSITION MODEL BASED ON UNIVERSAL INTERMITTENCY FUNCTION

PART II: EXPERIMENTAL AND NUMERICAL INVESTIGATIONS OF FILM-COOLING EFFECTIVENESS ON A HIGHLY LOADED TURBINE BLADE

A Dissertation

by

ALI NIKPARTO

Submitted to the Office of Graduate and Professional Studies of
Texas A&M University
In partial fulfillment of the requirements for the degree of

DOCTOR OF PHILOSOPHY

Chair of Committee,	Meinhard T. Schobeiri
Committee Members,	Junuthula N. Reddy
	Je-Chin Han
	Jean-Luc Guermond
Head of Department,	Andreas Polycarpou

August 2018

Major Subject: Mechanical Engineering

ABSTRACT

The flow around a gas turbine blade is inherently three-dimensional and based on the Re-number and the blade geometry, it may be laminar, transitional or turbulent. The blade surfaces are subject to periodic unsteady wakes that originate from the upstream stator/rotor rows. The wakes with their highly vortical cores impinge on the downstream blade surfaces and cause an intermittent transition of the boundary layer from laminar to turbulent. The intermittent behavior of the boundary layer under periodic wake flow condition is characterized in several publications from TPFL (Turbomachinery Performance and Flow Research Lab). Intermittency at each location varies between a maximum and a minimum value at different times. Maximum intermittency corresponds to the intermittent behavior of the flow inside the blade boundary layer once it is subjected to the wake vortical core and minimum intermittency characterizes the nature of the boundary layer when it is subject to non-turbulent flow region between the wakes. The correlation between minimum, maximum and instantaneous intermittencies is best described by the universal intermittency function that has a Gaussian distribution. In the current study, a transport equation for intermittency has been derived from previously obtained experimental measurements. This transport equation is revisited for the curvilinear coordinate system and was implemented in a RANS solver to model the transient behavior of the flow on the suction surface of a turbine blade. It was later integrated with a turbulence model, and the results were validated against experimental measurements and transitional-SST turbulence model. The benchmark data, used for derivation and validation, were obtained in the cascade facility at TPFL. The facility simulates the periodic wake flow by moving rods attached to two parallel timing belts in

front of the blade cascade. All calculations were conducted at Reynolds number of 414,000.

Also, another effort has been made to measure film-cooling effectiveness on the suction and pressure surfaces of a low-pressure turbine blade utilizing the same cascade facility. Low-pressure turbine blades are not necessarily exposed to critically high temperatures and for that reason, cooling technologies are not very common in these stages of the engine. Yet, the film-cooling experiments were designed with the purpose of understanding the effects of the underlying physics of the transitional flow on film-cooling effectiveness. The flow around this turbine blade has unique characteristics. The flow regime is transitional and, especially in off-design conditions, it is often accompanied by flow separation and rapid change of pressure gradient as well as unsteady incoming wakes that could impinge on the blade surface and penetrate the boundary layer. These flow features add to the level of complexity of this case. For the experiments, the flow coefficient is maintained at 0.8, and the incoming wakes in experiments have a reduced frequency of 3.18. Film-cooling effectiveness under periodic unsteady flow condition was studied using Pressure-Sensitive Paint. Experiments were performed at Reynolds number of 150,000 and blowing ratio of 1, based on equal mass flux distribution. It was determined that HTC and FCE behave in opposite manners for the most part. This behavior is justified from turbulence intensity and velocity fluctuation perspective. Also, unsteady wakes show opposite effects on suction and pressure sides of the blade.

DEDICATION

I dedicate this work to my lovely wife, Niloufar, who has always been there for me and has supported me throughout this journey. I also would like to dedicate my dissertation to my dear family, my mother, father, sister and my brother without whom I would never be the man that I am today.

ACKNOWLEDGMENTS

I would like to thank my committee chair, Dr. Schobeiri, and my committee members, Dr. Han, Dr. Reddy, and Dr. Guermond for their guidance and support throughout this research.

I also would like to thank my colleagues and the department faculty and staff at Texas A&M University for making my time here a great experience.

Finally, I would like to thank my parents for their encouragement and my wife for her patience and love.

CONTRIBUTORS AND FUNDING SOURCES

This work was supervised by a dissertation committee consisting of Professor M.T. Schobeiri (advisor), Professor J.C Han, and Professor J.N Reddy of the department of Mechanical Engineering and Professor J.L Guermond of the department of Mathematics.

The experimental data presented in Chapter 6 was gathered by Dr. Burak Ozturk and were published in 2007. The data analyzed in Chapter 12 was partially produced and analyzed by Mr. Tyler Rice of the department of Mechanical Engineering. The calibration code for five-hole probe included in the Appendix is produced by Mr. Hicham Chibli. All other works conducted for this dissertation was completed by the student independently.

The graduate study was supported by a professorship from Texas A&M University and Graduate Teaching Fellowship from Department of Engineering, Texas A&M University. There are no outside funding contributions to acknowledge related to the research and compilation of this document.

NOMENCLATURE

c	Chord length
c_{ax}	Axial chord
c_p	Thermal heat capacity at constant pressure
C	Concentration
D	Mass diffusion
D	Van driest damping function
D_R	Rod diameter
F_{kl}	Klebanhoff intermittency function
g	Gravitational acceleration
h_b	Blade height
I	Light intensity
k	Turbulence kinetic energy
k	Thermal conductivity
Le	Lewis number
l_m	Mixing length
L_{ss}	Suction surface length
M	Blowing ratio
P	Pressure
Re	Reynolds number
$Re\text{-}\theta$	Momentum thickness Reynolds number
S_B	Blade spacing
S_R	Rod spacing

t	Time
T	Temperature
Tu_{in}	Inlet turbulence intensity
U	Velocity
U_w	Belt velocity(wake generator velocity)
V_{ax}	Axial velocity
W	Nozzle inlet width
y	Vertical distance from the wall
y+	Dimensionless wall distance

Greek letters

α_1	Inlet flow angle
α_2	Outlet flow angle
α_d	Thermal diffusivity
γ	Intermittency function
Γ	Universal intermittency function
δ	Boundary layer height
δ	Kronecker delta function
ε	Dissipation
ε_m	Turbulent mass diffusivity
ε_t	Turbulent thermal diffusivity
ζ	Non-dimensionalized lateral distance
η	FCE

μ	Viscosity
ξ	Wake parameter
ξ_1	Streamwise direction
ξ_2	Blade normal direction
ρ	Density
σ	Cascade solidity
$\boldsymbol{\Phi}$	Flow coefficient
ϕ	Cascade angle
ω	Specific dissipation
Ω	Reduced frequency
Ω	Vorticity

Subscripts

∞	Pertaining to freestream
aw	Adiabatic wall
blk	Black
c	Coolant
e	Edge of the BL
e	end
f	Film
m	mainstream
mix	Air+Nitrogen
N_2	Nitrogen

ref	Reference
s	start
t	Turbulent
t	total
w	Wall

Abbreviation

CCD	Charged coupled device
CTA	Constant temperature anemometry
DNS	Direct numerical simulation
FCE	Film-cooling effectiveness
FSTI	Freestream turbulence intensity
HPT	High-pressure turbine
HRN	High Reynolds number
HTC	Heat transfer coefficient
LE	Leading edge
LES	Large eddy simulation
LPT	Low-pressure turbine
LRN	Low Reynolds number
PSP	Pressure sensitive paint
PS	Pressure side
RANS	Reynolds averaged Navier Stokes
SS	Suction side
TE	Trailing edge

TPFL Turbomachinery Performance and Flow research Lab

TABLE OF CONTENTS

LIST OF FIGURES

Page

LIST OF TABLES

Page

1 DEVELOPMENT OF NEW TRANSITION MODEL

INTRODUCTION AND LITERATURE REVIEW

The world is now experiencing a dramatic demand for new sources of energy. According to International Energy Outlook 2013 [3], world energy consumption will increase by 56% by 2040. Although renewable energies and Nuclear energy are the fastest-growing energy sources, fossil fuels will remain as the primary source of energy for future generations. According to projections, about 80% of energy demand in 2040 will be supplied by fossil fuels. Energy engineers are certainly the backbone of every society and crucial to the future of energy supply chain as they have to carry the burden on their shoulders to meet the needs in time and to prevent a probable energy crisis. Aside from energy crisis, the environmental issues surrounding conventional and modern energy conversions, have also pushed engineers to move into the direction of clean and efficient energy extraction and conversion methods. Gas turbine, as one of the most important components of energy conversion cycles, plays a large role in the modern world, from generating power for communities to supplying thrust for aircrafts. Engineers and researchers are always attempting to maximize the efficiency of gas turbine engines and to increase the output energy. However, there are numerous challenging technical issues to be resolved.

Although the concept of Gas Turbine Engine is not new (the first patent of gas turbine engine was submitted in 1791 [4]) it did not become operational until 1939 when Brown Boveri company manufactured the world's first gas turbine for power generation purposes [5]. Ever since gas turbine engineers have tried to come up with new designs to push the maximum efficiency of the engine to around 40%. Increasing demand for power

and the limited amount of fossil fuel resources along with environmental concerns have been a driving force to design and manufacture a more efficient engine. Higher efficiency can be obtained by increasing the turbine inlet temperature.

For aero-engines, the thrust/weight ratio plays an equally important role. The weight of the turbine section constitutes a major portion of the entire engine weight causing the engine designer to reduce the blade numbers. Researchers have proven that reduction in blade count can be achieved while turbine blades have kept their performance status quo [6, 7]. This reduction is beneficial in numerous ways. To name a few, we can point out to reduction in weight and reduction of manufacturing as well as maintenance cost. Turbine blades could potentially experience a variation of Reynolds number depending on the operating condition. Also reduction in the number of blades could cause an increased load on every single blade. Depending on the load distribution, the suction surface can be exposed to high negative pressure gradient followed by a strong adverse pressure gradient. This fact in conjunction with transitional nature of the flow could produce a very complicated flow condition.

Understanding the behavior of flow field around a turbine blade is of prime importance in gas turbine engineering as it can affect the design and performance of engine elements. An important phenomenon that can affect the flow regime is the effect of impinging wakes, originating from upstream stator blades, on the downstream rotor row. In the first part of this research, there has been an attempt to numerically model and investigate the behavior of the boundary layer development along the suction surface of a highly-loaded turbine blade under steady and unsteady inlet flow conditions using Reynolds Averaged Navier-Stokes (RANS) tools. RANS equations in conjunction with

turbulence models enable us to model flow fields. For unsteady case, the case was studied and modeled at a reduced frequency of the incoming wakes. Also, it includes a comprehensive assessment of predictive capabilities of commercial RANS numerical tools. To evaluate the reliability of current RANS-based numerical methods, rigorous boundary layer and heat transfer measurements that were previously done in unsteady boundary layer research facility of Turbomachinery Performance and Flow Research Lab (TPFL) of Texas A&M University, were used as a benchmark. The numerical simulation model is generated using the geometry of the same cascade facility at TPFL. Comparisons of the numerical results and the previously obtained experimental measurements detail the differences in predictive capabilities of the RANS methods regarding locating the onset and length of separation, velocity profile inside boundary layer, velocity fluctuations, surface pressure distribution and boundary layer parameters.

1.1 Turbine Aerodynamic Research

Gas turbine engines have been around for a long time, and the efficiency of them have been pushed to around 40%. The increasing demand for power and environmental issues, as well as limited resources of fossil fuels, has forced the researchers to constantly improve and modify their design approaching ideal Brayton cycle. To do that, thorough understanding of aerodynamics and heat transfer is required as they are closely related to one another.

An extensive unsteady boundary layer research was started in the mid 1960s at the Technical University Darmstadt, Germany, which gave birth to very fundamental and high impact publications. Pfeil and Herbst [8] and Pfeil, et al. [9] conducted experiments on the effects of unsteady wakes on boundary layer transition. In these publications, they

quantified the effect of unsteady wake-flow on boundary layer transition along a flat plate. They confirmed that when the wake region impinges on the plate surface, it causes the boundary layer to become turbulent momentarily. They introduced a model for transition process using time-space distribution of the turbulent spots. Orth [10] also investigated the boundary layer development along a flat plate under unsteady flow periodically disturbed by wakes produced by moving bars. The results show how the wake disturbances enter the boundary layer and result in turbulent patches, which are transported downstream. He also observed and reported the calming effect of the wakes.

Schobeiri and Radke [11] utilized a curved plate to carry out experimental investigations under zero and negative pressure gradient in an unsteady research facility using a rotating cascade of rods. They also showed that the incoming wakes generate turbulent patches that eventually penetrate the boundary layer resulting in a strong deformation and generation of high turbulence intensity. After they have completely penetrated the boundary layer, they leave behind a pronounced calmed region. Schobeiri and Pappu [12] examined unsteadiness on boundary layer development on a high-pressure turbine blade using a linear cascade facility. They used moving rods mounted on two parallel timing belts to produce periodic incoming wakes and studied the passing frequency, wake structures and freestream turbulence intensities on boundary layer development and transition. Chakka and Schobeiri [1] performed intermittency analysis and introduced an intermittency function for unsteady wake flow condition by experimentally investigating the wake effects as well as pressure gradient on boundary layer development and transition on a curved plate. They later expanded their investigations to the high-pressure turbine blades of NASA Space Shuttle Main Engine

and generalized their intermittency function [2]. The model introduces various intermittency values for regions inside and outside of the wake vortical core as a function of Reynolds number at the start and end of the transition. This model was later incorporated into a boundary layer code TEXSTAN. The results showed good agreement with measured heat transfer coefficient.

Stadtmüller and Fottner [13] surveyed the boundary layer with surface mounted hot-film sensors and hot-wire probe in a linear high-speed cascade facility under unsteady wake flow conditions. They measured the total pressure losses with a wake rake instrumented with pitot probe and fast-response pressure sensors to acquire time-averaged and time-resolved data.

Popovic, et al. [14] studied midspan aerodynamics performance of a family of three low-pressure turbine airfoils under steady condition inside a low-speed cascade wind tunnel. They showed that front-loaded airfoils could reduce the size of separation region significantly and in some cases eliminate the separation bubble. They proved that these kinds of airfoils are very resistant to flow separation. On the other hand, they showed that the aft-loaded airfoil had separation region on the suction side at almost all Reynolds numbers and turbulence intensities. Consequently, higher profile loss was recorded for aft-loaded airfoils compared to front-loaded ones. Also, they observed that at low Reynolds numbers, the separation bubble bursts abruptly and the suction surface flow changes from having a relatively short re-attaching bubble to be fully separated.

Schobeiri and co-workers [15, 16] extended their studies to low-pressure turbine blades. They examined the effects of periodic wake-induced inlet flow condition on the boundary layer development, separation and finally re-attachment on the suction surface

of a highly loaded low-pressure turbine blade. They also showed that the separation bubble under unsteady flow condition exhibits temporal behavior. These studies were performed to identify the transition process along a low-pressure turbine blade. Sjolander and co-workers [17, 18] also performed experimental measurements using hot-film method in a linear cascade of high-lift low-pressure turbine blades under unsteady flow conditions for various Reynolds number, free stream turbulence intensity (FSTI), wake frequency and flow coefficients. They deduced that presence of wakes could suppress the separation bubble considerably to the point that they can force the flow to re-attach even in low Reynolds number where normally no re-attachment follows the separation in wakeless condition. More recently Liang, et al. [19] used hot-film sensors to study the effect of wake passing frequency on boundary layer transition of a low-pressure turbine blade. For that matter, they used a linear cascade test rig and moving bar mechanism to simulate the flow inside a gas turbine engine. They showed that the wake passing frequency significantly changes the duration and size of the calmed region. They also observed that the wake frequency has opposite effects on laminar and turbulent friction losses, which indicates for a given airfoil, an optimum wake passing frequency exists that minimizes the total loss.

Wisler and Co-workers [20-23] performed a comprehensive boundary layer measurement and simulation on the airfoil surfaces in multi-stage, axial flow compressors and low-pressure turbines in a four-part paper. Boundary layer measurements were done using hot-film gauges and hot-wire probes while computations were made using steady and unsteady boundary layer codes. They divided the flow into two distinct but coupled paths. The first path lies under wake trajectory and the second path lies in between wakes.

They studied the location and strength of various regions within the paths and observed that transition is mostly governed by bypass and separated flow transitions.

Hourmouziadis and co-workers [24, 25] created a pressure distribution on a flat plate, matching the suction side of a turbine blade, using a contoured wall opposite to the flat plate to study separated transitional flow in unsteady flow conditions. They produced unsteadiness by incorporating a rotating flap located downstream of the test sections. Their results indicated that higher Reynolds number expedites transition and reduces transition length while separation onset remains unaffected. Gostelow and Thomas [26] investigated the laminar separation on a flat plate under a strongly self-diffusing laminar pressure distribution. Dähnert, et al. [27] also investigated the transition process along a flat plate in the presence of a pressure gradient and separation bubble and concluded that shear layer instability dominates transition.

Liu and Rodi [28] carried out unsteady boundary layer measurement on turbine cascade, which was installed downstream of a squirrel cage. Kaszeta, et al. [29] experimentally studied laminar-turbulent transition inside a channel in which side-walls resemble suction and pressure surfaces of a low-pressure turbine blade.

Schobeiri, et al. [30, 31] studied boundary layer development, transition, separation and finally re-attachment along suction surface of a highly-loaded low-pressure turbine blade using a costume designed hot wire probe.

CFD analysis plays a major role in modern turbomachinery design. Turbine blade design now relies heavily on steady and unsteady CFD analysis. The most widely used Computational method for simulations involving turbomachinery elements is the RANS method using statistical turbulence models. Even-though Large Eddy Simulation (LES)

and Direct Numerical Solution (DNS) methods promise more accurate results [32, 33], due to impractical large simulation time, RANS approach remains as the most popular computational tool for modeling turbulent flow. In RANS solvers all of the quantities are expressed in-terms of mean and fluctuating parts. Conventional turbulence models assume fully turbulent flow with no transitional effect. Hence they normally fail to predict the separation bubble [34]. Conventional turbulence models have been enhanced and modified over time to be able to capture transitional flow regime and its effects.

Numerous researchers have done simulation of wakes around low-pressure turbine blades. Meyer [35] is among the pioneers in this field that used a thin airfoil theory and potential flow. In this model, he replaced each wake by a perturbation (negative-jet) of uniform flow. The wakes were then transported by the mainstream. The negative jet causes a pressure build-up on the suction surface and a flow removal from the pressure side. Lefcort [36] extended the thin airfoil theory to wakes of finite thickness.

As computational tools have reached a level of maturity over the past few decades, the context of turbo-machinery aerodynamics has witnessed significant progress. Cho and Chung [37] proposed a transitional model suitable for implementation in RANS based solvers. They developed a set of transport equations for turbulence kinetic energy, k, turbulence dissipation, ε, and intermittency factor, γ. This model was originally produced for free shear flows and provides an acceptable cross-stream variation of intermittency factor. Steelant and Dick [38] proposed a method to simulate bypass transition using classical k-ε model. They took intermittency into account by conditioned averages during the fraction of time the flow is turbulent or laminar. This model was designed to reproduce the intermittency factor distribution of Dhawan and Narasimha [39] in the

streamwise direction. Suzen and Huang [40] blended the two models above to get the best features of the two. The outcome was a model that was capable of both reproducing intermittency distributions in streamwise and cross-stream directions. They later modified their intermittency transport model to computationally investigate the effect of unsteady wake/blade interactions [41]. For that matter, they combined their intermittency functions with Menter's SST model [42-44].

In another publication, Steelant and Dick [45] advanced their model and simulated skin friction and heat transfer using conditionally averaged Navier-Stokes equations. They defined two separate terms for free-stream turbulence factor and boundary layer intermittency factor and proposed a transport equation for a turbulence-weighting factor. Menter and co-workers [43, 44, 46, 47] introduced a transitional model and proposed two additional transport equations for intermittency factor (γ) and $Re\theta$(momentum thickness Reynolds number). This model, which is now the most popular model in transitional flow modeling and is implemented in many commercial solvers, uses local variables to identify the transition onset location. Following this approach, Lodefier, et al. [48] combined the fully turbulent k-ω model with a dynamic transport equation for intermittency and used local variables to trigger the transition onset in their model. In a more recent article, Durbin [49] used the same transport equation of Ref [48] and added penetration of free-stream turbulence into the boundary layer while he removed the separate transition correlation to switch γ on. This model was later modified and re-published in Ref [50] to predict transition in separated boundary layers. Schobeiri and co-workers [51] derived a transport equation based on flow measurements of a highly-loaded

turbine blade. They implemented this model in a RANS-based solver and numerically simulated transitional behavior under periodic condition.

Rodi and co-workers [52, 53] used DNS technique to model the flow inside a turbine cascade with incoming wakes originated from moving rods. Praisner and Clark [54] included an empirically based transition model for both attached and separated models into a RANS solver. They showed that trying to capture the freestream turbulences might enhance the accuracy of empiricism. Sarkar [55] studied the effects of wake structures on the evolution of the boundary layer over the suction surface of a highly-loaded LPT blade. They used LES method and instead of using the sliding mesh method for generating the wake. They interpolated the results of a flow past a cylinder into a domain that contains the airfoil.

Jagannathan, et al. [56] used high-pass filter Smagorinsky model for sub-grid scales to model the linear low-pressure turbine blade cascade flow with LES. They were able to capture the hairpin vortices near the transitional and turbulent flow regime on the suction side of the blade. Refs [57-59] are also examples of more recent studies in this field that both used RANS solvers and sliding mesh method to perform simulations.

1.2 Turbine Heat Transfer Research

Heat transfer aspect of the gas turbine blades in high-pressure stages was thoroughly discussed in many publications mainly because they are more exposed to higher temperature flow conditions than low-pressure or even intermediate-pressure stages.

Han, et al. [60] measured the effects of unsteady inlet flow condition on heat transfer of a high-pressure turbine blade. They located a spoke wheel ahead of a linear

cascade and produced unsteady wakes. Using hot-wire anemometry and a thin foil thermocouple instrumented blade; they studied the influence of unsteady wakes on heat transfer coefficient from the gas turbine blade. They observed that the unsteady wakes promote earlier transition, which in return cause much higher heat transfer coefficient on both suction surface and pressure surface of the blade.

Dullenkopf and Mayle [61] focused on effects of turbulence and moving wakes on laminar heat transfer of a high-pressure turbine blade. They correlated the effect of freestream turbulence on the Nusselt number and turbulence parameter. They then used this correlation in a quasi-steady model to predict the effect of incoming wakes on laminar heat transfer and compared the results against experimentally obtained data. Magari and LaGraff [62] studied wake-induced unsteady heat transfer of the stagnation region of a cylinder in cross-flow condition, which is a representative of the leading edge region of a gas turbine blade. They documented the heat transfer augmentation in the stagnation region due to wake unsteadiness at two different Mach numbers, one incompressible and one transonic. They also concluded that time-averaged heat transfer rate at the stagnation line experiences a maximum value independent of Reynolds number.

Giel and his co-workers [63, 64] studied heat transfer in a separated flow over a high-pressure airfoil inside a linear cascade. They performed measurements in a linear cascade with highly three-dimensional blade passage flows. They obtained data by a steady state technique using a thin-foil heater, low thermal conductivity blade and liquid crystal sheet attached to the surface of the blade. They studied heat transfer from the blade in a wide range of Reynolds number, pressure ratio, and incidence angle. They identified that variation in Reynolds number is responsible for laminar to turbulent

transition on the suction side of the blade and observed that isentropic exit pressure ratio has a negligible effect on heat transfer however it can indirectly affect heat transfer coefficient through Reynolds number. Finally, inlet flow angle was reported to also indirectly change the heat transfer coefficient value by relocating the stagnation point as well as changing the Reynolds number.

Schobeiri and Chakka [2] used a specially manufactured high-pressure blade with an internal heater core to measure heat transfer coefficient using a liquid crystal sheet glued to the center portion of the blade. They also implemented the universal intermittency function into a Navier-Stokes boundary layer code, TEXSTAN, which simultaneously solves the continuity, momentum and energy equations. The good agreement between predicted heat transfer results and experimentally obtained data proves that a physics-based transition model can enhance the level of reliability of numerical solvers.

Tallman, et al. [65] measured hot-gas side heat transfer to a 1½ stage high-pressure transonic turbine in a turbine test facility. They used thin platinum pyrex gauges for transient temperature measurements. The obtained readings were then analyzed using one-dimensional conduction assumption to find the heat flux to the surface.

Carullo, et al. [66] studied a transonic turbine blade in a cascade and investigated the effects of turbulence intensity, turbulence length scale and Reynolds number on heat transfer coefficient in a steady flow condition using thin film gauges that allow high spatial resolution with minimal flow disruption. In this method since the gauge changes resistance with temperature, it was used as one arm Wheatstone bridge circuit. They reported a heat transfer augmentation of 23% and 35% for pressure and suction sides

respectively at the nominal condition in high-turbulence intensity case compared to low-turbulence intensity flow condition.

Unlike high-pressure turbine stages, not enough attention has been paid to research the heat transfer from low-pressure blades, eventhough aerodynamics of such airfoils has been extensively discussed. Heat transfer in low-pressure stages could be even more complicated than intermediate and high-pressure stages due to flow complexities such as steep pressure gradient, flow transition and flow separation. Schobeiri, et al. [67] investigated the periodic unsteady wake on heat transfer from a low-pressure turbine blade in presence and absence of flow separation. They concluded that unsteady wakes, freestream turbulence intensity and Reynolds number all have direct effects on augmentation of heat transfer rate. According to their findings, heat transfer coefficient undergoes a continuous drop on suction side in the transitional region and separated flow zone followed by a local maximum at the location of flow re-attachment. On the pressure side, however, the effect of transition was more clearly seen as HTC drops and rises again in the transitional zone. They reported high FSTI could completely wash out the transition portion on the blade. This effect was observed on the pressure side of the blade. Also, it can completely submerge unsteady wakes and hence reduce the sensitivity of heat transfer coefficient to wake frequency in high FSTI.

Wolff, et al. [68] provided detailed velocity, heat transfer and pressure measurements of a separated flow over a low-pressure turbine blade. They used constant temperature anemometry (CTA) Wheatstone bridge with hot-film to find heat transfer coefficient. Unlike previous studies, they reported a local maximum in heat transfer coefficient distribution in the middle of flow separation region and a local minimum at

the location of reattachment. Furthermore, they reported a small peak just downstream of reattachment location due to high turbulent shear layers.

Among more recent publications, Refs [69, 70] discuss effects of unsteady wakes on end-wall surfaces of a linear cascade of turbine blades using naphthalene sublimation method to find heat/mass transfer distribution. They witnessed an increase in heat transfer in higher Strouhal number that was attributed to thinner boundary layer in unsteady case.

Computational tools have been extensively validated for HPT in terms of their accuracy and reliability of predicting heat transfer characteristics. In HPT stages, flow is normally attached and fully turbulent as opposed to low-pressure stages where the flow is generally transitional and often is accompanied by separation.

Abe, et al. [71, 72] introduced a new turbulence model and calculated heat transfer in separating and re-attaching flow. In this study, they introduced Kolmogorov velocity scale and used it in two-equation heat-transfer model to account for near-wall effects. Heyerichs and Pollard [73] calculated heat transfer rate in separated and impinging turbulent flow. Dunn [74] conducted a thorough literature survey about the heat transfer measurement techniques and predictions. He reported that RANS CFD has achieved limited success regarding calculating the heat transfer coefficient on a turbine blade. He attributed this deficiency to the lack of appropriate models to simulate turbulence structure.

Medic and Durbin [75] used two layer k-ε model as well as k-ω and $v^2 - f$ model to predict the turbulent behavior of the flow and deduced that using k-ε model with reasonable k production will result in rather good flow and heat transfer predictions. Hermanson, et al. [76] also used k-ε realizable model as well as k-ε realizable two-layer

model and $v^2 - f$ model to predict the external heat transfer for turbine vanes and blades in presence of secondary flow. It was found that *k-ε* model fails to correctly predict the heat transfer from the blade while $v^2 - f$ gives better agreement with experiments in terms of predicting the Stanton number value on the surfaces of the blade. De la Calzada and Alonso [77] used an in-house CFD code for heat transfer in separated flow to simulate the heat transfer particularly in separation and re-attachment zones. Also, the influence of inlet Mach number on heat flux has been studied. It was found that heat transfer coefficient drops in separation zone and goes through a local maximum downstream of the re-attachment region. It was also reported that Reynolds number is a dominant parameter and in a less significant manner, inlet flow angle influences heat transfer. Tallman [78] used a compressible RANS CFD solver with *k-ω* turbulence modeling to study the heat transfer to a high-pressure vane and a high-pressure blade of a 1½ stage turbine. He compared their results with a previously obtained data from a transient shock tunnel facility. He concluded that the compressible RANS solver is capable of predicting pressure and heat transfer at mid-span locations. Dunn and co-workers [79] performed an integrated experimental and numerical study. They measured heat transfer to the blade using heat flux gauges at the transonic condition and compared the results with industrial codes as well as a two dimensional code, UNSFLO-2D, developed previously by Giles [80, 81]. This code models the entropy generated around the airfoil using full Navier-Stokes equation, but propagates entropy inviscidly downstream to the next blade row. The comparison resulted in a very good agreement at mid-span between the experimental and the two numerical data sets.

De La Calzada, et al. [82] also reported that heat transfer coefficient goes through a local minimum and maximum respectively in the separation and re-attachment regions. Very recently Wang, et al. [83] investigated heat transfer from an outlet guide vane and endwall regions for a subsonic flow both from numerical and experimental points of view. They performed experiments in a linear cascade facility and used liquid crystal method. For numerical platform, they used a RANS solver with three different turbulence models. The models performed well to simulate pitch-wise averaged Nusselt number while significant deviations were observed in off-design conditions where separation becomes inevitable.

2 FLOW TRANSITION

Flow inside a gas turbine engine is highly complex and a detailed investigation is needed to study the effect of every single parameter on the performance of the entire engine. Some main factors that increase the level of complexity of flow in the engine are three-dimensional secondary flow, inherent unsteadiness, and freestream turbulence as well as large separation regions, especially in off-design condition and transitional flow regime.

Distribution of laminar, transitional and turbulent boundary layer flow regime defines the state of the boundary layer, which indicates loss production and heat transfer characteristics. The transition is a stochastical, unsteady and three-dimensional process in the region where the flow is intermittently laminar and turbulent. Also in order to be able to understand the behavior of film coverage on a surface as well as heat transfer, the underlying physics regarding aerodynamics of the problem has to be fully learned and understood. The following section that includes some of the high-impact articles in these fields explains the boundary layer transition process and discusses transition process categorizations. Also, it is tried to shed some light on the history and evolution of transitional flow studies performed over the past few decades.

2.1 Boundary Layer Transition

Boundary layer transition is a process in which boundary layer gradually develops and transitions from laminar to turbulent state. The turbulent boundary layer is identified by random occurrence and dissipation of swirls or “eddies”. Flow in turbomachines, especially in gas turbine engines, is highly transitional. Depending on parameters such as turbulence level, geometrical details, pressure gradient, and surface roughness, transition

mechanisms are categorized. Transition process of boundary layer under a steady flow field could generally be categorized into three different categories:

- Natural Transition
- Separated Flow Transition
- Bypass Transition

2.1.1 Natural Transition

Natural transition is the most common transition mechanism, which occurs due to the growth of unstable Tollmien-Schlichting waves. Laminar boundary layer develops linear oscillations of well-defined frequency when Reynolds number exceeds some certain value. Early studies in this regard were done by Reynolds [84], Burgers [85] and Van der Hegge Zijnen [86].

To mathematically explain the natural transition, several researchers, such as Prandtl [87] and Schlichting [88], used perturbation method and stability analysis. Through this analysis, the well-known Orr-Sommerfeld stability equation was derived [89, 90].

2.1.2 Separated Flow Transition

Separated flow transition occurs in the shear flow when the flow separates. A reattachment in the turbulent zone normally follows the separation. Hatman and Wang [91] categorized the separated flow transitions into three distinct categories:

(a) Transitional separation with transition starting upstream of the separated region. In this case, the transition is mostly developed as a natural transition.

(b) Short bubble mode with laminar separation. In this scenario, separation occurs while the flow is still laminar. The transition occurs downstream of the separation point by inflectional instability and a quick transition completion.

(c) Long bubble mode where separation still occurs in laminar flow regime but the transition completion is delayed.

Mayle [92] also performed a thorough literature review on the topic of separated flow transition.

2.1.3 Bypass Transition

Bypass transition is a very complex phenomenon and normally is imposed on the boundary layer by the high level of turbulence in the boundary layer. Morkovin [93] showed that Orr-Sommerfeld equation was not applicable for relatively high turbulence intensities. In this situation, the Tollmine–Schlichting waves are bypassed, and turbulence spot formations are occurring right away. This kind of transition usually happens for airfoils encountering wakes originating from the upstream device.

Aside from bypass transition, turbomachinery elements are also prone to reverse transition [92], where flow transitions from turbulent to laminar state at low turbulence levels.

2.1.4 Transition in Turbomachinery

Flow in turbomachinery is highly unsteady and periodic. Due to periodic nature of the flow, the transition process is also seen as a transient or unsteady process. The transition is an extraordinarily complicated process and is not yet fully understood. Transitional parameters are greatly affected by flow conditions thus understanding and describing the physics of transitional flow in turbo-machines are of prime importance.

Correct modeling of transition is crucial in turbomachinery elements design as it can help better prediction of profile loss.

Numerous attempts have been made by many researchers to mathematically model transition. Emmons [94] used turbulent spot production theory to investigate the transition process. According to this theory, every point of the body is turbulent a fraction of the time. This theory was also incorporated by Dhawan and Narasimha [39]. They tried to describe and model the intermittency distribution of the flow and justify statistical similarities of transitional flows. They defined intermittency factor for a natural transition. Dey and Narasimha [95] promoted the same theory and treated the global flow as a combination of turbulent and laminar flow which resulted in good prediction in zero and favorable pressure gradient but failed in predicting accurate results for negative pressure gradient flows. To more accurately identify the turbulent from non-turbulent flow, especially in unsteady flows, Townsend [96] used an analog method that counted the periods of time that a turbulent fluctuation quantity could be judged non-zero and based on that, he proposed a method to calculate the intermittency function. Hedley and Keffer [97] proposed derivative of velocity signals as detector function that uses information from longitudinal and lateral fluctuations. This approach was widely used by numerous researchers, among others, in Ref [98].

Numerous studies have concentrated on identifying and correlating the onset and extent of boundary layer transition. Abu-Ghannam and Shaw [99] proposed a model for locating the transition onset and end under different pressure gradients and flow conditions. Walker and Gostelow [100] proposed a transition model in an adverse pressure gradient. They surveyed the popular existing transition model at that time to

identify the deficiencies and developed their model based on the fact that Tollmien-Schlichting waves appear more often in adverse pressure gradient flows than zero pressure gradient flow conditions.

Gostelow, et al. [101] focused on the effects of turbulence, pressure gradient, and flow history. They revealed that there could be an exponential decrease in transition length with increasing adverse pressure gradient. They also included that turbulence level has a similar but less significant effect compared to the pressure gradient.

2.2 Physics of Intermittent Flow, Transition

In order to better understand the physics of intermittent flow, a flat plate with a smooth surface inside a wind tunnel is considered. If a miniature hotwire sensor is placed downstream of the laminar region, within the boundary layer, it can provide an instantaneous response to any high-frequency incoming flow [102]. The following picture shows how by accurately positioning the hot-wire sensor inside the boundary layer, the high-frequency response could be registered.

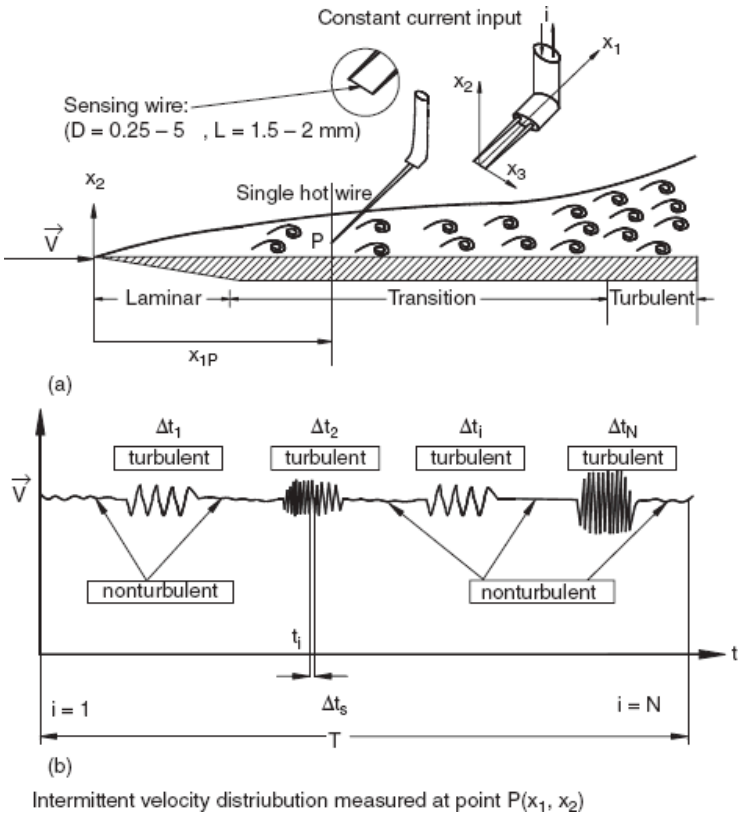

Figure 2-1 Measurement of turbulence intermittency by correctly positioning the hot-wire sensor inside the boundary layer and registering the high-frequency response [102]

In a transitional flow regime, sequences of turbulent and non-turbulent signals would appear intermittently. In order to identify turbulent from non-turbulent signals, the following approach, originally suggested by Kovasznay [103], is normally adopted. They define the intermittency function in the following manner:

$$I(x,t)=\begin{cases} 1 & \textit{turbulent} \\ 0 & \textit{laminar} \end{cases} \tag{2-1}$$

Figure 2-2 shows the intermittently laminar-turbulent flow and the corresponding intermittency function value.

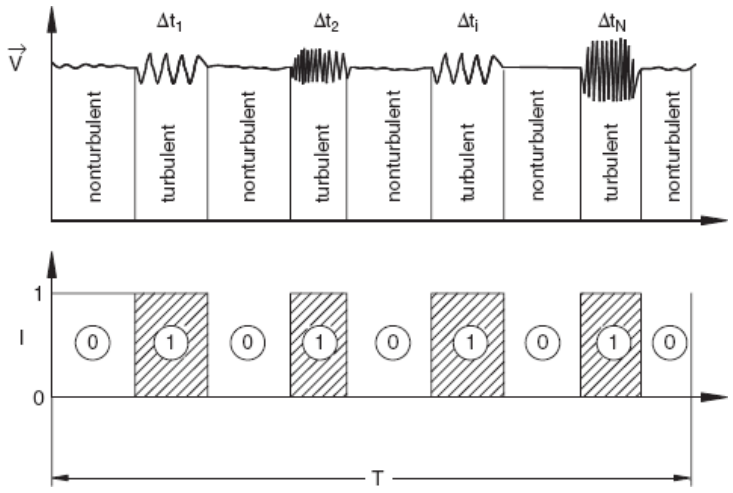

Figure 2-2 Identification of turbulent, non-turbulent flow [102]

Once the turbulent, non-turbulent region is identified and the distribution of intermittency function *I(x,t)* is obtained, the intermittency factor γ could be defined using the following equation:

$$\gamma(x) = \frac{\sum_{i=1}^{N} \Delta t_i}{T} = \frac{1}{T}\int_{t}^{t+T} I(x,t)\,dt \qquad \textbf{(2-2)}$$

Intermittency factor, γ, simply is the fraction of the time that flow is turbulent in a sufficiently long period of time.

Velocity fluctuations are not sufficient to make instantaneous decisions and determine whether a certain flow is laminar or turbulent. For that reason, velocity signals have to be sensitized to more easily judge on this matter. Finding time derivative of velocity signals is a common practice for this purpose. Figure 2-3 shows the instantaneous velocity at a particular location along with the sensitized signal (time-derivative) and the indicator function, *I(t)*.

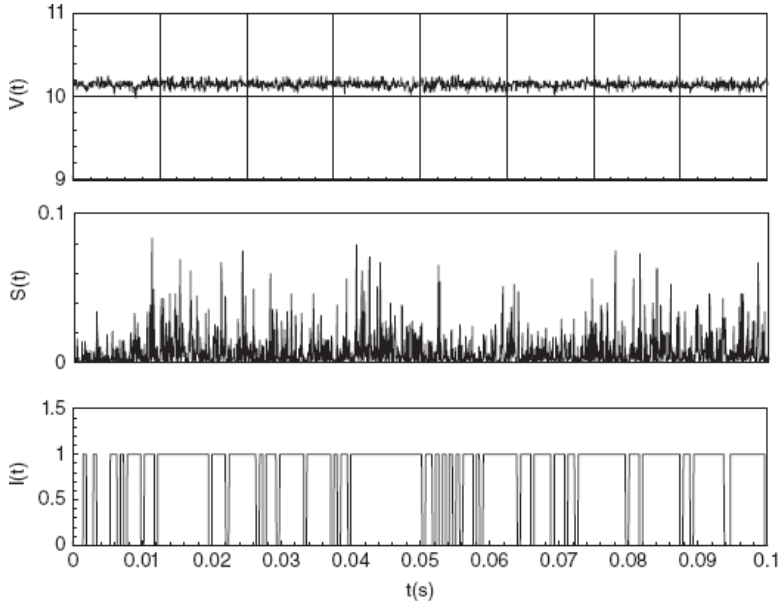

Figure 2-3 Instantaneous velocity (top), sensitized velocity signal (middle) and the indicator function (bottom) [104]

I(t) is defined in the following way:

$$I(x,t) = \begin{cases} 1 & when \quad S(x,t) \geq C \\ 0 & when \quad S(x,t) < C \end{cases} \tag{2-3}$$

The resulting square wave is used to condition the appropriate averages using the equations above. Performing the averaging process (Equation (2-2)) for the steady flow shown in Figure 2-3, one could find the intermittency factor, γ. The intermittency factor γ is always between 0 and 1. Intermittency factors of 0 and 1 correspond to laminar and turbulent flow regimes respectively. Intermittency flow measurements could be done at different stream-wise and cross-stream locations.

Intermittency factor could change in both stream-wise and normal directions. Figure 2-4 shows the intermittency factor distribution in stream-wise direction along the concave surface of a curved plate at zero-pressure gradient for different normal distances.

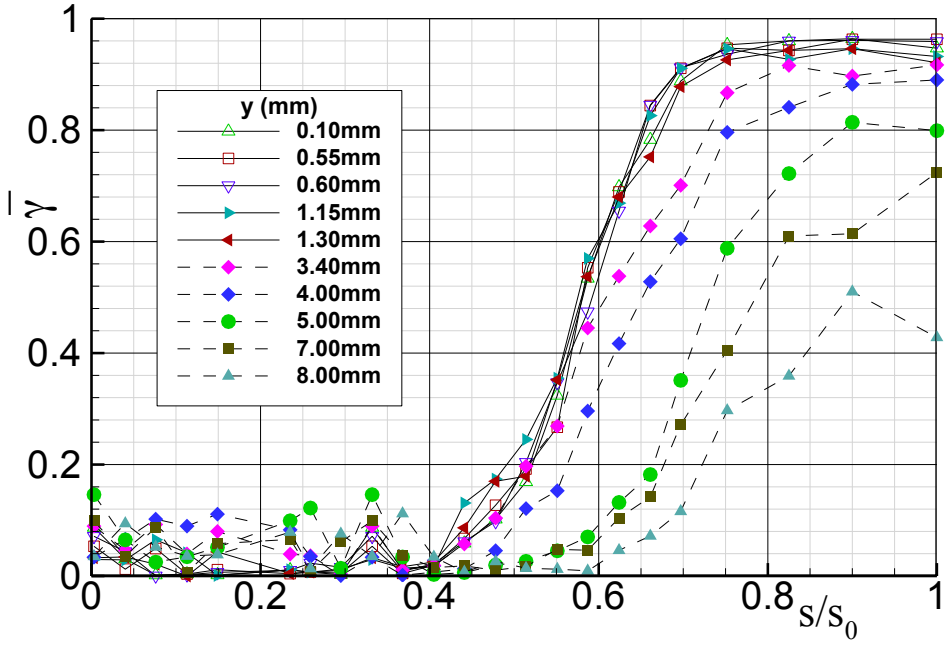

Figure 2-4 Intermittency distribution in stream-wise direction for the curved plate, measured at different normal distances from the plate surface [1]

Close to the surface, the intermittency starts from zero and approaches its maximum value as the flow progresses in the stream-wise direction. Moving away form the surface would result in lower values for intermittency factors which translates into non-turbulent free-stream.

2.3 Evolution of The Universal Intermittency Function

Flow in many engineering devices, especially gas turbine engines, is of periodic nature due to interactions between the stationary and rotating components. Figure 2-5 shows the unsteady flow interaction within a turbine stage.

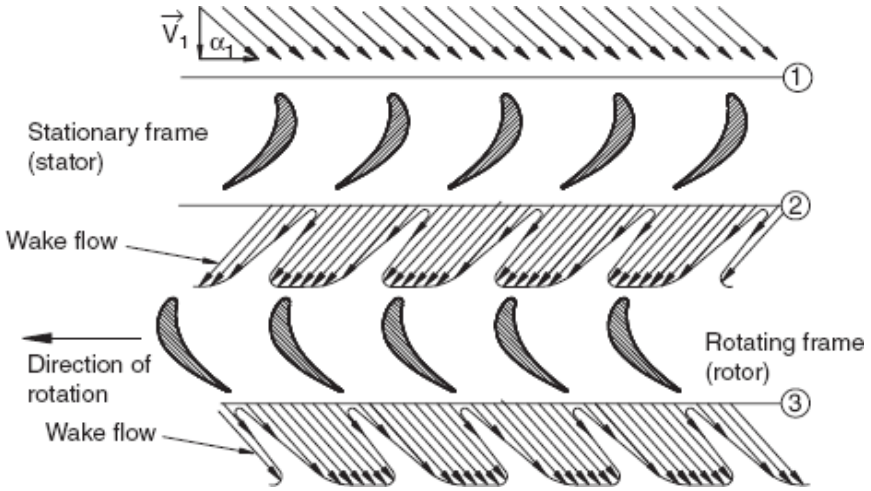

Figure 2-5 Unsteady flow interaction between stationary and rotating frames in gas turbine engines [102]

The flow is spatially periodic downstream of stator blade row and temporally periodic downstream of the rotor row. This periodic unsteady flow condition cannot be studied and modeled in the same manner that a transitional flow is described in the previous section. Once the instantaneous velocity, in this periodic unsteady case, is ensemble averaged, the intermittency factor can be calculated using:

$$< \gamma(x,t) >= \frac{1}{M}\sum_{j=1}^{M} I(t_i, j) \qquad \textbf{(2-4)}$$

In equation (2-4), *M* refers to the total number of ensembles. Figure 2-6 shows different ensembles of a periodic unsteady flow. Also, the corresponding intermittency function *I(t,j)* at a given position vector is shown. *I(t,j)* could be obtained for each ensemble in the same way that intermittency function was defined in a statically steady flow.

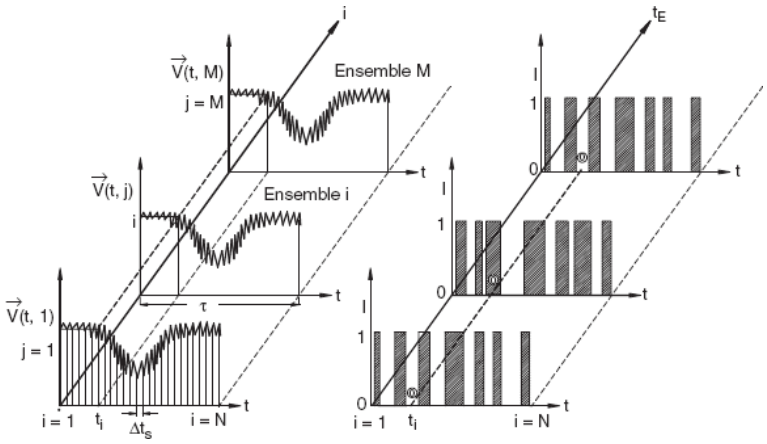

Figure 2-6 Periodic unsteady flow velocity *V(x,t)* and the distribution of *I(x,t)* at different ensembles [102]

In order to find the instantaneous intermittency in a periodic unsteady flow, instantaneous velocity has to be sensitized and then intermittency function *I(x,t)* must be obtained. Finally by ensemble-averaging the intermittency function *I(x,t)*, the time dependent intermittency factor could be obtained. The following picture shows the entire process of determining the γ(t).

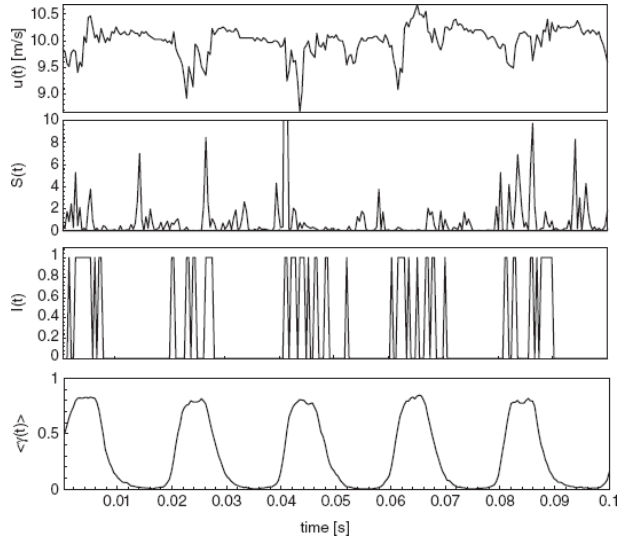

Figure 2-7 Processing of instantaneous velocity signals and finding of γ(t) [102]. These data were taken and post processed for S/S_0=0.5235 and the vertical location y=0.1 mm

This figure was obtained by recording the velocity at a specific location (S/S_0=0.5235 and y=0.1mm) on a curved plate. The periodicity, in this case, was produced by moving a set of cylindrical rods with a diameter of 2mm in front of the curved plate. For each ensemble, the velocity signals are sensitized and ensemble average of *I(x,t)* is taken to obtain ensemble-averaged $<\gamma(x,t)>$. By repeating the same procedure for all locations on the curved plate, Figure 2-8 could be obtained.

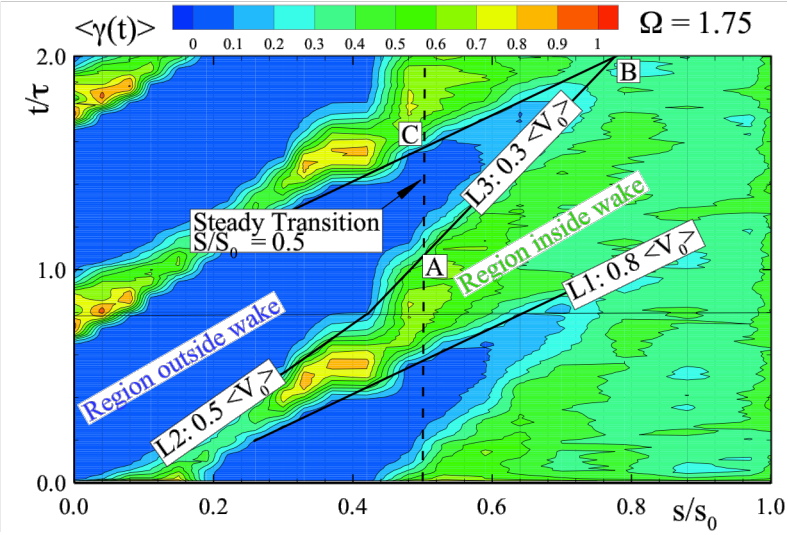

Figure 2-8 Contour plot of intermittency factor along the stream-wise direction for unsteady frequency of Ω=1.75 [102]

The zones with lower intermittency mark the regions outside of the wake and the zones with higher intermittency values, indicate the highly vortical core of impinging wakes. Prior to $S/S_0 \approx 0.6$, there is a clear distinction between regions inside and outside of the wake. Each wake strip is defined by two lines, *L1* and *L2*, which mark the leading and the trailing edges of the wake respectively. The state of boundary layer becomes momentarily turbulent once the wakes have impinged on the plate surface and immediately after the wakes have passed, the same location would be exposed to calm

region. The calming effect could potentially delay the natural transition as long as unsteady wakes have not mixed. Increasing turbulence intensity or reduced frequency can increase the chance of mixing the wakes and shifting the transition upstream. The calming effect has been studied extensively before by Schubauer and Klebanoff [105], Herbst [106], and Schobeiri and Radke [11].

2.3.1 Intermittency Modeling of Periodic Unsteady Flow

Chakka and Schobeiri [1] performed intermittency analysis and proposed an intermittency function for unsteady wake flow condition by experimentally investigating the wake effects as well as the pressure gradient on boundary layer development and transition along a curved plate. They later expanded their experiments to the high-pressure turbine (HPT) blades of the NASA Space Shuttle Main Engine (SSME) and generalized their unsteady boundary layer transition model [2].

This model specifically is designed for wake flow condition. A relative intermittency is introduced in this model that relates between maximum intermittency (vertical core inside the wake) and the minimum intermittency (becalmed region). It was shown in the studies above that the relative intermittency in the wake flow condition follows a Gaussian distribution when plotted with respect to non-dimensionalized lateral distance (Figure 2-9).

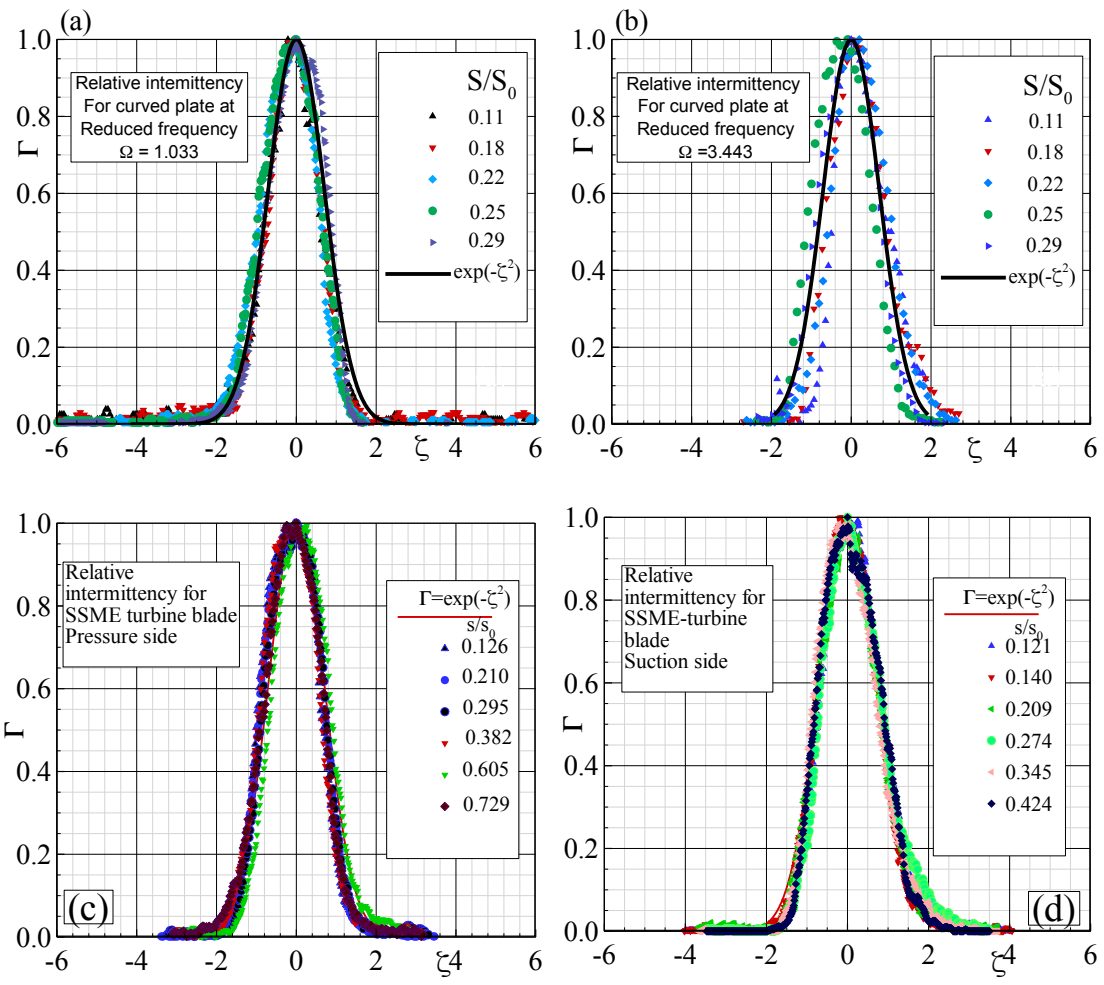

Figure 2-9 Relative intermittency as a function of non-dimensionalized lateral coordinate for curved plate (a) and (b), and high-pressure turbine blade (c) and (d) [2]

Schobeiri and co-workers [1, 2] defined a dimensionless wake parameter, ζ:

$$\zeta = \frac{tU_w}{b} = \frac{ts_R}{\tau b} = \frac{\xi_2}{b} \qquad \textbf{(2-5)}$$

In this equation, U_w is the belt (wake generator) translational velocity and b is the wake width, and it is calculated by the following equation:

$$b = \frac{1}{\sqrt{\pi}} \int_{-\infty}^{+\infty} \Gamma d\xi_2 \qquad \textbf{(2-6)}$$

According to [1, 2] the relative intermittency can be defined as :

$$\Gamma = \frac{\gamma(t) - \gamma_{\min}(t)}{\gamma_{\max}(t) - \gamma_{\min}(t)} \tag{2-7}$$

In this equation, $\gamma(t)$ is the ensemble-averaged intermittency function. $\gamma_{max}(t)$ and $\gamma_{min}(t)$ are respectively the time-dependent intermittency inside and outside the wake vortical core. The following equation could best describes the Gaussian distribution shown in Figure 2-9:

$$\Gamma = e^{-\xi^2} \tag{2-8}$$

Minimum, maximum and average intermittency values for a wake flow is formulated by Ref [2]:

$$\gamma_{\max} = 1 - c_1 e^{-\left[\frac{\mathrm{Re}-\mathrm{Re}_s}{\mathrm{Re}_e-\mathrm{Re}_s}\right]^2} \tag{2-9}$$

$$\gamma_{\min} = c_2 \left(1 - e^{-\left[\frac{\mathrm{Re}-\mathrm{Re}_s}{\mathrm{Re}_e-\mathrm{Re}_s}\right]^2}\right) \tag{2-10}$$

$$\gamma_{avg} = c_4 \left(1 - c_3 e^{-\left[\frac{\mathrm{Re}-\mathrm{Re}_s}{\mathrm{Re}_e-\mathrm{Re}_s}\right]^2}\right) \tag{2-11}$$

The constants seen in the above equations are functions of reduced frequency Ω and are listed in the following table. They are obtained for specific operating conditions.

Table 2-1 model constants

Constants	Ω=1.333	Ω=1.725	Ω=3.443	Ω=5.166
c_1	0.57	0.22	0.50	0.35
c_2	0.80	0.85	0.86	0.88
c_3	1.00	0.82	0.80	0.80
c_4	0.85	0.92	0.92	0.94

According to the universal intermittency function [1, 2], the flow intermittency would vary for locations inside and outside of the wake vortical core. As the wake impinges on a surface, turbulence intermittency rises almost instantly and drops immediately due to calming effect after the wake passes. This unique characteristic of unsteady periodic wake-induced flow is successfully captured by universal intermittency function formulation.

3 COMPUTATIONAL FLUID DYNAMICS AND TURBULENCE MODELING

This chapter is dedicated to computational fluid dynamics and especially finite volume method. Details of turbulence modeling are also included in this chapter. Computational fluid dynamics is a numerical tool in which governing differential equations (momentum, continuity and energy equations) are algebraically modeled, and different numerical tools are used to provide a solution for a system of equations representing governing equations. With advancements in computational power in the past few decades, more complex models have had the chance to be introduced and tested.

The continuity equation for incompressible flow has the following form:

$$\nabla.\vec{V} = 0 \tag{3-1}$$

The momentum equation has the following mathematical description:

$$\frac{D\vec{V}}{Dt} = -\frac{1}{\rho}\nabla p + \vec{g} + \nu\Delta\vec{V} \tag{3-2}$$

The energy equation:

$$\rho C_p \frac{DT}{Dt} = k\nabla^2 T + \mu\left(\frac{\partial V_i}{\partial x_j} + \frac{\partial V_j}{\partial x_i}\right)\frac{\partial V_i}{\partial x_j} \tag{3-3}$$

The continuity equation for an incompressible flow may be expanded to:

$$\frac{\partial V_1}{\partial x_1} + \frac{\partial V_2}{\partial x_2} + \frac{\partial V_3}{\partial x_3} = 0 \tag{3-4}$$

In the same manner, the momentum equations for incompressible flow can be re-written in the following form.

$$\rho\left(\frac{\partial V_1}{\partial t} + V_1\frac{\partial V_1}{\partial x_1} + V_2\frac{\partial V_1}{\partial x_2} + V_3\frac{\partial V_1}{\partial x_3}\right) = -\frac{\partial p}{\partial x_1} + \mu\left(\frac{\partial^2 V_1}{\partial x_1^2} + \frac{\partial^2 V_1}{\partial x_2^2} + \frac{\partial^2 V_1}{\partial x_3^2}\right) + \rho g \tag{3-5}$$

$$\rho\left(\frac{\partial V_2}{\partial t}+V_1\frac{\partial V_2}{\partial x_1}+V_2\frac{\partial V_2}{\partial x_1}+V_3\frac{\partial V_2}{\partial x_3}\right)=-\frac{\partial p}{\partial x_2}+\mu\left(\frac{\partial^2 V_2}{\partial x_1^2}+\frac{\partial^2 V_2}{\partial x_2^2}+\frac{\partial^2 V_2}{\partial x_3^2}\right)+\rho g_2 \quad \textbf{(3-6)}$$

$$\rho\left(\frac{\partial V_3}{\partial t}+V_1\frac{\partial V_3}{\partial x_1}+V_2\frac{\partial V_3}{\partial x_1}+V_3\frac{\partial V_3}{\partial x_3}\right)=-\frac{\partial p}{\partial x_3}+\mu\left(\frac{\partial^2 V_3}{\partial x_1^2}+\frac{\partial^2 V_3}{\partial x_2^2}+\frac{\partial^2 V_3}{\partial x_3^2}\right)+\rho g_2 \quad \textbf{(3-7)}$$

Total energy equation can also be written in this form

$$c_p\left(\frac{\partial T}{\partial t}+V_1\frac{\partial T}{\partial x_1}+V_2\frac{\partial T}{\partial x_2}+V_3\frac{\partial T}{\partial x_3}\right)=\frac{k}{\rho}\left(\frac{\partial T^2}{\partial x_1^2}+\frac{\partial T^2}{\partial x_2^2}+\frac{\partial T^2}{\partial x_3^2}\right)+\frac{1}{\rho}\left(\frac{\partial p}{\partial t}+V_1\frac{\partial p}{\partial x_1}+V_2\frac{\partial p}{\partial x_2}+V_3\frac{\partial p}{\partial x_3}\right)+\frac{1}{\rho}\phi \quad \textbf{(3-8)}$$

Five unknowns in the above equations are *P, V_1, V_2, V_3* and *T*. Governing equations shown above form a system of complex non-linear partial differential equations and thus they are very difficult to solve analytically. These equations are first linearized and then are solved. For unsteady problems, the system is marched in time, and a solution is obtained for each time-step.

3.1 Reynolds Averaged Navier-Stokes (RANS)

Reynolds number is a measure of turbulence inside a system. It was first introduced by Osborne Reynolds[107] and is the ratio of inertial forces to viscose forces. It is observed that while Reynolds number is below some certain value-critical Reynolds number-the flow is very smooth and no time dependency is recorded. This flow is called laminar flow. At or above the critical Reynolds number, random fluctuations in flow quantities such as pressure, velocity, and temperature with unsteady characteristics are seen inside the flow. These random fluctuations characterize turbulent flow. Flow quantities in turbulent flow can be decomposed into a mean steady value and a fluctuating

component. In a statistically steady flow, the velocity vector is decomposed in the following way:

$$V(x,t) = \bar{V}(x) + V'(x,t) \tag{3-9}$$

This same decomposition can be applied to describe the different components of velocity and pressure mathematically. The mean $\bar{Q}$ of a flow quantity, Q can be defined as:

$$\bar{Q} = \frac{1}{\delta t}\int_0^{\delta t} Q(t)\,dt \tag{3-10}$$

Q is a time-dependent quantity and could be a 0^{th} order tensor quantity such as temperature and pressure or a first order tensor quantity such as velocity. Q can be separated into mean and fluctuating components:

$$Q(t) = \bar{Q} + Q(t)' \tag{3-11}$$

By definition, in a statistically steady flow, the time-average of the fluctuating component is zero:

$$\bar{Q}' = \frac{1}{\delta t}\int_0^{\delta t} Q'(t)\,dt = 0 \tag{3-12}$$

From equation (3-12) it follows that:

$$\bar{\bar{Q}} = \bar{Q} \tag{3-13}$$

By substituting $V_i(t)$ with $\bar{V}_i(t) + V_i'(t)$ and $P_i(t)$ within momentum (Navier-Stokes equation) and averaging both sides, following equations are derived:

$$\frac{\partial \bar{V}_i}{\partial x_i} = 0 \tag{3-14}$$

$$\rho\frac{\partial\overline{V}_i}{\partial t}+\rho\overline{V}_j\frac{\partial\overline{V}_i}{\partial x_j}=\rho\overline{g}_i+\frac{\partial}{\partial x_j}\left[-\overline{p}\delta_{ij}+2\mu D_{ij}-\rho\overline{V_i'V_j'}\right] \quad \textbf{(3-15)}$$

Where D_{ij} is the mean rate of strain tensor and is defined as

$$\overline{D_{ij}}=\frac{1}{2}\left(\frac{\partial\overline{V}_i}{\partial x_j}+\frac{\partial\overline{V}_j}{\partial x_i}\right) \quad \textbf{(3-16)}$$

Equation (3-15) is commonly known as Reynolds Averaged Navier-Stokes equation. The last term on the right-hand side of the equation ($\rho\overline{V_i'V_j'}$) is the Reynolds stress term. This extra term requires some closure equations. Turbulence modeling is needed to predict Reynolds stresses and their transport terms.

3.2 Statement of RANS CFD (Turbulence Modeling), Past And Present

Turbulence models that are widely used to model turbulent behavior and close the Reynolds equations are categorized into two groups according to whether Boussinesq assumption is incorporated or not [108]. Models that fall into the first group are those that use this assumption and usually are referred to as turbulent viscosity models or first order models. According to experimental evidence, this assumption holds true for many engineering flow circumstances. The second group that is also known as Reynolds stress model or second order closures, avoids using this assumption. Such models are more general than the first order models and are expected to provide better results for cases in which flow is encountered by sudden changes in mean strain rate or high streamline curvature. They are based on solving transport equations for individual components of Reynolds stress tensor and dissipation rate. This fact adds to the level of complexity of the mathematical system, which eventually leads to reduced numerical robustness and higher computational effort. Even though, the Reynolds stress models are better suited to

predict complex flows; practice has proven that they do not necessarily provide better results than first order models.

There is also a third group that consists of models that are not based entirely on Reynolds equations. Large-eddy simulations fall into this category. Turbulence models could also be classified according to the number of partial differential equations that must be solved, from zero to 12, to obtain closure [108].

3.2.1 Zero-Equation Models

3.2.1.1 Prandtl Mixing Length Hypothesis

Prandtl mixing length hypothesis is the cornerstone of many of the early turbulence models. According to Prandtl hypothesis [109], eddy viscosity can be represented by:

$$\mu_t = \rho l_m^2 \left| \frac{\partial V_1}{\partial x_2} \right| \quad \textbf{(3-17)}$$

In this equation, l_m is the mixing length and is flow dependent. For two-dimensional boundary layer flow, inside the viscose sub-layer, the l_m could be found by this equation:

$$l_m = kDy \quad \textbf{(3-18)}$$

In this equation, k is an empirically obtained constant and D is the Van-Driest damping function. For the logarithmic region outside viscose sub-layer equation (3-18) reduces to:

$$l_m = ky \quad \textbf{(3-19)}$$

This equation can be used along with equations (3-14) and (3-15) to find the mainstream velocity components ($\overline{V}_i, \overline{V}_j$).

3.2.1.2 Algebraic Model: Cebeci Smith Model

Cebeci-Smith[110] model is an algebraic model which divides the boundary layer into two sub-layers. First one includes viscose sub-layer, buffer layer and a portion of outer region. The second layer includes remaining of the outer region. For the inside layer, the viscosity is calculated using this equation:

$$\nu_{t_i} = l_m^2 \left[\left(\frac{\partial V_1}{\partial x_2} \right)^2 + \left(\frac{\partial V_1}{\partial x_1} \right)^2 \right]^{1/2} \quad \textbf{(3-20)}$$

l_m is obtained from Van-Driest model:

$$l_m = \kappa y \left(1 - e^{-y^+/A^+} \right) \quad \textbf{(3-21)}$$

With κ=0.4 and $A^+ = 26\left(1 + y\frac{dp/dx}{\rho u_\tau^2}\right)^{-1/2}$. For the outer layer, the turbulent kinematic viscosity is obtained through this equation:

$$\nu_{t_o} = \alpha U_e \delta_1 F_{Kl}\left(y;\delta\right) \quad \textbf{(3-22)}$$

In this equation, α=0.0168, U_e is the velocity at the edge of the boundary layer, and δ_1 is the boundary layer displacement thickness. F_{Kl} is Klebanhoff intermittency function [111].

3.2.1.3 Algebraic Model: Baldwin-Lomax Model

Another algebraic model that is common is the Baldwin-Lomax model [111]. Similar to Cebeci-Smith model, this model also divides boundary layer into two separate sub-layers and uses algebraic correlation to find the kinematic viscosity in the boundary layer. For the inner layer the kinematic viscosity is calculated from this equation:

$$\nu_{t_i} = l_m^2 |\Omega| \tag{3-23}$$

Mixing length in this equation is obtained from equation (3-21) and Ω is the rotation tensor. For outer layer the viscosity is obtained by this equation:

$$\nu_{t_o} = \alpha C_{cp} F_{wake} F_{kl}\left(y, y_{\max} / C_{Kleb}\right) \tag{3-24}$$

F_{wake} is the wake function:

$$F_{wake} = \min\left(y_{\max} F_{\max}; C_{wk} y_{\max} U_{diff} / F_{\max}\right) \tag{3-25}$$

In this equation F_{max} is the maximum of the following function:

$$F(y) = y|\Omega|\left(1 - e^{-y^+/A_0}\right) \tag{3-26}$$

U_{diff} is defined by:

$$U_{diff} = \left(\sqrt{V_1^2 + V_2^2}\right)_{\max} - \left(\sqrt{V_1^2 + V_2^2}\right)_{\min} \tag{3-27}$$

3.2.2 One-Equation Models

In this category, one turbulent transport equation is solved. The one-equation turbulence model was originally proposed by Prandtl [112]. The transport equation has the following form:

$$\frac{\partial Z}{\partial t} + V_i \frac{\partial Z}{\partial X_i} = \frac{1}{\sigma} \frac{\partial}{\partial x_i}\left[\left(\nu + \nu_t \frac{\partial V}{\partial x_i}\right)\right] + P(Z) - D(Z) \tag{3-28}$$

The turbulence variable (Z) is normally turbulence kinetic energy. Left-hand side of the equation above, represents the material derivative of turbulence variable (summation of temporal and convective transport terms), while on the right-hand side there are diffusion, production and destruction terms of the parameter Z respectively. Prandtl [112],

Baldwin-Barth [113] and Spalart-Allmaras [114] brought closure to the transport equation by correlating the eddy viscosity and the turbulence parameter *Z*.

3.2.3 Two-Equation Models

Two equation models are the most popular models in the industry. By definition, two-equation models include two transport equations of turbulence parameters. Turbulence kinetic energy, *k*, is often one of the transported variables. The other transported quantity normally is either dissipation, ε, or specific dissipation, ω. These equations are used to find turbulent viscosity, μ_t.

3.2.3.1 *k*-ε Model

Launder and Spalding [115] proposed the following transport equation for turbulent kinetic energy and dissipation.

$$\frac{Dk}{Dt} = \frac{1}{\rho}\frac{\partial}{\partial x_j}\left(\frac{\mu_t}{\sigma_k}\frac{\partial k}{\partial x_j}\right) + \frac{\mu_t}{\rho}\left(\frac{\partial \bar{V}_i}{\partial x_j} + \frac{\partial \bar{V}_j}{\partial x_i}\right)\frac{\partial \bar{V}_i}{\partial x_j} - \varepsilon \tag{3-29}$$

$$\frac{D\varepsilon}{Dt} = \frac{1}{\rho}\frac{\partial}{\partial x_j}\left(\frac{\mu_t}{\sigma_\varepsilon}\frac{\partial \varepsilon}{\partial x_j}\right) + C_{\varepsilon 1}\frac{\mu_t}{\rho}\frac{\varepsilon}{k}\left(\frac{\partial \bar{V}_i}{\partial x_j} + \frac{\partial \bar{V}_j}{\partial x_i}\right)\frac{\partial \bar{V}_i}{\partial x_j} - \frac{C_{\varepsilon 2}\varepsilon^2}{k} \tag{3-30}$$

Turbulent viscosity is then obtained after finding the *k* and ε values through this closure equation:

$$\mu_t = \nu_t \rho = \frac{C_\mu \rho k^2}{\varepsilon} \tag{3-31}$$

The constants seen in the above equations are calibration constants and are obtained by simple flow configuration [109]. One of the disadvantages of the originally proposed *k*-ε model is that the terminology of equations (3-29) and (3-30) do not reflect molecular viscosity hence in the near wall region, where the effects of molecular viscosity become

apparent; they fail in predicting reasonable results. In order to solve this situation, near-wall treatment for *k*-ε model was introduced. Near-wall treatment methods generally are categorized into two approaches: Low-Reynolds Number (LRN) treatment and High-Reynolds Number (HRN) treatment. In the former approach, the centroid of the first cell is located close to the wall in such a way that $y^+ \sim 1$. This results in a very fine mesh and requires very high computational power. In the latter approach, wall functions are used either in the source term of the momentum equation or in the turbulent viscosity of the cells adjacent to the wall. In HRN method, the centroid of the first cell adjacent to the wall has to be within the log-layer of the boundary condition since this method relies on log-law velocity profile within the boundary layer.

3.2.3.2 *k*-ω Model

In the *k*-ω model, instead of solving the transport equation for dissipation, ε, a transport equation for specific dissipation, ω, is proposed and solved. Specific dissipation was defined by Wilcox[116] as:

$$\omega = \frac{\varepsilon}{C_v k} \tag{3-32}$$

And eddy viscosity could be obtained from this equation:

$$\mu_t = \rho \frac{k}{\omega} \tag{3-33}$$

According to Wilcox formulation, the transport equation for specific dissipation is:

$$\frac{\partial \omega}{\partial t} + U_j \frac{\partial \omega}{\partial x_j} = \alpha \frac{\omega}{k} \tau_{ij} \frac{\partial U_i}{\partial x_j} - \beta \omega^2 + \frac{\partial}{\partial x_j}\left[\left(\nu + \sigma \nu_T \right) \frac{\partial \omega}{\partial x_j} \right] \tag{3-34}$$

Closure coefficients for the above equation are listed in the following table:

Table 3-1 Closure coefficient in *k*-ω turbulence model

α	β	σ
5/9	3/40	1/2

Since there has to be no production of turbulence in near-wall region, due to molecular viscosity, the appropriate boundary condition for *k* would be:

$$k_{wall} = 0 \tag{3-35}$$

This boundary condition applies to the transport equation of *k* in the *k*-ε model as well. This boundary condition, however, gives rise to a problem; specific dissipation in near-wall region has to approach to infinity according to this equation. To solve that issue, Wilcox proposed that ω at the wall has to be set to:

$$\omega_{wall} = \frac{60\nu}{C_{\mu}\left(\Delta y^2\right)} \tag{3-36}$$

In this equation, *y* is the normal distance of the first node from the solid wall.

3.2.3.3 *k*-ω SST Model

The Shear Stress Transport (SST) model is a hybrid model that incorporates a blending function that activates *k*-ω model for near wall regions and switches to *k*-ε for regions far from the solid wall. This model was proposed by Menter [42] to obtain the best of the two models as *k*-ω is more robust in near-wall regions and *k*-ε performs best in shear type flows. The transport equations for turbulent kinetic energy and specific dissipation in *k*-ω SST model has the following form:

$$\frac{\partial k}{\partial t}+U_j\frac{\partial k}{\partial x_j}=P_k-\beta^* k\omega+\frac{\partial}{\partial x_j}\left[\left(\nu+\sigma_k\nu_T\right)\frac{\partial k}{\partial x_j}\right] \tag{3-37}$$

$$\frac{\partial \omega}{\partial t}+U_j\frac{\partial \omega}{\partial x_j}=\alpha S^2-\beta\omega^2+\frac{\partial}{\partial x_j}\left[\left(\nu+\sigma_w\varpi_T\right)\frac{\partial \omega}{\partial x_j}\right]+2\left(1-F_1\right)\sigma_{\omega 2}\frac{1}{\omega}\frac{\partial k}{\partial x_i}\frac{\partial \omega}{\partial x_i} \tag{3-38}$$

The blending function F_1 used in this model that is responsible for switching between k-ε and k-ω, is defined as:

$$F_1=\tanh\left\{\left\{\min\left[\max\left(\frac{\sqrt{k}}{\beta^*\omega y},\frac{500\nu}{y^2\omega}\right),\frac{4\sigma_{\omega 2}k}{CD_{k\omega}y^2}\right]\right\}^4\right\} \tag{3-39}$$

In this equation, y is the normal distance from the wall, and the CD_{kw} is defined by the following equation:

$$CD_{kw}=\max\left(s\rho\sigma_{\omega 2}\frac{1}{\omega}\frac{\partial k}{\partial x_i}\frac{\partial \omega}{\partial x_i},10^{-10}\right) \tag{3-40}$$

The source term seen on the right-hand side of the k transport equation has the following form:

$$P_k=\min\left(\tau_{ij}\frac{\partial U_i}{\partial x_j},10\beta^* k\omega\right) \tag{3-41}$$

Remaining coefficients seen in these equations are obtained through this equation. These coefficients are blended forms of k-ω and k-ε coefficients:

$$\phi=\phi_1F_1+\phi_2\left(1-F_1\right) \tag{3-42}$$

In this equation ϕ_1 corresponds to coefficients from k-ω equation and ϕ_2 represents coefficients from k-ε equation. The values of these coefficients are listed in the following table:

Table 3-2 Closure coefficients for *k*-ω SST turbulence model

α_1	α_2	β_1	β_2	$\beta*$	σ_{k1}	σ_{k2}	σ_{w1}	σ_{w2}
5/9	0.44	3/40	0.0828	0.09	0.85	1	0.5	0.856

Finally, the turbulent viscosity is obtained from:

$$\nu_T = \frac{a_1 k}{\max\left(a_1\omega, SF_2\right)} \tag{3-43}$$

F_2 is calculated from the following equation:

$$F_2 = \tanh\left[\left[\max\left(\frac{2\sqrt{k}}{\beta^*\omega y}, \frac{500\nu}{y^2\omega}\right)\right]^2\right] \tag{3-44}$$

Menter, et al. [43, 44] proposed two additional transport equations for intermittency and transition onset Reynolds number, which interacts with *k*-ω SST model through correcting the production term in the *k* transport equation. This model has been widely tested against numerous experimental measurements, especially turbomachinery data, and is reported to have good correspondence. More detail regarding this transitional method is given in section 3.3.8 γ-$Re\theta$ Model.

3.2.3.4 *k*-ω SST CC Model

Eddy viscosity models are insensitive to streamline curvature. To account for the effects of streamline curvature, Spalart and Shur [117] suggested an empirical correction function, f_r, to be used as a multiplier of the production term. This multiplier function is obtained through these expressions:

$$f_{rotation} = (1 + c_{r1}) \frac{2r^*}{1 + r^*} \left[1 - c_{r3} \tan^{-1}(c_{r2} \tilde{r}) \right] - c_{r1} \quad \textbf{(3-45)}$$

$$\tilde{f}_r = \max\left\{ \min(f_{rotation}, 1.25), 0 \right\} \quad \textbf{(3-46)}$$

$$f_r = \max\left[0, 1 + C_{scale}(\tilde{f}_r - 1) \right] \quad \textbf{(3-47)}$$

3.2.3.5 *k*-ω SST RM Model

RANS models are developed for fully attached flow simulations or mildly separated. In cases where there exists a rather large separation region, RANS models often under-predict turbulence stress levels. To correct this deficiency, Reattachment Modification (RM) model was introduced to enhance turbulence levels in separating shear layers. RM model adds a source term to the right-hand side of the *k* transport equation in SST model. The source term has the following description:

$$P_{RM} = P_K \min\left[4 \times \max\left(0, \frac{\min(S^2, \Omega^2)}{0.09\omega^2} - 1.6 \right), 1.5 \right] F_{LR} \quad \textbf{(3-48)}$$

F_{LR} prevents interaction between RM model and laminar-turbulent transition models and has the following form:

$$F_{LR} = \tanh\left[\left(\frac{k}{\omega \nu C_{LR}} \right)^2 \right] \quad \textbf{(3-49)}$$

In this equation, C_{LR} is an adjustable coefficient and could be altered based on the application. By default, it assumes the value of 10.0.

3.3 Transition Models

Laminar-turbulent flow transition is a highly complicated process, and all the aspects regarding this phenomenon have not yet been fully understood. Numerous

correlations have been proposed over the years to describe the behavior of the transitional flow under certain flow conditions. Laminar-turbulent boundary layer transition models in RANS could be categorized into two main categories based on the fact that they have incorporated the boundary layer stability theorem.

3.3.1 e^N Model

Smith and Gamberoni [118] along with Van Ingen [119] introduced the first version of e^N model to be used for predicting transition of incompressible two-dimensional boundary layer method. This model is an example of Low-Reynolds Number(LRN) approach. In LRN turbulence models, the whole turbulent boundary layer including the viscous sublayer is solved and thus incorporating wall functions is avoided [120]. The viscous sublayer is computed using no-slip boundary condition.

This model calculates the growth of disturbance amplitude. The factor N would be the total growth rate of the most unstable disturbance [121]. It involves calculating the laminar velocity, and the temperature profiles followed by computing the amplification factor of the most destabilizing wave among all velocity profiles. Finally, the transition onset location is calculated from amplification rates. The major drawback of this model is the fact that it has limited capability in-terms of predicting the transition caused by non-linear effects. Also, it is recommended to couple the Navier-Stokes solver with a boundary layer code since they are usually not accurate enough to evaluate the stability equations [47, 120, 122, 123]. Additionally, the exponent N is not universal and normally is correlated using experimental data. For that reason, e^N model is usually considered as a semi-empirical model.

3.3.2 Baldwin-Lomax Transitional Model

As said before, this is a zero-equation model which calculates the eddy viscosity based on local velocity profile [124]. Transition modeling capability here is achieved by zeroing the eddy-viscosity in the laminar flow and switching it back on at the onset of transition.

3.3.3 Warren, Harris and Hassan One-Equation Model

This one-equation model uses the intermittency distribution of Dhawan and Narasimha [39]. It incorporates first-mode (Tollmien-Schlichting) waves along with the effects of second mode disturbance and defines turbulent length-scale using first and second mode length-scales, which are based on experimental correlations.

3.3.4 Cho and Chung Model

Cho and Chung [37] proposed a transport equation for intermittency and incorporated it in k-ε turbulence model. The turbulent eddy viscosity is then calculated using a closure equation. The proposed transport equation is developed considering the entrainment effect on the intermittency in the free boundary of shear layers. Cho-Chung transport equation has the following format:

$$U_j \frac{\partial \gamma}{\partial x_j} = D_g + S_g \qquad \textbf{(3-50)}$$

In this equation, D_g represents the spatial transport of intermittency factor due to velocity jump between the two fluid.

$$D_g = \frac{\partial}{\partial x_j}\left[-\gamma\left(1-\gamma\right)\left(\tilde{\overline{U}}_j - \overline{\tilde{U}}_j\right)\right] \tag{3-51}$$

This term could turn into a diffusion term in-case the Lumley's velocity jump model [125] is applied.

$$D_g = \frac{\partial}{\partial x_j}\left[\left(1-\gamma\right)\frac{\nu_t}{\sigma_g}\frac{\partial \gamma}{\partial x_j}\right] \tag{3-52}$$

S_g in equation (3-50) represents the conversion rate of the irrotational fluid to the turbulent fluid. It would be the summation of source term proposed by Libby [126], later modified by Byggstøyl and Kollmann [127], and the interaction between the mean velocity gradient and the intermittency field.

$$S_g = C_{g1}\gamma\left(1-\gamma\right)\frac{P_{k,s}-P_{k,n}}{k} + C_{g2}\frac{k^2}{\varepsilon}\frac{\partial \gamma}{\partial x_j}\frac{\partial \gamma}{\partial x_j} - C_{g3}\gamma\left(1-\gamma\right)\frac{\varepsilon}{k}\Gamma \tag{3-53}$$

In this equation, $P_{k,s}$ and $P_{k,n}$ are the production of turbulent kinetic energy by shear and normal strains respectively. Also, Γ is the amount of intermittency entrained by the interaction between the mean velocity gradient and the intermittency filed per unit volume of fluid.

3.3.5 Steelant and Dick Model

Steelant and Dick [38] proposed a transport equation for intermittency to simulate bypass transition. They took into account the transition using the conditioned averages during the fraction of time the flow is laminar or turbulent. This model is derived in such a way to reproduce the streamwise intermittency distribution of Dhawan and Narasimha [39]. This model that is derived for a unidirectional flow over a flat plate, assumes the following form:

$$\frac{\partial \rho\gamma}{\partial t} + U\frac{\partial \rho\gamma}{\partial x} = 2f(1-\gamma)\sqrt{-\ln(1-\gamma)}\beta\rho U \quad \textbf{(3-54)}$$

In addition, it is equipped with a function, f, that can produce the distributed breakdown of intermittency as opposed to sudden production of γ at the onset location of intermittency. The effect of the pressure gradient in this model is included in the term β. It assumes different values at different pressure gradients.

3.3.6 Suzen and Hung Model

Suzen and Huang [40] combined two intermittency transport equations of Cho and Chung [37] and Steelant and Dick [38] in order to get the best of the two models. Steelant and Dick [38] model reportedly performs superior in near-wall regions, and the Cho and Chung [37] model is more suitable for free shear flows.

In this model, the turbulent eddy viscosity for transitional flow is obtained by multiplying the intermittency factor and turbulent eddy viscosity. To calculate other turbulent flow quantities, Menter's SST model [42] was used. In order to locate the onset of transition, this model uses the correlation of Huang and Xiong [128].

3.3.7 Durbin Model

Durbin [49] introduced an intermittency transport equation for the purpose of bypass transition modeling. This transport equation is based on local variables and the transition, unlike the conventional models, is initiated by the diffusion of freestream into the boundary layer and also source term. The source term is a function of vorticity Reynolds number as well as the ratio of eddy viscosity to molecular viscosity and is prevented from switching on prematurely. This model is then integrated into the k-ω model and implemented in a RANS based solver.

3.3.8 *γ-Reθ* Model

In this model that is proposed in Refs [43, 44], two additional transport equations are solved. First transported parameter is the intermittency factor γ and the second one is the momentum thickness Reynolds number $Re_{\theta t}$.

$$\frac{\partial(\rho\gamma)}{\partial t}+\frac{\partial(\rho U_i\gamma)}{\partial x_j}=P_{\gamma 1}-E_{\gamma 1}+P_{\gamma 2}-E_{\gamma 2}+\frac{\partial}{\partial x_j}\left[\left(\mu+\frac{\mu_t}{\sigma_f}\right)\frac{\partial\gamma}{\partial x_j}\right] \tag{3-55}$$

$$\frac{\partial(\rho \mathrm{Re}_{\theta t})}{\partial t}+\frac{\partial(\rho U_j \mathrm{Re}_{\theta t})}{\partial x_j}=P_{\theta t}+\frac{\partial}{\partial x_j}\left[\sigma_{\theta t}(\mu+\mu_t)\frac{\partial \mathrm{Re}_{\theta t}}{\partial x_j}\right] \tag{3-56}$$

The transition sources in equation (3-55) are:

$$P_{\gamma 1}=F_{length}\rho S\left[\gamma F_{onset}\right]^{C_{a1}} \tag{3-57}$$

$$E_{\gamma 1}=c_{e1}P_{\gamma 1}\gamma \tag{3-58}$$

S is the strain rate magnitude in equation (3-57). F_{onset} in the same equation is obtained through the following equations:

$$\mathrm{Re}_v=\frac{\rho y^2 S}{\mu} \tag{3-59}$$

$$F_{onset1}=\frac{\mathrm{Re}_v}{2.193\mathrm{Re}_{\theta c}} \tag{3-60}$$

$$F_{onset2}=\min\left[\max\left(F_{onset1}^4, F_{onset1}\right), 2.0\right] \tag{3-61}$$

$$R_T=\frac{\rho k}{\mu\omega} \tag{3-62}$$

$$F_{onset3}=\max\left[1-\left(\frac{R_T}{2.5}\right)^3, 0\right] \tag{3-63}$$

$$F_{onset} = \max\left(F_{onset2} - F_{onset3}, 0\right) \tag{3-64}$$

$Re_{\Theta C}$ is the critical Reynolds number in equation (3-60) that reflects the location at which intermittency first starts to rise.

The production term in equation (3-56) is obtained through the following equations:

$$P_{\theta t} = c_{\theta t}\frac{\rho}{t}\left(\mathrm{Re}_{\theta t} - \tilde{\mathrm{R}}\mathrm{e}_{\theta t}\right)\left(1.0 - F_{\theta t}\right) \tag{3-65}$$

$$t = \frac{500\mu}{\rho U^2} \tag{3-66}$$

$$F_{\theta t} = \min\left\{\max\left[F_{wake}e^{-(y/\delta)^4}, 1.0 - \left(\frac{\gamma - 1/c_{e2}}{1.0 - 1/c_{e2}}\right)^2\right], 1.0\right\} \tag{3-67}$$

$$\delta = \frac{375\Omega y}{U}\frac{\tilde{\mathrm{R}}\mathrm{e}_{\theta t}\mu}{\rho U} \tag{3-68}$$

$$\mathrm{Re}_{\omega} = \frac{\rho\omega y^2}{\mu} \tag{3-69}$$

$$F_{wake} = e^{-\left[\mathrm{Re}_{\omega}/(1E+5)\right]^2} \tag{3-70}$$

The model constants for transport equations are listed the following table:

Table 3-3 model constants

$C_{\theta t}$	0.03
$\sigma_{\theta t}$	10.0

The production and destruction terms in k transport equation, P_k and D_K respectively, are then corrected through the following equations:

$$\tilde{P}_k = \gamma P_k \tag{3-71}$$

$$\tilde{D}_k = \min\left(\max\left(\gamma_{eff}, 0.1\right)1.0\right)D_k \tag{3-72}$$

γ–$Re\theta$ model, although is not physics-based, is the most popular transitional model being used in RANS approach. It does not intend to model the physics of the problem, instead, it attempts to fit a wide range of experiments into its formulations [43].

4 COMPUTATIONAL RESEARCH OBJECTIVES

As mentioned earlier, Computational Fluid Dynamics plays an undeniable role in the design process of turbomachinery components. Reliability of CFD results is dependent upon some parameters such as meshing, boundary condition selection, turbulence and transition modeling.

This study aims at numerically investigating the flow quantities around a turbine blade that has been previously experimentally studied. By doing so, one can study the trends exhibited between predicted versus measured performance of the blade. This will reveal the advantages and weaknesses of the current CFD tools. Additionally, a more detailed look will be taken at the accuracy of transition model and intermittency distribution in a wake-flow condition. To numerically simulate the transitional behavior of the boundary layer under periodic unsteady flow condition, a new intermittency transport equation is proposed which is based on the universal intermittency function developed by Chakka and Schobeiri [1]. Accurate prediction of the boundary layer behavior under the operating conditions requires minimum and maximum intermittency functions. These functions were developed inductively using the experimental results that were obtained in the absence of flow separation. In this study, the impact of the separation on the minimum and maximum intermittency are addressed. The enhanced minimum and maximum intermittency functions along with the universal intermittency are implemented in a RANS based solver for computational simulation. The details of research objectives are listed below:

4.1 Grid Generation

- Create a high quality structured grid for the linear turbine blade cascade of high-pressure and low-pressure turbine blade, and the moving rods:
  - Ensure about the high quality of the grid at near wall regions. y^+ of less than one is ensured in order to resolve viscous sub-layer inside the boundary layer successfully.
  - Ensure about grid independency of the results.

4.2 Steady State Modeling

- Performs steady state simulation of flow inside the linear cascade of LPT blades using $\gamma-Re_\theta$ turbulence model.
- Compare the obtained data from CFD simulations with previously measured data from experiments.
- Discuss the effect of aerodynamics on heat transfer.
- Evaluate the performance of transitional SST turbulence modeling on calculated flow quantities and heat transfer in steady state flow at different working conditions.

4.3 Transient Modeling

- Perform time accurate, transient numerical simulation of unsteady flow inside the linear cascade of LPT blades using the $\gamma-Re_\theta$ turbulence model.
- Evaluate performance of time-averaged results of $\gamma-Re_\theta$ turbulence model when compared with steady-state analysis results and experimental data.
- Discuss the effect of aerodynamic parameters on heat transfer in unsteady wake-flow.

4.4 Transition Modeling

- Deriving a new physics-based intermittency transport equation for an unsteady periodic wake-flow condition.
- Implement the transport equation for universal intermittency function into the solver and discuss the reliability of the results by comparing them with Langtry-Menter intermittency results and also experimental data.
- Evaluate the performance of universal intermittency function in conjunction with transitional turbulence modeling on flow quantities and heat transfer in unsteady wake –flow condition.
- Discuss the future path regarding transition modeling in turbomachinery.

5 LOW-PRESSURE TURBINE BLADE CASCADE STUDY

This chapter[1] focuses on numerical simulation of flow around a low-pressure turbine blade in a linear subsonic cascade facility. The following contains details about numerical simulation, grid generation, and numerical results.

5.1 Numerical Simulation

Three-dimensional steady (RANS) and unsteady (URANS) calculations were carried out for the linear low-pressure turbine blade cascade facility using a commercial RANS-based solver, ANSYS CFX v17.1. Figure 5-1 depicts the computational domain and the corresponding boundary conditions for CFD simulations. The geometric information is taken exactly from the cascade facility for the simulations to be the identical representation of the working condition in the cascade facility.

As seen, the model consists of two separate domains, one stationary that includes

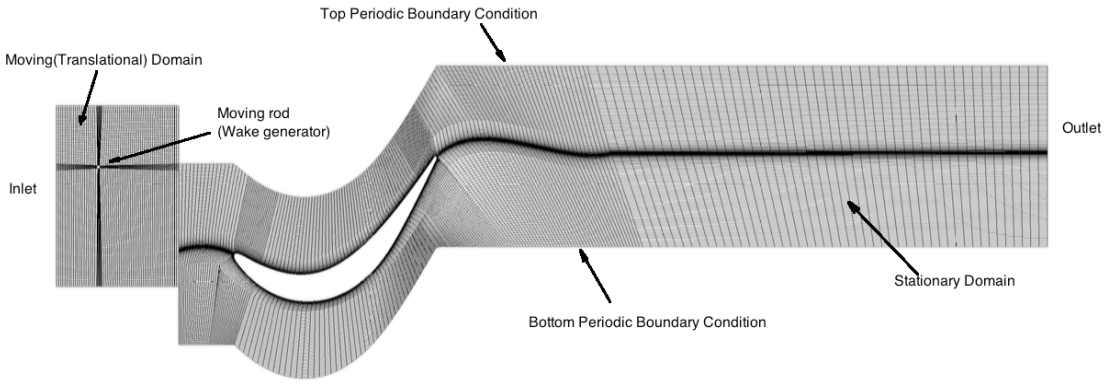

Figure 5-1 Computational domain and boundary conditions for LPT blade linear cascade facility

[1] Part of the data reported in this chapter and the next is reprinted with permission from Ref [129] A. Nikparto and M. T. Schobeiri, "Combined numerical and experimental investigations of heat transfer of a highly loaded low-pressure turbine blade under periodic inlet flow condition," *Proceedings of the Institution of Mechanical Engineers, Part A: Journal of Power and Energy,* p. 0957650918758158, 2018.

the blades, and the other one is a moving domain that includes the rods. All of the interfaces between the components except for the one between stationary and moving domain (the interfaces defined in pitch-wise direction for periodic boundary condition for both domains) are using mixing-plane method. The boundary conditions are defined according to the corresponding experimental data. At the inlet of the cascade, the static and total pressures are measured as well as the turbulence intensity. Simulations are performed to obtain heat transfer coefficient at different locations and aerodynamic flow quantities.

For this study, ANSYS CFX v17.1 was used. This solver is a finite-element-based finite-volume solver. Since the Mach number is relatively low, the air is treated as an incompressible fluid in these simulations. High-resolution scheme is used to discretize the convection term, and as for the temporal term, second-order backward Euler method was used. Each simulation under the aforementioned conditions and method requires 8.6×10^{6} CPU seconds to fulfill, which is equivalent to 24hrs on the available computational platform.

5.1.1 Mesh Generation

ANSYS ICEM was used to produce the computational grid. The domain is composed of 650,000 elements. It consists of hexagonal elements and the regions near blade surfaces have a higher definition as well as the leading and trailing edges. The very fine grid in these regions ensures a y^{+} value of less than 1, which is necessary and sufficient to capture the viscous sub-layer. Also, since there exists a rather large separation bubble on the suction side of the blade under the working condition in which the measurements were performed, this region is intentionally set to be thick to enclose

the separation bubble. In the regions that are rather far from the blade surfaces, the elements are isotropic and hexagonal. A grid independency test was also performed. For that purpose, flow quantities at different Reynolds numbers and turbulence intensities were compared for different grids at critical conditions such as leading edge and separation zone. Figure 5-2 shows the computational domain.

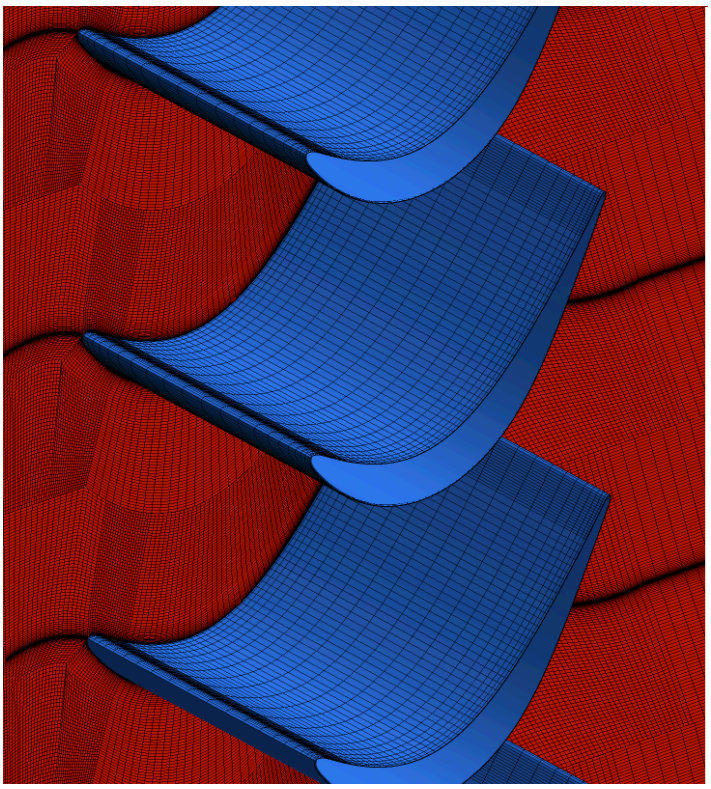

Figure 5-2 Computational domain in three-dimensions [129]

5.1.2 Boundary Conditions

Uniform velocity is prescribed to the inlet in the same direction as the incidence angle. Non-reflecting boundary condition is applied to the outlet of the computational domain, and periodic boundary conditions have been applied to both ends of the domain in the pitch-wise direction as shown in Figure 5-1.

5.1.3 Turbulence Model

Intermittency characterizes the transitional flow. The following equation exhibits the coordinate invariant form of the Navier-Stokes equation for transitional flow:

$$\frac{\partial \rho \bar{V}}{\partial t} + \left(\rho \bar{V}\right).\nabla \bar{V} + \nabla.\left(\gamma \rho \overline{V'V'}\right) = -\nabla \bar{P} + \mu \Delta \bar{V} + \rho g \qquad \textbf{(5-1)}$$

The third term on the right-hand side of the equation (5-1) is the product of Reynolds stress and intermittency factor. Incorrect prediction of the intermittency factor and Reynolds stress model would result in multiplicative error that will cause over/under-prediction of the flow quantities. The flow regime investigated in this study is of transitional nature, and correct prediction of the intermittency factor could increase the reliability of the computational results. The transition model incorporated in ANSYS CFX v17.1 solver is developed by Menter, et al. [43, 44]. In this model, a transport equation is proposed for intermittency and is integrated into SST turbulence model. Additionally, another transport equation is proposed for momentum thickness Reynolds number.

5.2 Numerical Results Analysis

Aerodynamics and Heat transfer are closely related subjects. Aerodynamics define the heat transfer characteristics, and correct prediction of aerodynamic flow quantities would decrease the typical gap between experimental and numerical results associated with numerical errors. Among aerodynamics flow quantities, velocity fluctuations are responsible for mass, momentum and energy transfer to the boundary layer.

Current simulations are performed at some select flow conditions. Simulations were performed at turbulence intensities of 1.9% and 13% at three reduced frequencies of Ω=0, 1.59 and 3.18 at three different Reynolds numbers.

5.2.1 Comparison To Experimental Measurements

5.2.1.1 Interaction of Aerodynamics and Heat-Transfer

To better understand the interaction between aerodynamics and heat-transfer, Figure 5-3 is compiled and presented here. This figure includes surface pressure distribution, velocity/velocity fluctuation profiles, and turbulence intensity as well as velocity magnitude contour plots.

Figure 5-3(a) shows the surface pressure distribution on the blade surfaces. On the suction surface of the blade, a strong negative (favorable) pressure gradient exists. This pressure gradient accelerates the flow until the minimum pressure point is reached. During this distance, the boundary layer is laminar and stable. Hence, it is incapable of transferring mass, momentum, and energy to the blade surface. In this region, we also witness a continuous drop in heat-transfer coefficient, consistent with the nature of the boundary layer. Immediately after the minimum pressure point, the flow experiences an equally strong positive pressure gradient, which tries to decelerate the flow. This fact results in an unstable boundary layer and finally separation. During this distance, heat transfer coefficient continues to drop until the level of turbulence inside the separation bubble rises (Figure 5-3(c)) [129].

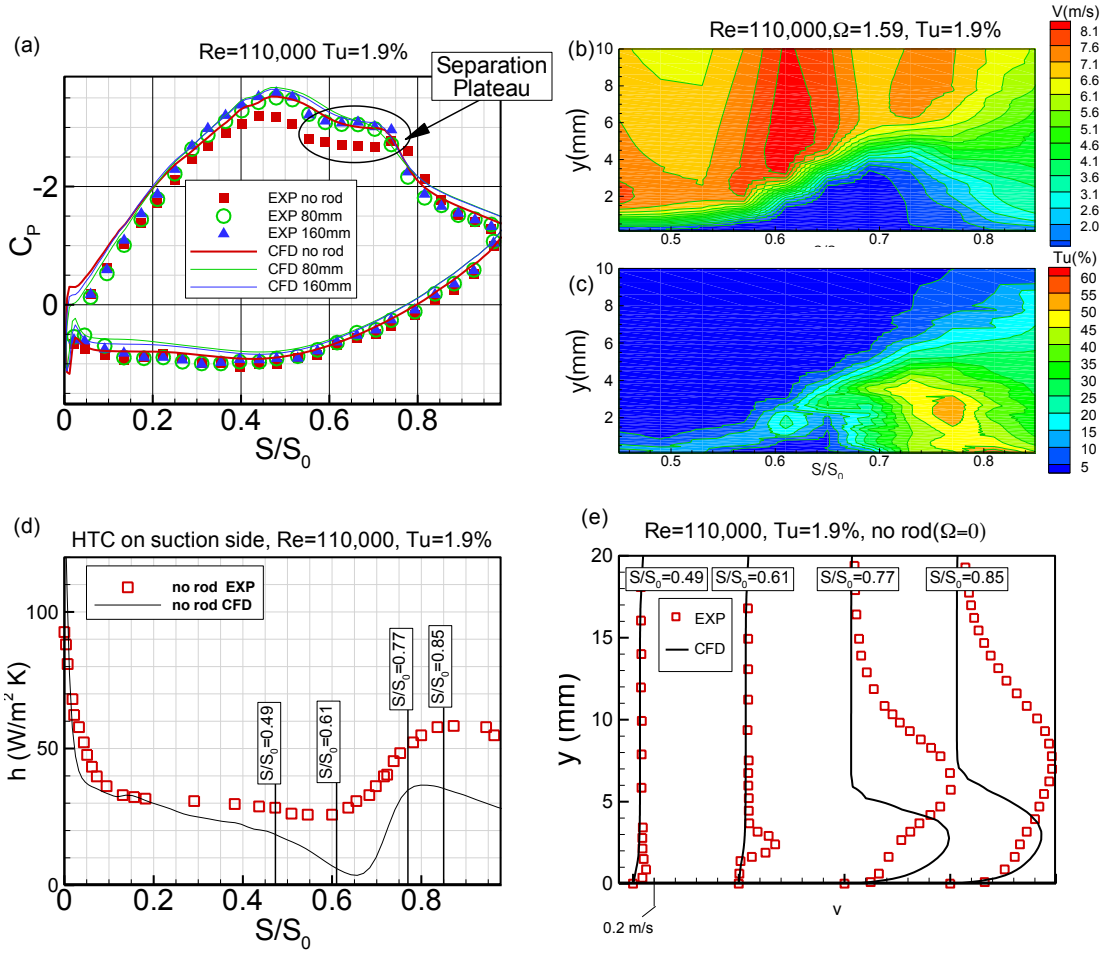

Figure 5-3 (a)Surface pressure distribution, (b) velocity and turbulence activity contour plots, (c) Heat Transfer Coefficient distribution and (d) Velocity fluctuation profiles. [129]

This fact is also reflected in Figure 5-3(e), the velocity fluctuation levels at locations S/S_0=0.77 and 0.85 is considerably larger than S/S_0=0.61. As a result, heat transfer coefficient starts to rise until immediately after the re-attachment location, where HTC experiences a local maximum. Figure 5-3(e) shows that inside the separation region, the velocity fluctuation level is highly under-predicted in the simulations. According to Prandtl hypothesis [130], the same pattern is expected in the lateral direction. Lower levels of fluctuation in simulations compared to measurements could only result in under-predicted HTC compared to the experiments.

Velocity fluctuations are responsible for transferring mass, momentum, and energy into the blade surface. Higher levels of fluctuations translate into a higher rate of momentum, energy exchange, and naturally higher heat transfer coefficient. Commercial solvers are relatively capable in-terms of predicting velocity profiles, while they normally fail to predict magnitudes of velocity fluctuations accurately. According to Figure 5-3(e), boundary layer initially does not show high levels of fluctuations, which is indicative of laminar flow. Even in the laminar flow regime, the solver fails to capture the fluctuation profile correctly. The discrepancy only rises as we enter the transitional and turbulent flow regime.

5.2.1.2 Effect of Turbulence Intensity

Figure 5-4 shows heat transfer coefficient distribution along the pressure surface and suction surfaces of the blade for unsteady flow cases. Figure 5-4(a) and (b) show HTC distribution at Tu=1.9% and 13% for Reynolds numbers of 110,000 and 250,000 respectively.

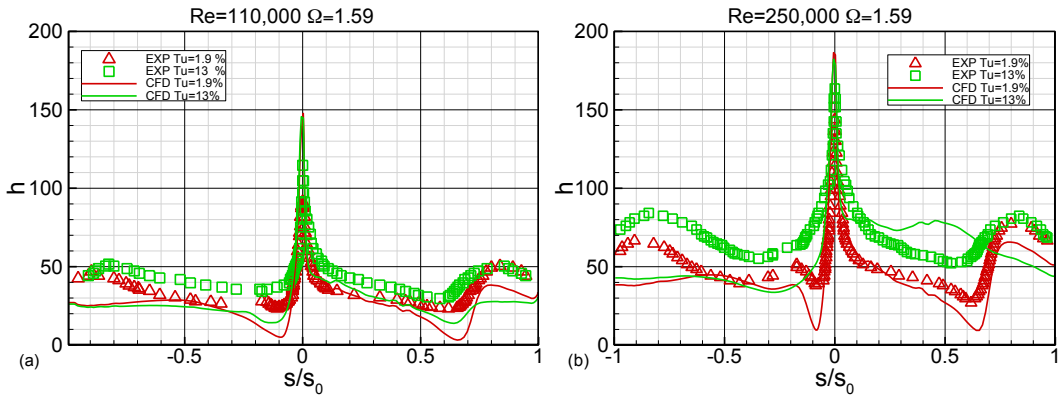

Figure 5-4 Effect of turbulence intensity on heat transfer coefficient for (a)Re=110,000 and (b)Re=250,000 [129]

In this figure, a systematic increase in heat transfer coefficient with turbulence intensity is observed. On the pressure side ($S/S_0<0$), HTC value drops sharply due to the low-energy nature of the laminar boundary layer. HTC rises immediately following the beginning of the transition. The sudden drop and increase in HTC value are more pronounced at higher Reynolds number (Figure 5-4(b)). The pattern of numerical simulation results is the same, mainly in laminar and transitional regions. The errors between numerical results and the experimental measurements are larger than the errors associated with aerodynamic flow quantities.

Figure 5-4 also reveals that the HTC undergoes another minimum at approximately between S/S_0=-0.43 and -0.5 depending on the Reynolds number in low turbulence intensity condition, which is not seen in the simulations. Additionally, the RANS solver predicts a constant value for HTC after the transition. This trend is not observed in measurements. This is because the intermittency function is shown to be incapable of increasing the fluctuation effects within the transitional boundary layer. Hence the HTC remains constant after reaching the transition onset.

Increasing the turbulence intensity has considerably boosted HTC value. This effect is more evident at higher Reynolds numbers. This trend could be best explained from aerodynamics point of view and random fluctuations in particular. The important observation here is the fact that presence of separation bubble has noticeably altered HTC pattern in low-turbulence intensity case while at higher *Tu*, this effect is not as clearly seen. Another important effect of increasing turbulence intensity would be the fact that the trace of transition, on either side of the blade, is completely washed out. The

minimum point on the pressure side that signifies the onset of transition at Tu=1.9%, is no longer present at Tu=13%, especially when Re=250,000.

On the suction side, the RANS solver is relatively successful prior to the boundary layer transition. The numerical results show good agreement with the experimental measurements and the discrepancies begin to show inside the transitional regime. At Reynolds number of 110000, the increase in turbulence intensity has suppressed the effect of flow separation, yet the solver is still capable of predicting separation and re-attachment. In high Reynolds number, the increase in turbulence intensity has completely washed-out separation in simulations, and the solver is predicting a completely attached flow, unlike the experiments [129].

5.2.1.3 Effect of Reynolds Number

The distribution of HTC at different Reynolds numbers and different turbulence intensities for reduced frequencies of Ω=1.59(S_R=160 mm) and Ω=3.18 (S_R=80 mm) is shown in Figure 5-5. As stated before, increasing the Reynolds number has caused an increase in HTC. This increase influences laminar portion of the boundary layer and subsequently the transitional portion.

Figure 5-5(a) proves that the RANS solver successfully calculates the heat-transfer coefficient in the laminar portion of the suction surface. Increase in the Reynolds number has not produced any deficiency in this regard as seen in Figure 5-5(b). The deficiency is seen once turbulence intensity is increased. Figure 5-5(c) and (d) prove this fact. Disagreement between measurements and calculation become more pronounced in these figures. The solver could not even predict a separated flow in this flow condition.

This deficiency is due to the ineffectiveness of the built-in intermittency function of ANSYS-CFX and the corresponding transport equation of intermittency. In numerical simulations, the turbulence intensity and the length scale at the inlet of the domain is manually altered to match the turbulence intensity of experimental cases at the same location. Yet, the transport equation of intermittency fails to transport fluctuations correctly [129].

5.2.1.4 Effect of Reduced Frequency

The effects that unsteady wakes have on heat transfer coefficient are shown in Figure 5-6. Measurements and simulations are done for reduced frequency of Ω=0.0(S_R=∞), 1.59(S_R=160 mm) and 3.18(S_R=80 mm). At turbulence intensity of 1.9%,

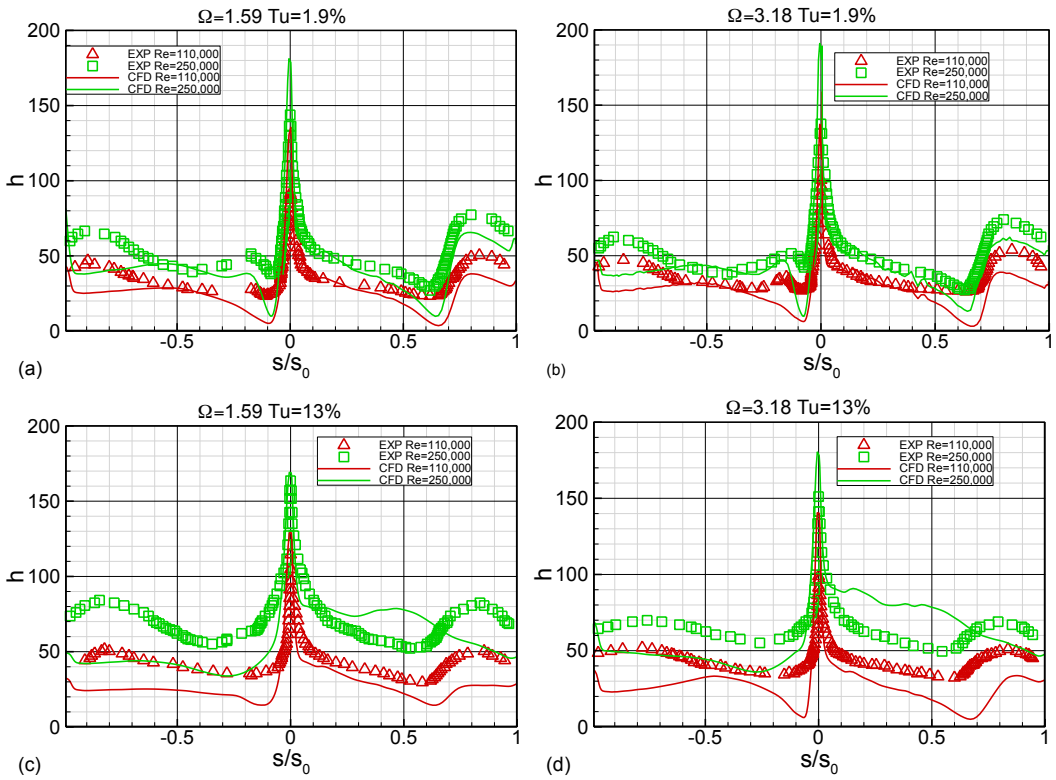

Figure 5-5 Effect of Reynolds number on unsteady heat transfer coefficient at (a)Tu=1.9% and Ω=1.59, (b) Tu=13% and Ω=3.18 [129]

unsteady wakes have only marginally changed HTC on the suction side of the blade. The same trend is observed in numerical simulation results.

They show an almost negligible sensitivity to reduced frequency, yet both sets of results show that unsteady wakes have suppressed the separation bubble to some extent. Unlike the suction surface, on the pressure surface a more noticeable difference is observed between the experimental and numerical simulations as unsteady wakes have transported the transition onset upstream. As turbulence intensity rises, numerical simulations show higher sensitivity to wake passing frequency in laminar region (Figure

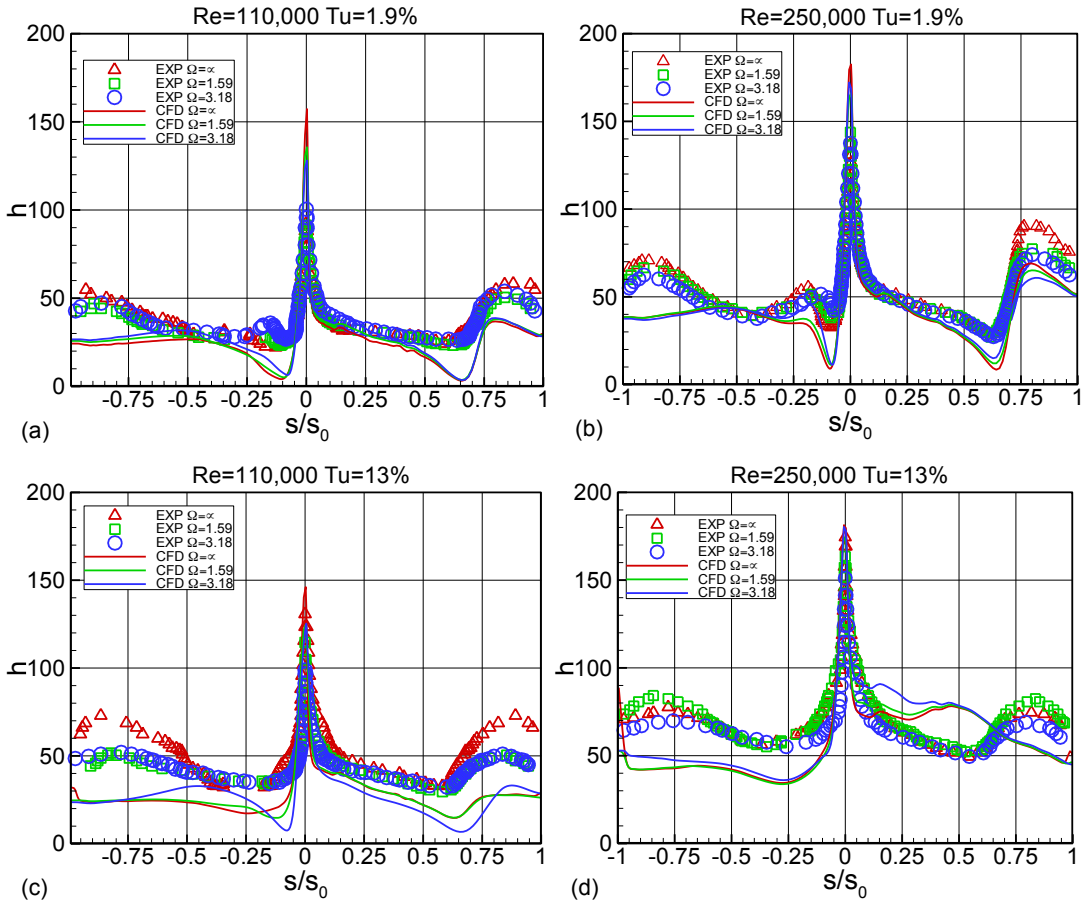

Figure 5-6 Effect of unsteady wake on heat transfer coefficient at (a) Re=110,000 Tu=1.9% (b) Re=250,000 Tu=1.9% (c) Re=110,000 Tu=13% and (d) Re=250,000 Tu=13% for unsteady inlet flow condition with Ω=0.0, 1.59 and 3.18 [129]

5-6(c) and (d)). While experimental measurements, regardless of wake passing frequency, show almost the same magnitude in this region.

Increasing turbulence intermittency to 13%, has caused the transitional region on the pressure surface to be completely washed out. This produces a rather different HTC pattern. In this case, computational results show higher sensitivity to wake passing frequency compared to low turbulence intensity case. This shows that the turbulence length scale in high turbulence intensity cases have failed to submerge the incoming wakes and for that reason, the turbulent vortical core, produced by moving rods, can significantly affect the HTC distribution.

In high-turbulence intensity test case (Tu= 13%, Re=110,000), there is a considerable difference between suction surface measurements under steady and unsteady flow conditions while there barely is any difference between the two unsteady measurements. This finding might be inconsistent with the general perception that unsteady wakes always add to the level of turbulence in the system and for that reason, cause an increase in HTC value. In this case, the effect of calm region prevails, and as a result, heat transfer coefficient has dropped.

The RANS solver produces inconsistent behavior at high turbulence intensity(13%) for the two Reynolds numbers. In the case of lower Reynolds number, the solver can capture the calming effect on the suction side and subsequently, HTC is lower at Ω=3.18, while completely opposite trend is observed for Re=250,000. Another major inconsistency observed in CFD results is the fact that HTC is correctly predicted in the laminar region at low-turbulence intensity as opposed to high turbulence intensity, where the solver fails to predict the HTC in laminar region correctly [129].

5.3 LPT Cascade Simulation, Discussion

In this chapter, a commercial RANS solver was used to analyze the three-dimensional flow inside a linear cascade for steady and unsteady flow conditions. A comparison was made in all cases with the corresponding measurements. In most cases, CFD results show rather large discrepancies and disagreements with experimental measurements. Namely, the velocity fluctuations at select locations were significantly under-predicted and in-terms of velocity profile, they showed the largest disagreement in the boundary layer. The overall under-prediction of velocity fluctuations resulted in smaller HTC prediction in most cases.

In general, a major source of discrepancy between CFD results and measurements, in the opinion of the author, is the mixing-plane method that is normally used between the stationary and the moving domain. As described by Denton [131], the mixing plane is needed to mix out the upstream wake dominated flow to a uniform enthalpy and entropy in pitch-wise direction. The mixed-out flow is then prescribed as the inlet flow for the downstream domain. Mixing plane could potentially wash out the upstream wake by circumferentially averaging the flow quantities and imposing the mixed average profile on the subsequent stationary domain. There is always an entropy increase associated with mixing plane. To counter that effect, the stationary and moving domains were produced to have identical areas. The mixing plane will eliminate any circumferentially based effect. An example of which, would be wakes originated from upstream rods. Using mixing-plane, these parameters would then diffuse or mix out. For that reason, it adds to the level of uncertainty in the RANS modeling. To avoid the problems associated with

implementation of mixing plane, in the current simulations, transient stator-rotor model has been used for URANS modeling.

5.3.1 Modeling Errors

Computational errors are due to the approximations used in the computational process such as truncation error and round off error. Another source of error are the use of artificial viscosity that is used to stabilize the solution. Also, linear interpolation between flow quantities across grid points is another source of error. This could be amplified with larger spacing (larger grid elements). For this reason, finer grid and smaller spacings are required especially in the regions with high flow gradients. An example of these regions would be the leading edge, trailing edge and near-wall zones. The computational errors associated with grid density behave like an additional source of viscosity. Hence, it produces false entropy that could very well be transported downstream and affect the solution further.

5.3.2 Turbulence Modeling

To fully describe turbulence via modeling, a grid with very high resolution is required that can resolve the smallest scale vortices. This is what is done in DNS method and also LES. The downside of this method is the very high computational cost required to perform such simulations. With the current computational platforms, these methods are still not practical for turbo-machinery design purposes. The alternative would be turbulence modeling in RANS/URANS solvers that can provide almost accurate results within a reasonable timeframe. Turbulence models should be calibrated to give good flow predictions. In the case of unsteady separated flow, most turbulence models fail to predict the flow physics correctly. The Langtry-Menter transitional model that has been used in

this study (transitional SST), reportedly works well with fully attached flow, yet under-predicts separation region and for that reason over-predicts the blade performance.

5.3.3 Transition Modeling

Transition modeling plays a large part in predicting turbine blade performance. Boundary layer scale and entropy generation are directly correlated. Most CFD solvers are capable of predicting the boundary layer growth for fully laminar or turbulent flow. But they normally fail in transitional regime. There are some reasons that contribute to this fact, such as the turbulence intensity and length scale at the inlet, surface curvature, and pressure gradient. Flow separation is normally observed in off-design conditions, especially at low-Reynolds numbers and rather low turbulence intensity levels. Separated flow normally attaches to the blade at a downstream location. Flow separation is influenced by factors such as turbulence intensity and of-course the unsteady wakes that could move transition onset upstream. This effect is extensively studied by Chakka and Schobeiri [1].

Most transition models incorrectly predict the location and the size of the flow separation. Transition modeling gets more complicated considering the near-wall and 3-Dimensional effects. Also in some cases, the boundary layer might transition back to laminar state [56]. In Figure 5-7, turbulence intermittency contour plots are shown. As seen in this figure the intermittency distribution around the blade is affected by the inlet flow conditions. Higher turbulence intensity and Reynolds number have tripped the transition earlier.

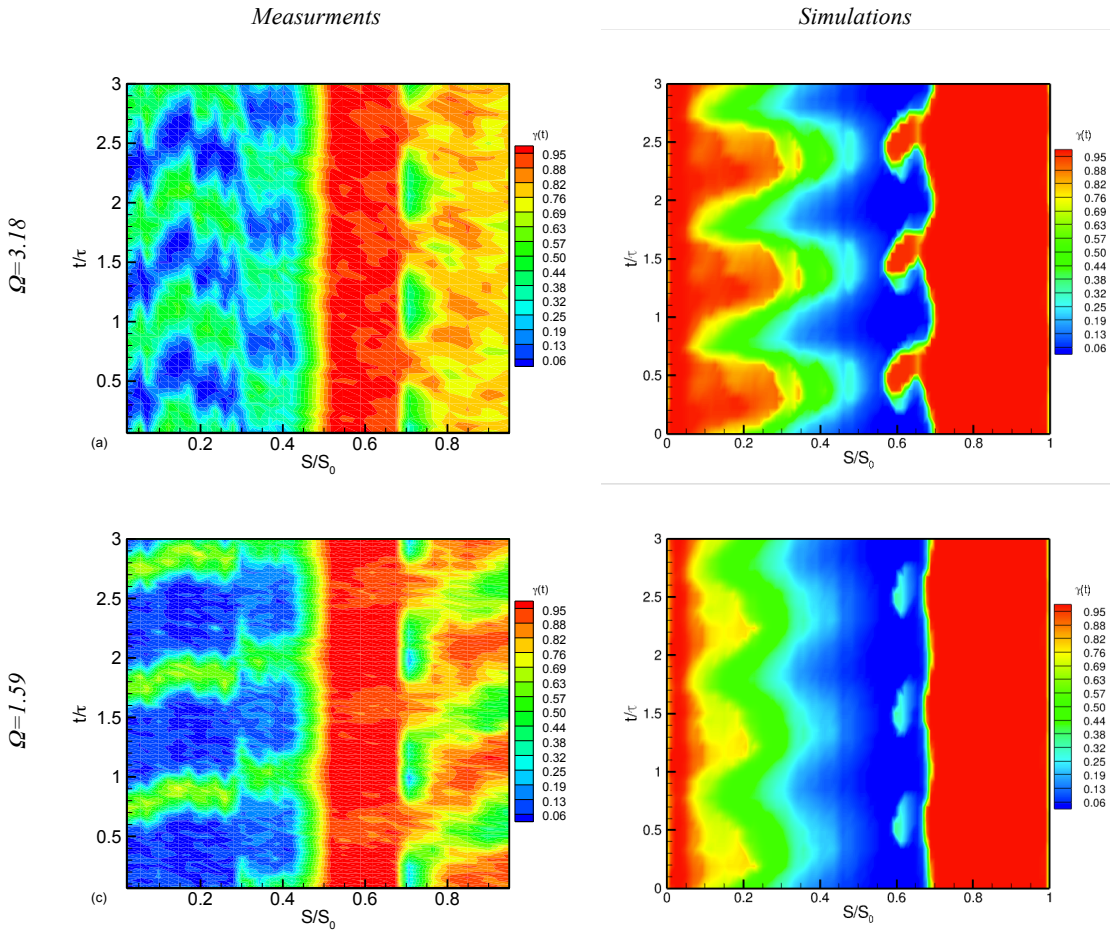

Figure 5-7 Turbulence intermittency contour plots obtained from measurements and simulations for unsteady frequencies of 1.59 and 3.18

5.3.4 Experimental Consideration

There are a few considerations when it comes to comparing computational results against experimental measurements. The most important subject is the validity of assumptions regarding boundary conditions used in the computational model. Regarding the inlet flow condition, since in experimental measurements, five-hole probe and X-hotwire were used, the turbulence intensity was measured accurately as well as turbulence length scale. Uniform velocity was prescribed at the inlet with corresponding turbulence intensity/length-scale.

In the current study, the surfaces of the blade are assumed to be completely smooth. The surface roughness plays an important role in boundary layer growth and transition to turbulent state. All the blades used for experimental measurement purposes were newly manufactured and sanded. For that reason, the surface roughness must be in the order of a few microns, but it would be really hard and impossible to measure the roughness at all locations and all times.

The other important consideration is the uncertainty in measurements. As stated in Ref [132], uncertainty in velocity measurement increases as the velocity decreases. This is mostly due to uncertainty in pressure transducers used in the calibration stage. The same trend is observed in heat-transfer measurements. The uncertainty of liquid crystal method decreases with increase in HTC value. But overall HTC measurements have an average uncertainty of 4.5%.

CFD solvers have remained an inseparable part of turbomachinery element design cycle, even though there are some inherent errors associated with them. They have gained popularity since they can boost the understanding of turbomachinery flow physics. However, CFD still has so many deficiencies to overcome. As has been confirmed before[131, 133], CFD must be used more as a comparative tool rather than a reliable predictor of performance. Experimental measurements will still be required to produce benchmarks used for improving the reliability of CFD codes.

6 DERIVATION AND IMPLEMENTATION OF NEW TRANSITION MODEL

6.1 Unsteady Intermittency

Section 3.3 discusses some of the popular transition models being used in CFD, which have obtained rather limited success. The following section focuses on the derivation and implementation of a physics-based intermittency transport equation that can be implemented in commercial RANS solvers.

6.1.1 Transport Equation of γ, Model Formulation

Section 2.3 thoroughly discusses the universal intermittency function. This section is dedicated to the derivation of a transport equation for universal intermittency function. According to the universal intermittency function [1, 2], the flow intermittency would vary for locations whether they are inside or outside of the wake vortical core. As the wakes impinge on the surfaces, turbulence intermittency rises almost instantly and drops immediately due to calming effect after the wake passes. Universal intermittency function formulation successfully defines this unique characteristic of unsteady periodic wake-induced flow. The relative intermittency function has a Gaussian distribution with respect to lateral distance for all locations. The Gaussian distribution is expressed in-terms of ζ in in Equation (2-8) and is shown in Figure 2-9.

The transport equation for intermittency used for this study is physics based and is derived based on the measurements in TPFL. The cascade facility and the flow condition in which the measurements were performed, were described in Chapter 9 (Table 9-2). Under this flow condition, the measurements revealed that the intermittency distribution in the stream-wise direction on the suction side of the blade would be as depicted in this picture.

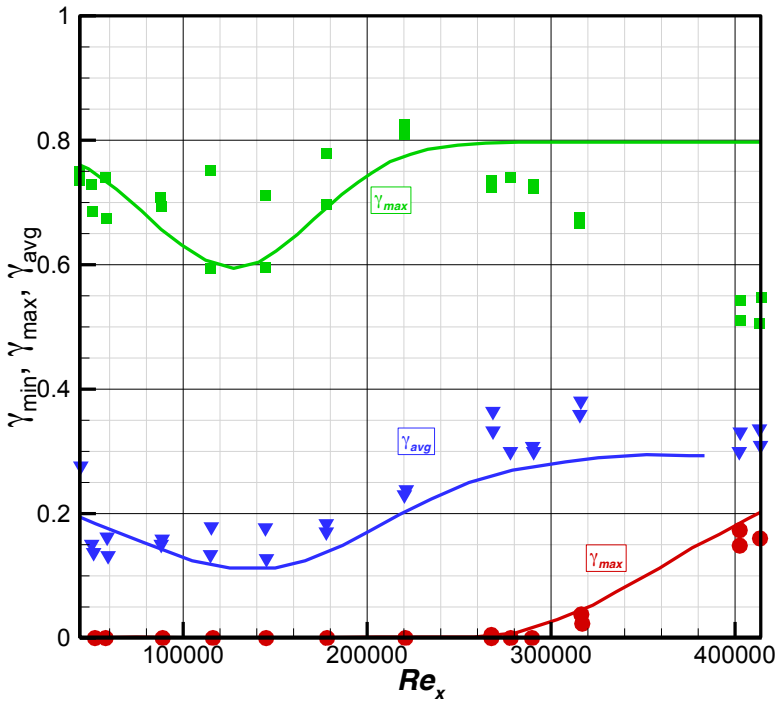

Figure 6-1 Minimum, maximum and time-averaged intermittency distribution on the suction surface of the HPT blade as a function of axial Reynolds number for Ω=0.755 [2]

The discrete data points are obtained from measurements, and the solid curves represent equations (2-9), (2-10) and (2-11).

The intermittency transport equation used here is:

$$\frac{\partial \gamma}{\partial t} + V.\nabla\gamma = D_\gamma + P_\gamma - E_\gamma \qquad \textbf{(6-1)}$$

The three terms seen on the right-hand side of this equation are the diffusion, production and dissipation terms respectively. The source term in this equation is derived in such a way that it can reproduce the same stream-wise intermittency distribution as shown in Figure 6-1. The source term would cause the intermittency to vary at each location from γ_{min} to γ_{max}. Hence, the source term would have to be composed of one

temporal term and one spatial term. For that purpose, equation (2-7) is re-written in the following form:

$$\gamma = \left(\gamma_{\max} - \gamma_{\min}\right) e^{-\zeta^2} + \gamma_{\min} \tag{6-2}$$

The term ζ could also be re-written as:

$$\zeta = \left(\frac{U_W t}{b}\right) = \left(\frac{U_W t}{b}\right)\left(\frac{\tau}{\tau}\right) = \left(\frac{U_W \tau}{b}\right)\left(\frac{t}{\tau}\right) = \left(\frac{S_R}{b}\right)\left(\frac{t}{\tau}\right) = \beta\left(\frac{t}{\tau}\right), \beta = \frac{S_R}{b} \tag{6-3}$$

The transport equation for intermittency, γ, would have the following format:

$$\frac{\partial \gamma}{\partial t} + V.\nabla\gamma = P_t + P_c + D_\gamma - E_\gamma \tag{6-4}$$

The P_t and P_c, which are transient and convective terms. P_t is:

$$\begin{aligned} P_t &= \frac{\partial \gamma}{\partial t} = \frac{\partial}{\partial t}\left(\left(\gamma_{\max} - \gamma_{\min}\right) e^{-\zeta^2} + \gamma_{\min}\right) = \left(\gamma_{\max} - \gamma_{\min}\right) \frac{\partial}{\partial t} e^{-\zeta^2} \\ &= \left(\gamma_{\max} - \gamma_{\min}\right)\left(-2\zeta \frac{\partial \zeta}{\partial t}\right) e^{-\zeta^2} = \left(\gamma_{\max} - \gamma_{\min}\right)\left(-2\beta\left(\frac{t}{\tau}\right)\left(\frac{\beta}{\tau}\right)\right) e^{-\zeta^2} \\ &= -2\left(\frac{\beta}{\tau}\right)^2 t e^{-\zeta^2} \left(\gamma_{\max} - \gamma_{\min}\right) \\ \rightarrow P_t &= -2\left(\frac{\beta}{\tau}\right)^2 t \left(\gamma_{\max} - \gamma_{\min}\right) e^{-\zeta^2} \end{aligned} \tag{6-5}$$

Equation (6-5) could be re-written as the following by incorporating equation (6-2).

$$P_t = -2\left(\frac{\beta}{\tau}\right)^2 t\left(\gamma - \gamma_{\min}\right) \tag{6-6}$$

The spatial source term could be obtained and formulated as the following:

$$P_c = V_1 . \frac{\partial \gamma}{\partial x_1} + V_2 . \frac{\partial \gamma}{\partial x_2} + V_3 . \frac{\partial \gamma}{\partial x_3} \tag{6-7}$$

Alternatively, transport equations could be written for γ_{min} and γ_{max}, without having to include the transient term. In that case, only the convection term would appear in the

left hand-side of the transport equation. Later, the intermittency would be established at each location using equation (6-2). The alternate method was used as well in this study.

The intermittency measurements were performed in the stream-wise direction while the spatial term has to be written in the Cartesian coordinate system to more easily and appropriately program it into the solver. The curvilinear coordinate system is shown in the following figure.

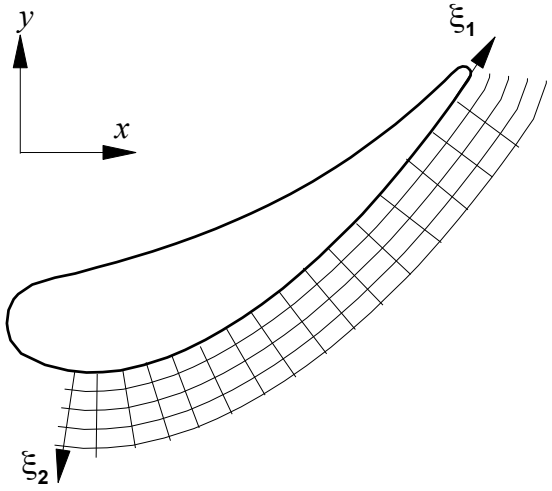

Figure 6-2 Curvilinear coordinate system for high-pressure turbine blade. Stream-wise (ξ_1) and blade-normal (ξ_2) direction

The source term of the intermittency transport equation is fully defined if γ_{min} and γ_{max} are defined. Minimum intermittency is defined according to Ref [1]:

$$\gamma_{\min} = c_2 \left(1.0 - e^{-\left(\frac{\mathrm{Re}_x - \mathrm{Re}_{x,s}}{\mathrm{Re}_{x,s} - \mathrm{Re}_{x,e}} \right)^2} \right) \qquad \textbf{(6-8)}$$

Instead of equation (2-10), maximum intermittency is specified in the following format:

$$\gamma_{\max} = 0.8 - \gamma_{\min} \tag{6-9}$$

Since $\gamma=\gamma(\xi_1,\xi_2)$, the derivative terms could be written in the following form using the chain rule:

$$\frac{\partial \gamma}{\partial x_i} = \frac{\partial \gamma}{\partial \xi_j}\frac{\partial \xi_j}{\partial x_i} = \frac{\partial \gamma}{\partial \xi_1}\frac{\partial \xi_1}{\partial x_i} + \frac{\partial \gamma}{\partial \xi_2}\frac{\partial \xi_2}{\partial x_i} \tag{6-10}$$

And the derivatives with respect to stream-wise coordinate (ξ_1) that appear in equation (6-10), could be obtained using equation (6-2):

$$\begin{aligned}\frac{\partial \gamma}{\partial \xi_1} &= \frac{\partial}{\partial \xi_1}\left(\gamma_{\max} - \gamma_{\min}\right)e^{-\zeta^2} + \gamma_{\min} \\ &= \left(\frac{\partial \gamma_{\max}}{\partial \xi_1} - \frac{\partial \gamma_{\min}}{\partial \xi_1}\right)e^{-\beta^2\left(\frac{t}{\tau}\right)^2} + \frac{\partial \gamma_{\min}}{\partial \xi_1}\end{aligned} \tag{6-11}$$

And finally, the derivative of γ_{min} and γ_{max} with respect to streamwise coordinate.

$$\begin{aligned}\frac{\partial \gamma_{\max}}{\partial \xi_1} &= C_1\left(\xi - \xi_s\right)e^{-\left(\frac{\xi-\xi_s}{\xi_e-\xi_s}\right)^2} \\ \frac{\partial \gamma_{\min}}{\partial \xi_1} &= C_2\left(\xi - \xi_s\right)e^{-\left(\frac{\xi-\xi_s}{\xi_e-\xi_s}\right)^2}\end{aligned} \tag{6-12}$$

γ in the stream-wise direction varies according to Figure 6-1 and equation (6-2). Intermittency measurements in the blade-normal direction are not performed, and for that reason, we have assumed that intermittency is changing in ξ_2 direction in the same way that it would change in a curved plate test case. Figure 2-4 that was obtained by performing intermittency measurement on the concave side of a curved plate at different distances by Chakka and Schobeiri [134] is used for this purpose.

The intermittency distributions in Figure 2-4, bears a striking resemblance to Gaussian distribution, for that reason, the following distribution of intermittency has been used to derive the derivatives in ξ_2 direction.

$$\gamma = \frac{1}{\sigma\sqrt{2\pi}} e^{-\frac{(S-\mu)^2}{2\sigma^2}} \tag{6-13}$$

$$\frac{\partial \gamma}{\partial \xi_2} = \frac{\partial}{\partial \xi_2}\gamma\left(\sigma(\xi_2), \mu(\xi_2)\right) = \frac{\partial \gamma}{\partial \sigma}\frac{\partial \sigma}{\partial \xi_2} + \frac{\partial \gamma}{\partial \mu}\frac{\partial \mu}{\partial \xi_2} \tag{6-14}$$

Equation (6-14) is used in equation (6-10) only once the relationship between σ and μ with ξ_2 is established. Finding the best Gaussian fit for the measurements shown in Figure 2-4 would provide us with such information. By doing so, the following figure is obtained and presented here. It shows how coefficients σ and μ would vary with ξ_2.

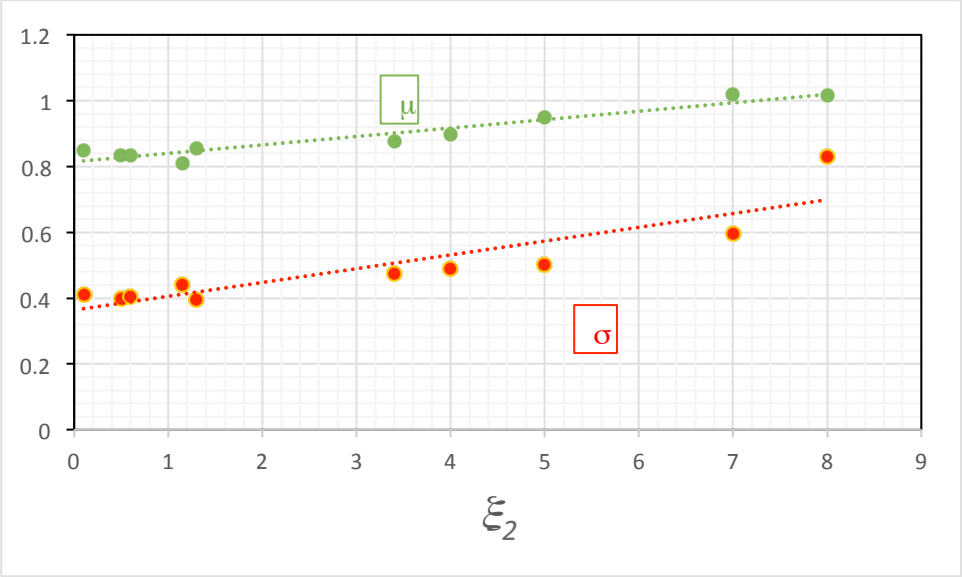

Figure 6-3 variations of σ and μ with ξ_2. Obtained through finding the best fit for the intermittency distribution

By having this information, the convective term of the intermittency transport equation, P_c, could be derived in the following form:

$$V_i \frac{\partial \gamma}{\partial x_i} = V_i \left(\frac{\partial \gamma}{\partial \xi_j} \frac{\partial \xi_j}{\partial x_i} \right) = V_i \left(\frac{\partial \gamma}{\partial \xi_1} \frac{\partial \xi_1}{\partial x_i} + \frac{\partial \gamma}{\partial \xi_2} \frac{\partial \xi_2}{\partial x_i} \right) =$$

$$V_i \left(\frac{\partial \gamma}{\partial \xi_1} \frac{\partial \xi_1}{\partial x_i} + \left(\frac{\partial \gamma}{\partial \sigma} \frac{\partial \sigma}{\partial \xi_2} + \frac{\partial \gamma}{\partial \mu} \frac{\partial \mu}{\partial \xi_2} \right) \frac{\partial \xi_2}{\partial x_i} \right) = V_i \left(\left(\left(\frac{\partial \gamma_{\max}}{\partial \xi_1} - \frac{\partial \gamma_{\min}}{\partial \xi_1} \right) e^{-\beta^2 \left(\frac{t}{\tau} \right)^2} + \frac{\partial \gamma_{\min}}{\partial \xi_1} \right) \frac{\partial \xi_1}{\partial x_i} + \ldots \right. \quad \textbf{(6-15)}$$

$$\left. \ldots + \left(\frac{-1}{\sigma^2 \sqrt{2\pi}} e^{\frac{-(\xi_1 - \mu)^2}{2\sigma^2}} \left(-1 + \frac{(\xi_1 - \mu)^2}{\sigma^2} \right) \frac{\partial \sigma}{\partial \xi_2} + \frac{(\xi_1 - \mu)}{\sigma^3 \sqrt{2\pi}} e^{\frac{-(\xi_1 - \mu)^2}{2\sigma^2}} \frac{\partial \mu}{\partial \xi_2} \right) \frac{\partial \xi_2}{\partial x_i} \right)$$

The transport equation for intermittency in the curvilinear coordinate system would be:

$$\frac{D\gamma}{Dt} = \frac{\partial \gamma}{\partial t} + V . \nabla \gamma = -2 \left(\frac{\beta}{\tau} \right)^2 t \left(\gamma - \gamma_{\min} \right) +$$

$$V_i \left(\left(\left(\frac{\partial \gamma_{\max}}{\partial \xi_1} - \frac{\partial \gamma_{\min}}{\partial \xi_1} \right) e^{-\beta^2 \left(\frac{t}{\tau} \right)^2} + \frac{\partial \gamma_{\min}}{\partial \xi_1} \right) \frac{\partial \xi_1}{\partial x_i} + \ldots \right. \quad \textbf{(6-16)}$$

$$\left. \ldots + \left(\frac{(\xi_1 - \mu)}{\sigma^3 \sqrt{2\pi}} e^{\frac{-(\xi_1 - \mu)^2}{2\sigma^2}} \frac{\partial \sigma}{\partial \xi_2} + \frac{(\xi_1 - \mu)}{\sigma^3 \sqrt{2\pi}} e^{\frac{-(\xi_1 - \mu)^2}{2\sigma^2}} \frac{\partial \mu}{\partial \xi_2} \right) \frac{\partial \xi_2}{\partial x_i} \right)$$

$$\ldots + D + E$$

For dissipation and diffusion terms, the correlations suggested by Steelant and Dick [45] is used:

$$E = \frac{V}{V_\infty} \frac{\partial V}{\partial n} \frac{\partial \gamma}{\partial n} \quad \textbf{(6-17)}$$

$$D = \frac{\partial}{\partial x_i} \left[\mu_\tau \frac{\partial \gamma}{\partial x_i} \right] \quad \textbf{(6-18)}$$

6.1.2 Implementation of γ Transport Equation in Fluent

The new intermittency transport equation is integrated into SST-$k\omega$ model. This equation is solved along with other transport equations for remaining turbulence

parameters (k and ω). The obtained intermittency, γ, is then used to correct the production of turbulence kinetic energy, k.

To introduce the new transport equation for intermittency in Fluent solver, a completely new turbulence model was written using User Defined Function (UDF). Initially transport equations f1or k and ω were written, tested and compared to the built-in transport equations for k and ω in SST model of Fluent.

$$\frac{\partial k}{\partial t} + U.\nabla k = P_k - \beta^* k\omega + \nabla\left[\left(\nu + \sigma_k \nu_T\right)\nabla k\right] \quad \textbf{(6-19)}$$

$$\frac{\partial \omega}{\partial t} + U.\nabla \omega = \alpha S^2 - \beta\omega^2 + \nabla\left[\left(\nu + \sigma_\omega \nu_T\right)\nabla\omega\right] + 2\left(1 - F_1\right)\sigma_{\omega 2}\frac{1}{\omega}\nabla k.\nabla\omega \quad \textbf{(6-20)}$$

For each turbulence parameter, k and ω, a scalar was defined, and corresponding source, diffusion, and dissipation terms are written. Once a reasonable agreement between the product of the two different sets of transport equations was obtained, the third transport equation for intermittency was added, and the production term of k transport equation was corrected in the following manner.

$$P_k = \gamma \times \min\left(\tau_{ij}\frac{\partial U_i}{\partial x_j}, 10\beta^* k\omega\right) \quad \textbf{(6-21)}$$

The UDF codes are included in the Appendix.

6.1.2.1 Near-wall Physics

One of the most challenging regions in common wall-bounded flows is the near-wall regions. The main complexities that presence of wall could impose on the problem could be categorized in the following two categories [135].

- Turbulence anisotropicity due to damping the wall-normal component.

- Increase in the production of turbulence kinetic energy through the shearing mechanism in the flow.

Presence of wall causes boundary layer, in which velocity changes from zero (no-slip boundary condition on the surface) to the free-stream velocity at the edge of the boundary layer. This fact results in a rather large gradients in flow quantities. The gradients are normally largest in the vicinity of the wall. Flow quantities such as friction factor are a function of velocity gradient inside the boundary layer. Similarly heat transfer coefficient is a function of temperature gradient (because of the thermal boundary layer that exists in near-wall zones). For that reason, accurate resolution of the near-wall effect is of paramount importance. Near-wall areas could be divided into three different areas according to Tennekes and Lumley [136].

- Viscose sub-layer ($y^+<5$)
- Buffer region ($5<y^+<30$)
- Inertial sub-layer ($30<y^+$)

Viscous effects are small in viscose sub-layer, and for that reason, the turbulence could be assumed negligible. Inside the viscose sub-layer, there exists a linear relationship between velocity/temperature and y^+. In buffer layer, however, both turbulent and viscose effects are considerable. The maximum turbulent production occurs inside the buffer layer at approximately $y^+=12$. Turbulence modeling in this region becomes a little challenging since there is a large variation in different turbulence source terms. Inside the inertial sub-layer, where $y^+>30$, there is a logarithmic relationship between velocity/temperature and y^+ according to Wilcox [116].

$$U^+ = \frac{1}{\kappa} \ln y^+ + B \qquad \text{(6-22)}$$

$$T^+ = \frac{1}{\kappa_T} \ln y^+ + B_T \qquad \text{(6-23)}$$

Inertial sub-layer is also referred to as logarithmic region because of the above relationships.

The standard method, when it comes to resolving the flow in near-wall regions, is to apply very fine mesh close to the wall. This method, that has been introduced earlier in this manuscript, is known as integration method or Low-Reynolds number (LRN) method. In this approach, a rather large number of nodes are required, and from computational stand-point, it could potentially require large computational power. Hence the alternative is proposed. In the alternate approach, which is known as High-Reynolds number (HRN) models, a function is used to bridge the near-wall regions and thereby the computational costs are significantly reduced. The added function is called wall function. The wall function is supposed to produce small to no deterioration to the results, but according to the personal experience of the author, when the flow is highly unsteady and transitional, they are not be expected to produce an accurate prediction of flow quantities inside the boundary layer.

In the current study, the former method (LRN) is used. The grid is composed of very fine elements in near-wall regions to successfully resolve the laminar sub-layer. Using this approach, more accurate results are expected and also producing and implementing wall functions are avoided.

6.1.3 Low-Pressure Turbine Blade Test Case

The Low-pressure turbine blade was subject of many experimental studies done by Schobeiri and co-workers [15, 30, 31, 137]. The intermittency transport equation, derived for the unsteady case in section 6.1.1 is applied to low pressure turbine simulation, with one difference: the minimum and maximum intermittency in low-pressure turbine case have the following distribution:

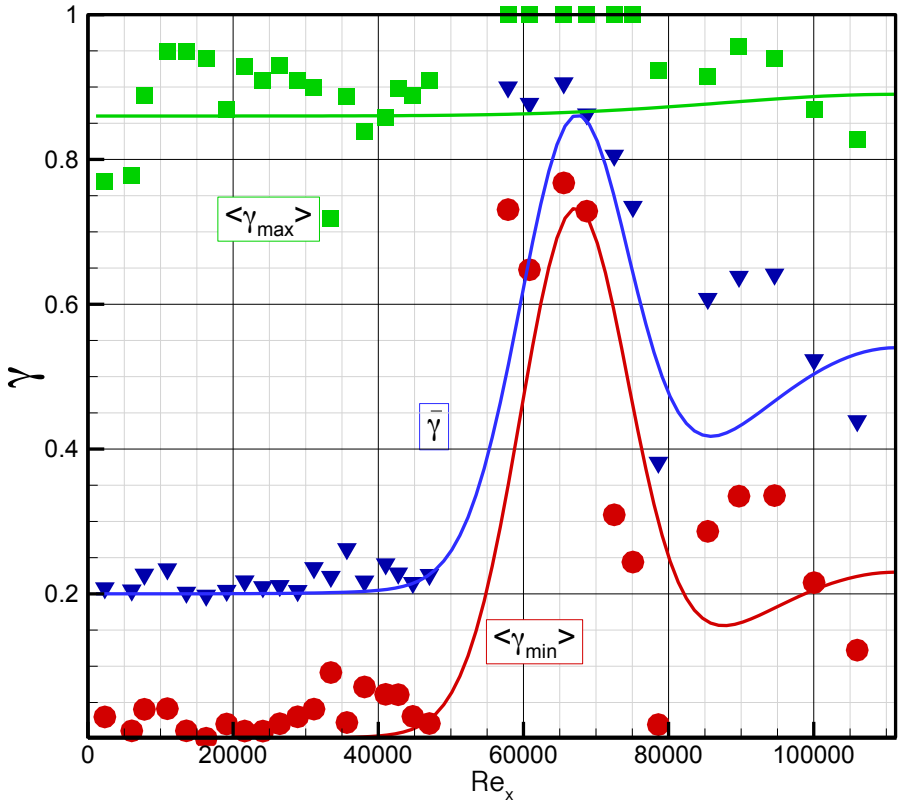

Figure 6-4 Minimum, maximum and time-averaged intermittency distribution for separated flow over a Low-pressure turbine blade as a function of axial Reynolds number at (Ω=1.59) [16]

The following picture shows the 2-D computational domain for the low-pressure turbine blade case. The boundary conditions prescribed for the top and bottom surfaces are periodic boundary condition so that it resembles the periodicity in the cascade.

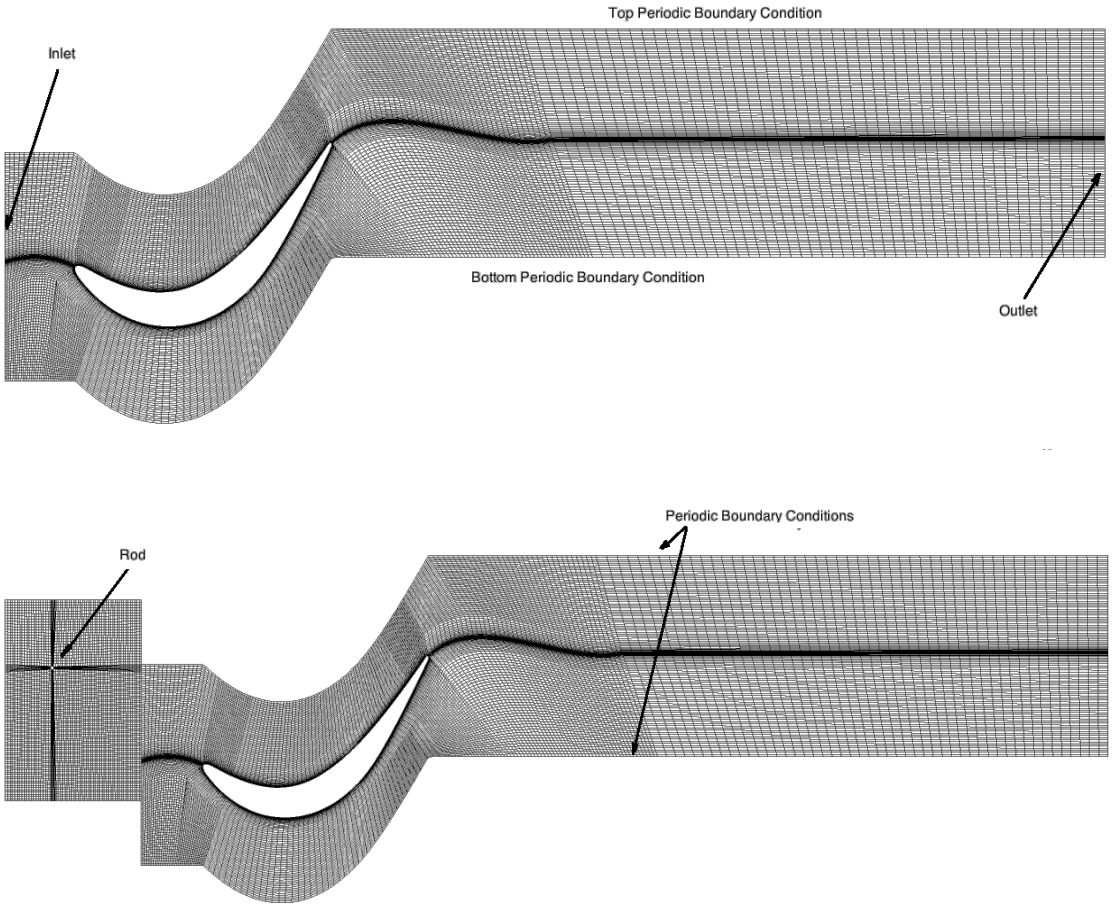

Figure 6-5 Computational grid used for numerical simulations of LPT test case, Steady case (top) and Unsteady simulation (bottom)

6.1.4 High-Pressure Turbine Blade Test Case

The high-pressure turbine blade cascade was the subject of measurements in Schobeiri and Chakka [2], for which the intermittency transport equation and the UDF code were derived and written respectively. The geometry of this HPT blade is shown in Figure 6-6.

This computational domain is composed of 340,000 number of elements, and periodic boundary conditions are used for identical top and bottom surfaces. In the formulations of the intermittency transport equations, which was implemented in the code, the transition start and end points were manually set equal to the measurements of Ref[2].

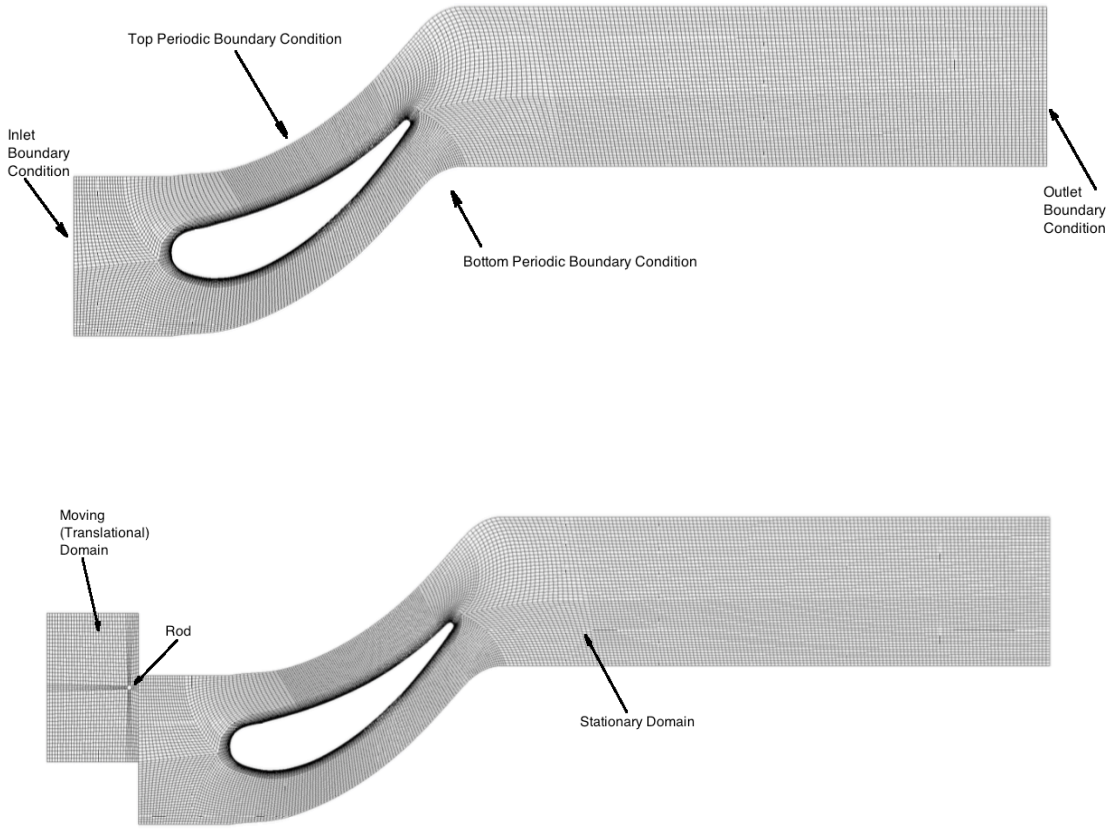

Figure 6-6 Computational grid used for numerical simulations for HPT test case, Steady case (top) and Unsteady simulation (bottom)

6.2 Experimental Validation

A transition model according to the formulation in the previous chapters and based on Chakka and Schobeiri [1] was constructed via User Defined Function and employed into the commercial solver ANSYS Fluent. The transition start and end points are based

on curved plate experiments, Ref[1]. The obtained results from the implementation of the new model into the solver were compared to the Menter's γ-Reθ model, [43, 44].

6.2.1 Low-Pressure Turbine Test Case

The following contains the results obtained from implementing the new transport equation for intermittency in ANSYS Fluent for low-pressure turbine blade test case.

6.2.1.1 Surface Pressure Distribution

In the experimental measurements, the static pressure was read using static pressure taps instrumented in the blade and pneumatic pressure transducer. As seen in the plotted time-averaged surface pressure distribution, there is a strong negative Pressure gradient until the minimum pressure point is reached. At this location, the minimum pressure coefficient is -3.56 at approximately $S/S_0=0.49$. Prior to minimum pressure point, the SST model and the new model perform well and the results are in complete agreement with measurements. Downstream from this location, the fluid particles decelerate and

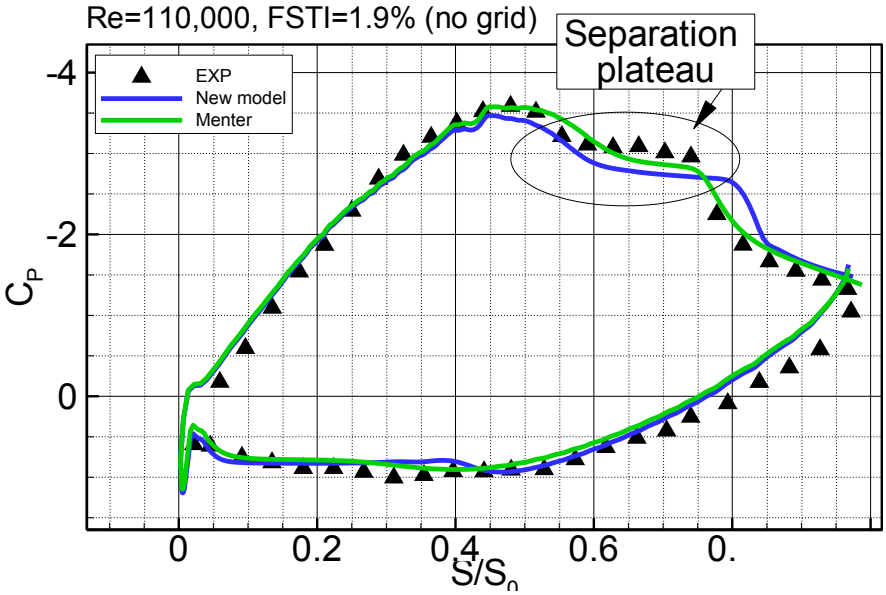

Figure 6-7 Pressure coefficient distribution around the low-pressure turbine blade [51]

deviations between simulations and measurements become more obvious. The deceleration continues until location $S/S_0=0.55$ is reached. This point signifies the beginning of the constant pressure plateau, which is indicative of flow separation. During the length of flow separation, the surface pressure remains constant. Both models are relatively successful in-terms of capturing the constant pressure plateau. This plateau is larger in the case of the new model compared to the SST turbulence model. This claim is substantiated after plotting the velocity contour plots on suctions surface (see Figure 6-9). Presence of wakes shows a vivid reduction in length of the separation bubble. This is seen by observing a shorter separation plateau. The same trend is also seen in both transitional models. In other words the impinging wakes have the effect of reduction in size of separation region.

6.2.1.2 Time-Averaged Velocity and Velocity Fluctuation

In the upstream region of the separation bubble the flow is fully attached. At the first location ($S/S_0=0.49$) there is negligible difference between the different velocity profiles. In the last three locations, S/S_0=0.73, 0.77 and 0.85, as displayed, despite the very thin boundary layer, even in the separation zone, transitional-*SST* model was successful to capture the back-flow zone although the predicted separation is very small. The introduced model is also relatively successful in terms of predicting the separation bubble with the advantage of having a more pronounced boundary layer. In other words boundary layer thickness is considerably improved and is more realistic in the new model.

Also judging by the velocity and velocity fluctuation profiles, it appears that the boundary layer thickness in the new model is more sensitive to unsteady wake frequency

as thickness has considerably increased whereas it has maintained almost the same thickness in the Langtry-Menter model in steady and unsteady flow conditions.

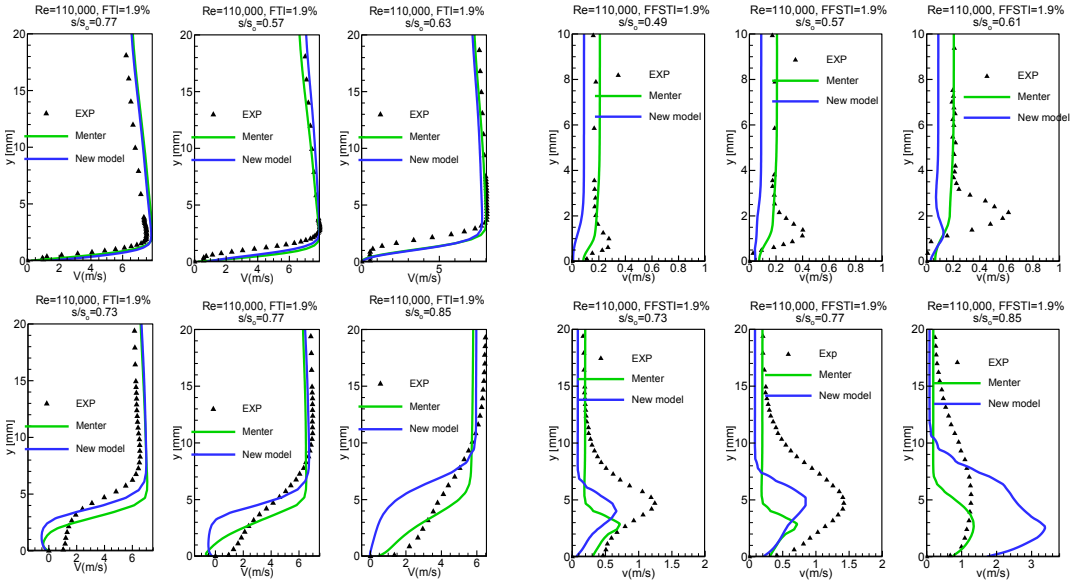

Figure 6-8 Velocity and velocity fluctuation profiles at 6 different stream-wise locations on the suction side of LPT blade at Ω=1.59

6.2.1.3 Flow Separation

Figure 6-9 shows the velocity magnitude contour plot of a portion of suction surface of the low-pressure turbine blade. Both models (SST and the new model) fail to locate the separation at a more downstream location than reality. This fact, as mentioned earlier, had also affected the pressure distribution around the blade.

The separation region predicted by the new model is considerably larger in both streamwise and cross-stream directions, than the SST model and of-course the measurements. This will certainly have effects on heat transfer coefficient distribution as this region is inherently weak on energy and is incapable of effectively transferring mass and energy, which will be discussed in the following section.

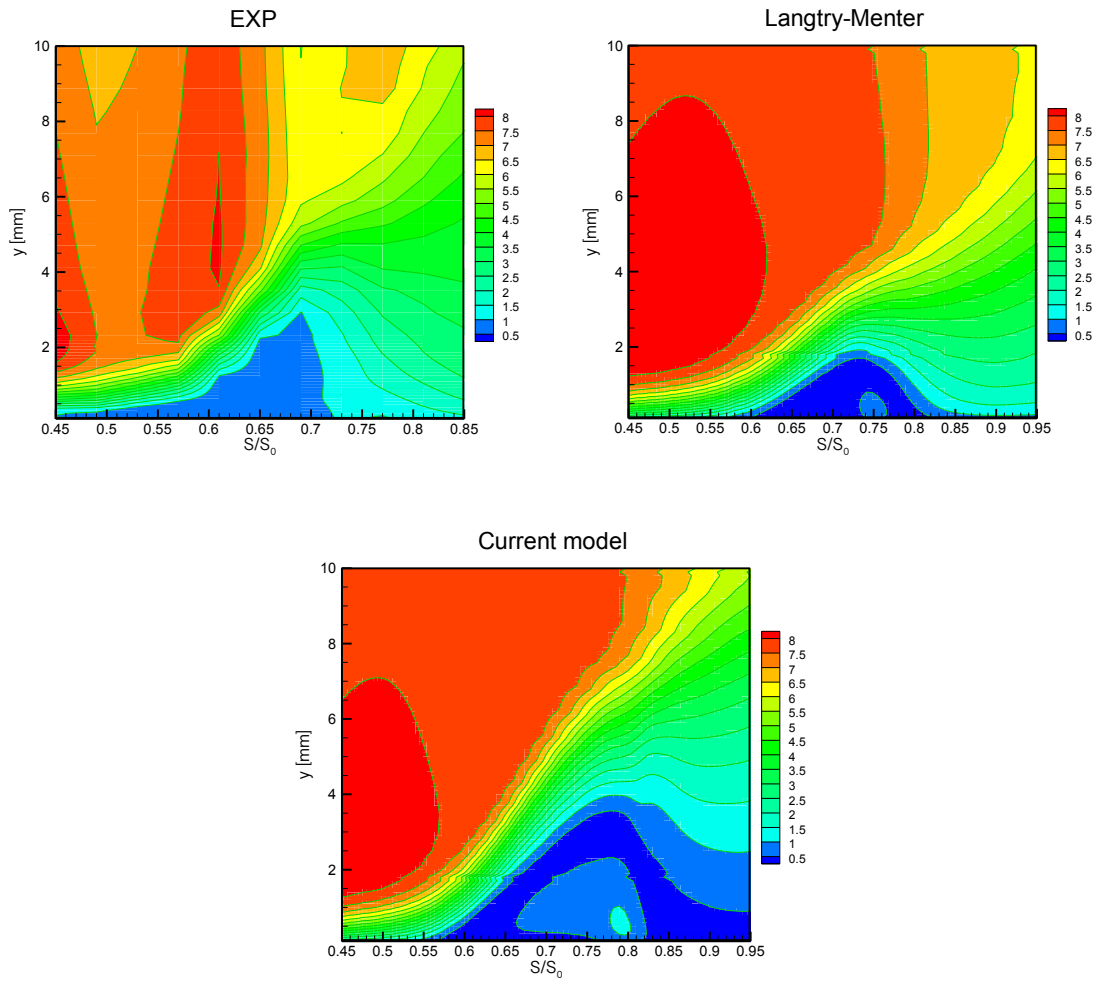

Figure 6-9 Velocity contour plots showing separation region, obtained from experimentation, SST model and the new model [51]

6.2.1.4 Heat-Transfer Coefficient

The distribution of heat transfer coefficient on the suction side of the blade is shown in the following figure. During the laminar region, the predicted heat transfer coefficient along the suction side using both models closely follow the experimental measurements. The drop of heat transfer coefficient continues until separation bubble is met. Separation bubble leading edge, signifies the point where deviations begin. Inside the separation zone the drop continues until the turbulence activity inside the bubble increases once again and as a result, the heat transfer coefficient rises and experiences a

local maximum at the location of re-attachment. The new model and the transitional-SST both fail to correctly locate the onset of separation bubble. In both cases, the bubble is delayed and consequently the HTC profile is affected.

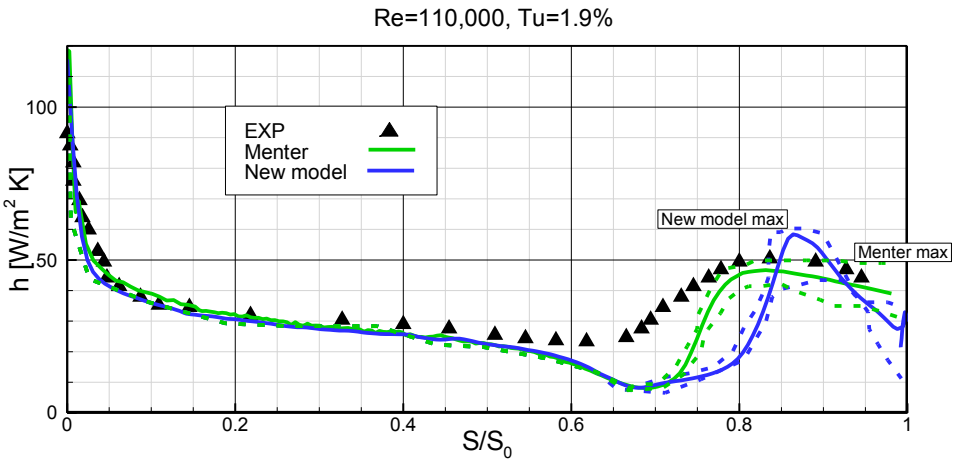

Figure 6-10 Heat transfer coefficient distribution along the low-pressure turbine blade suction surface obtained through experimental measurements, SST and the new model

6.2.2 High-Pressure Turbine Test Case

6.2.2.1 Surface Pressure Distribution

Static pressure distribution around the blade was obtained using a blade instrumented with static pressure taps at the mid-section of the blade [138]. Since the pressure taps are connected to pneumatic pressure transducers, the pressure readings would be inherently time-averaged due to internal damping effects. Figure 6-11 shows the distribution of pressure coefficient around the blade. In this picture, the symbols represent the experimental measurements, and the solid and dashed curves are the pressure distributions obtained from numerical simulations using the new model as well as the model proposed in Refs [43, 44, 46, 47], also known as $\gamma-Re_{\theta}$.

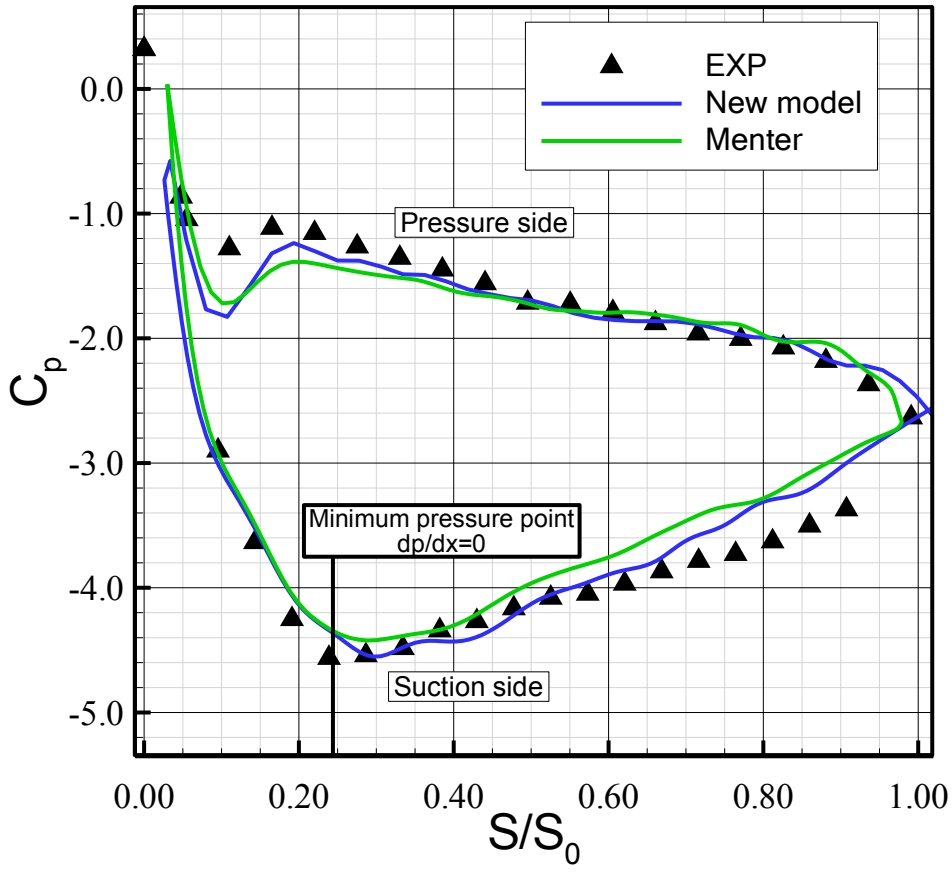

Figure 6-11 Pressure coefficient distribution around the blade obtained from measurements (symbols) and calculated using two transitional methods

The pressure distributions around the blade are almost identical for both numerical cases and are in complete agreement with the pressure readings from the experiment. Slight differences are observed in the leading edge region. This deviation could be a result of the difference in production of turbulent kinetic energy in the stagnation zone. The over/under-production of turbulent kinetic energy could cause deviations in flow losses that could potentially impact the development of boundary layer and pressure distribution. In more downstream regions, where there is a reasonable distance from stagnation point, the disagreement between the results become less apparent.

6.2.2.2 Time-Averaged Velocity and Velocity Fluctuation

Pressure distribution could give us some rough idea about the aerodynamics of the blade. However exact boundary layer measurements are required to understand and discuss the underlying physics of what is happening inside the boundary layer. After performing exact boundary layer measurements, the readings were ensemble averaged and then the boundary layer coordinates were transformed into blade-normal as explained before in Ref [51].

Figure 6-12 shows the time-averaged velocity and velocity fluctuations for five different locations obtained through measurements and also numerical modeling. It is apparent in this picture that the differences between velocity profiles in the laminar flow condition, $S/S_0=0.34$, is negligible (According to Ref [2], this region exhibits laminar flow regime). In more downstream zones, the deviations and differences become more apparent. Also, judging by velocity profiles, the transitional SST model predicts a thicker boundary layer initially up to the location where the average intermittency has risen and maintains a constant value ($S/S_0>0.7$). At these locations, both numerical models show similar behaviors and predict similar thickness for boundary layer.

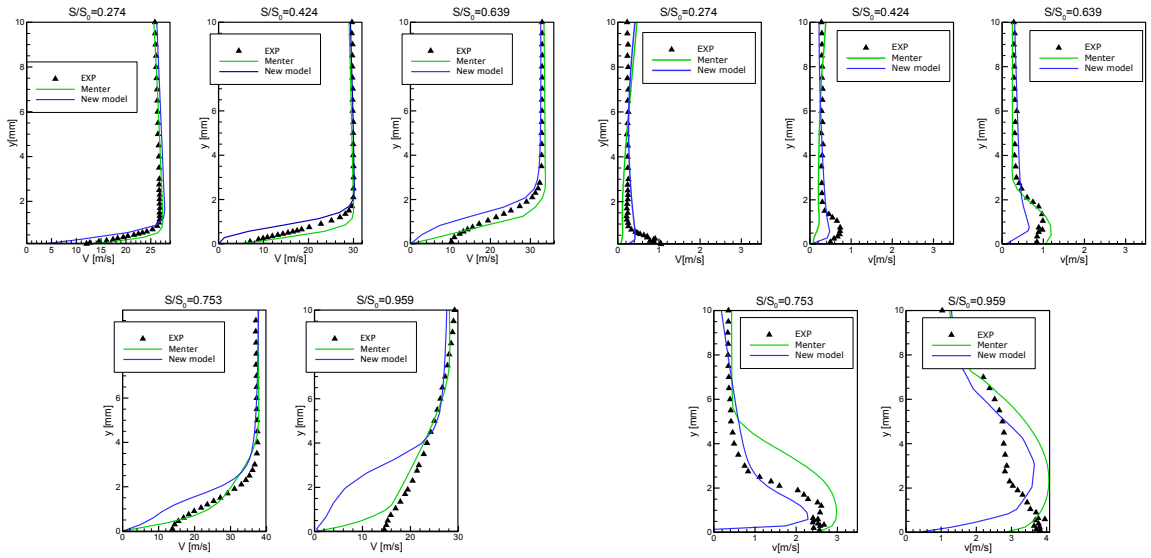

Figure 6-12 Time-averaged velocity and velocity fluctuation profiles obtained through experimentations and numerical simulations using the SST method and the new model

Velocity fluctuations are of importance since they define Reynolds stress tensor elements. Also, the fluctuations are responsible for the transfer of energy into the boundary layer. Using single-wire custom designed hot-wire sensor, the stream-wise velocity, and velocity fluctuations could be obtained. Prandtl hypothesis could later be used to obtain the lateral velocity fluctuations[130]. According to this hypothesis, which is confirmed by many researchers[139], the lateral fluctuation is proportional to streamwise fluctuations.

Inside the laminar boundary layer (S/S_0=0.343), the experiments show up to almost 1m/s fluctuations while the magnitude of fluctuations predicted by the modeling is much higher. At this location, the difference between the predictions of the two models is considerable. As the flow progresses in the streamwise direction and passes the minimum pressure point, the difference becomes more apparent. Menter model, which initially

under-predicts fluctuations in laminar zone, in more downstream locations, over-predicts the level of fluctuation fluctuations.

6.2.2.3 Heat Transfer

Heat transfer and aerodynamics are closely related subjects. A negligible computational error in aerodynamics flow quantities could propagate to heat transfer calculations and produce significant disagreements and deviations [129]. Lateral and axial velocity fluctuations are responsible for the transfer of mass, momentum, and energy into the boundary layer. There is a direct relationship between the amount of energy that is transferred to the blade and the level of fluctuations. As seen in previous sections, the commercial solvers are capable of calculating correct pressure distributions, and to some extent, velocity profiles but they lack the capability of correctly predicting the magnitude of velocity fluctuations. For that reason, to obtain a reliable solution for energy transport equation, correct modeling of turbulent aerodynamics parameters is required.

In terms of heat transfer coefficient, there is a large difference observed between the two sets of computational results. As shown in Figure 6-13, the heat transfer coefficient calculated by two models show completely different trend. On the suction surface of the blade, both models are successful in capturing the trend obtained from measurements, especially in laminar zone, but there are some differences, and it is tried to give a detailed investigation in the following.

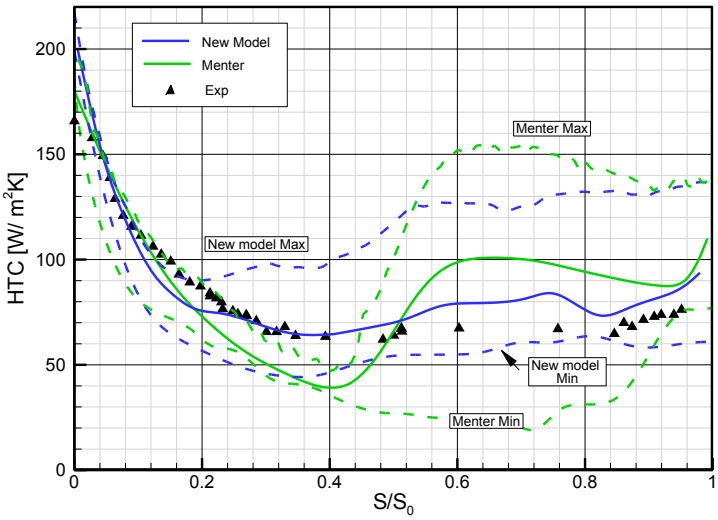

Figure 6-13 Heat transfer coefficient as a function of axial Reynolds number

The performance of the new model is significantly better, even in the laminar region. This improvement could very well be explained considering the velocity fluctuations shown in Figure 6-12. Since the level of differences between experimental and numerical data sets, in-terms of fluctuations, is relatively smaller for the case of the new model, the heat transfer coefficient is also in better agreement with measurements. In the regions farther downstream from the leading edge, especially when the minimum pressure point has passed and pressure gradient changes sign, completely different behavior is observed in the results obtained from both turbulence models. In the transitional-SST model, due to the sudden transition of flow from laminar to turbulent, heat transfer coefficient rises almost immediately. While in the new model, a more gradual increase in-terms of heat transfer coefficient is observed. Since the start and end transition Reynolds numbers could be manually controlled in the new model, superior performance was expected and is obtained. Menter model is highly sensitive to inlet flow

condition, namely turbulence intensity and although the inlet turbulence intensity is calibrated according to the measurements, it fails to place the transition onset correctly.

6.2.2.4 Intermittency

The high-pressure turbine test case was simulated using URANS, where the relative intermittency was used to determine intermittency value at different times and locations. When the wake with its highly vortical core impinges on the blade surface, the relative intermittency, Γ, was set to one and once the wake has passed and the same location is exposed to calm region, the relative intermittency of zero was used.

Figure 6-14 shows the resultant intermittency at various locations at different times. These contour plots are obtained through experimental measurements, Menter model and implementing the new transitional model into the Fluent solver. In these contour plots, only the first three wakes are shown for a better comparison of the effects of impinging wakes on the transition process. According to the measurements, intermittency is equal to zero in the region outside the wakes. In Figure 6-14(a), wake region is identified as a thin region with intermittency value near one. In the same figure, it is seen that the boundary layer periodically switches from laminar to turbulent and the fact that natural transition is affected by the periodic passing of the wakes. The wakes are initially very thin and do not interact, until almost the end of the blade in measurements. Transitional-SST predicts that the wakes interact at approximately S/S_0=0.9. Beyond this point, there is no indication of the calm region. In case of the new model, wakes do not interact until the location S/S0=0.8 is met. They maintain a very distinct profile before this point. Downstream form this point, the wakes interact, and intermittency maintains an almost constant value. Figure 6-14(c) shows a rather sudden occurrence of turbulent spots at particular times due

to rods. In the new model, high intermittency is carried downstream from the rods, and maximum intermittency drops almost consistently.

Using γ-Re_θ model, the calculations show that the maximum intermittency rapidly decreases to almost minimum intermittency before it starts to rise again at S/S_0=0.62. Prior to this location the effect of calm region prevails and suppresses the intermittency growth. Beyond this point, bypass transition trips the boundary layer to turbulent and maximum intermittency rises.

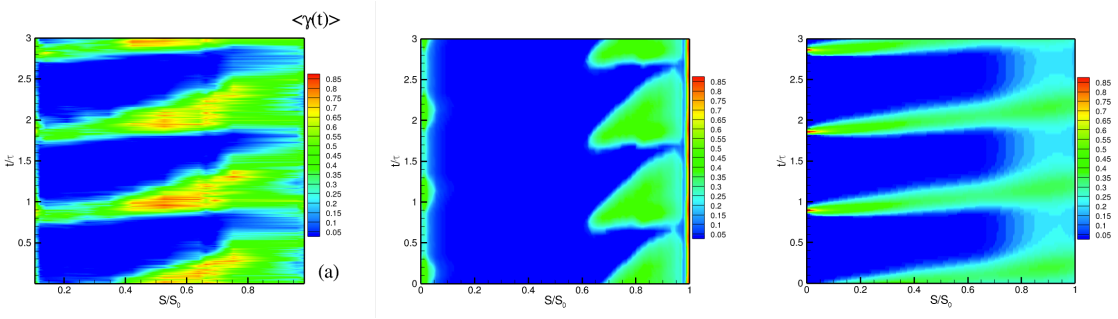

Figure 6-14 Unsteady intermittency at Ω=1.51 obtained through measurements (Left), Menter model (middle) and implementing the new model into the Fluent solver (right)

Intermittency factor, γ, shows a transient pattern and the boundary layer state constantly switches between laminar and turbulent. For that reason, intermittency at each location on the suction surface of the blade varies between a minimum and a maximum value. The maximum intermittency corresponds to the moment when the wake with its highly vortical core has impinged on the surface and shortly after the impingement, once the same location is exposed to calm region, the intermittency rapidly drops to a minimum value. The fluctuation bounds of the intermittency factor could be better seen and observed in Figure 6-15.

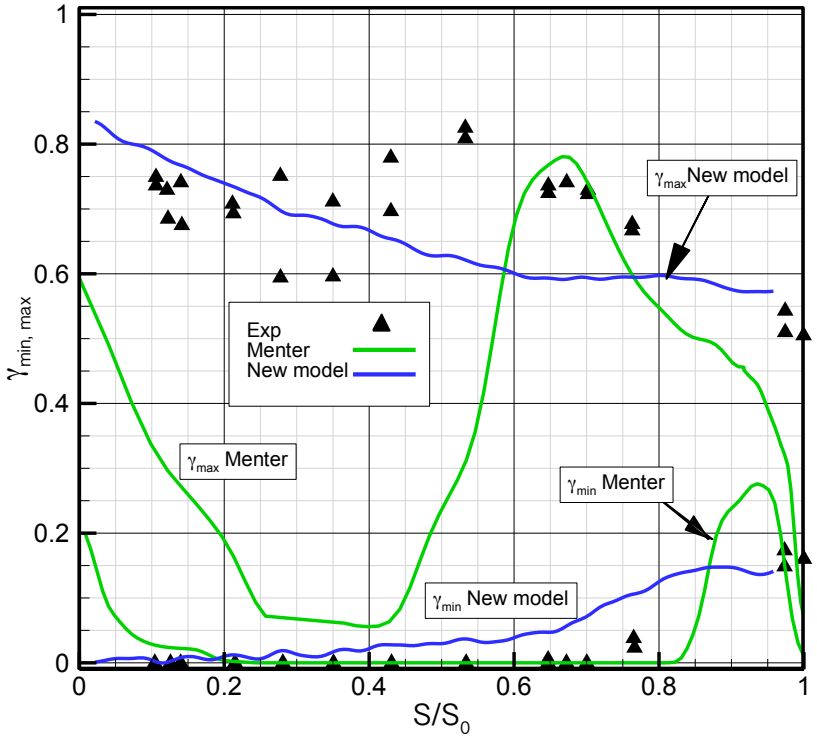

Figure 6-15 time-averaged intermittency as a function of axial Reynolds number

This figure is obtained for unsteady flow. The *min* and *max* subscripts respectively correspond to minimum and maximum values for intermittency. Minimum intermittency trend is very similar to the trend in intermittency factor that is observed in natural transition with one major difference. The minimum intermittency is affected by calming effect, and for that reason, there is a delay in the rise of intermittency and it never reaches one.

The maximum intermittency, on the other hand, is approximately equal to 0.8 at the beginning and remains almost constant. Until it gradually declines due to strong damping of wall shear stress forces. In Menter model, the maximum intermittency immediately rises, after a rapid drop, from a rather small value to almost 0.8. The initial value for intermittency is negligible in Menter model as seen in Figure 6-14 and Figure 6-15. This

indicates that the incoming wakes do not have as pronounced intermittency as seen in experiments and their kinetic energy has been damped long before they reach the leading edge of the blade. Yet, the energy is sufficient to trigger production terms in the boundary layer and increase the intermittency level to 0.8. Once the location S/S_0=0.3 is met, the same damping effect that had cause experimental measurements to fall, have produced a decline here as well. Regarding the results obtained by implementing the new model, the decrease in the maximum intermittency is more consistently seen from the beginning. On the other hand, minimum intermittency closely follows the minimum intermittency of measurements.

6.3 Conclusion of Aero-part

In addition to that, deficiencies of commercial turbulence models were investigated, and in an effort to enhance the performance of RANS solvers in-terms of accuracy in prediction of flow quantities, a new transport equation for intermittency is derived and implemented in a RANS solver. Computational Fluid Dynamics has advanced incredibly in recent years, yet there is still an uncertainty associated with CFD predictions. This uncertainty is improved in this study by incorporating a physics-based transport equation for intermittency rather than a transport equation that simply attempts to fit a large number of experiments into its formulation.

1. CFD simulations of flow over the low-pressure turbine blade were performed using a commercial RANS solver and the Menter's turbulence model. The existing built-in transition model of RANS solvers is capable of predicting a separation bubble on the suction surface of the blade although it fails to correctly locate the onset and extent of the bubble. Also incorrect prediction of fluctuations

inside the domain has resulted in consistently lower HTC resulting in more than 200% error at some critical locations.

2. Incoming wakes normally add to level of turbulence inside the domain. But the effect of unsteady wakes and FSTI do not superimpose. The experimental measurements of LPT case show that increasing wake frequency has resulted in lower HTC distribution. This effect is best seen in the high turbulence intensity and is mainly due to the calming effect. The Menter's model fails to see the calming effect and for that reason, RANS solver could not consistently predict the reduction in HTC for high turbulence intensity case when unsteady wakes have not been added to the system.
3. Degree of accuracy of HTC strongly depends on the accuracy in prediction of aerodynamic flow quantities. A small deviation of aerodynamic calculations could produce substantial disagreement in heat transfer. Accurately predicting the fluctuation components is crucial for predicting the HTC. New intermittency model is based on universal intermittency function developed and proposed by Schobeiri and Chakka [2]. According to this model, there exists a Gaussian distribution between the intermittencies inside(γ_{max}) and outside of the wake region(γ_{min}). Since the new intermittency model is physics based, it predicts higher velocity fluctuations inside the laminar boundary layer than Menter model. This fact translates into higher heat transfer coefficient in this zone.
4. During the transitional zone in the Menter model, velocity fluctuations rise and higher fluctuations than the measurements are seen. Transition occurs over a very short distance. Consequently, the heat transfer coefficient rises and an over-

prediction is observed in the turbulent regime. In case of the new model, the trend of heat transfer coefficient is better predicted and the gap between the actual and calculated heat transfer coefficient using Menter model is reduced. The heat transfer coefficient decreases almost consistently from the leading edge and the jump due to flow transition is of smaller order of magnitude.

7 INVESTIGATION OF FILM-COOLING EFFECTIVENESS

7.1 Introduction And Literature Review

In pursuit of obtaining higher thermal efficiency for gas turbine engines, the designers have constantly kept increasing the turbine inlet temperature of the engines. This has caused tremendous thermal stress and finally damage to engine components. Continuous exposure to high temperature increases the possibility of thermal failure of turbine components [140].

Aerodynamics and design of a gas turbine engine are constantly being evolved to find a more novel and efficient design. One of the major parameters that play a crucial role in the thermal efficiency of a gas turbine engine is the turbine inlet temperature. There is a tendency regarding increasing the turbine inlet temperature, which is only achievable by the progression of turbine cooling technology. Increase in the turbine inlet temperature results in a reduction of specific fuel consumption and increase in overall performance of the engine. However, operation at very high temperature is limited by the melting point of the material. Also, very high temperatures could harm the blades and reduce the lifetime of the engine elements. Therefore to raise the thermal capability of the engine, cooling techniques become necessary and inevitable. Figure 7-1 shows the trend that turbine inlet temperature has taken over the course of about 60 years. As shown in this figure, turbine inlet temperature has almost doubled since 1950.

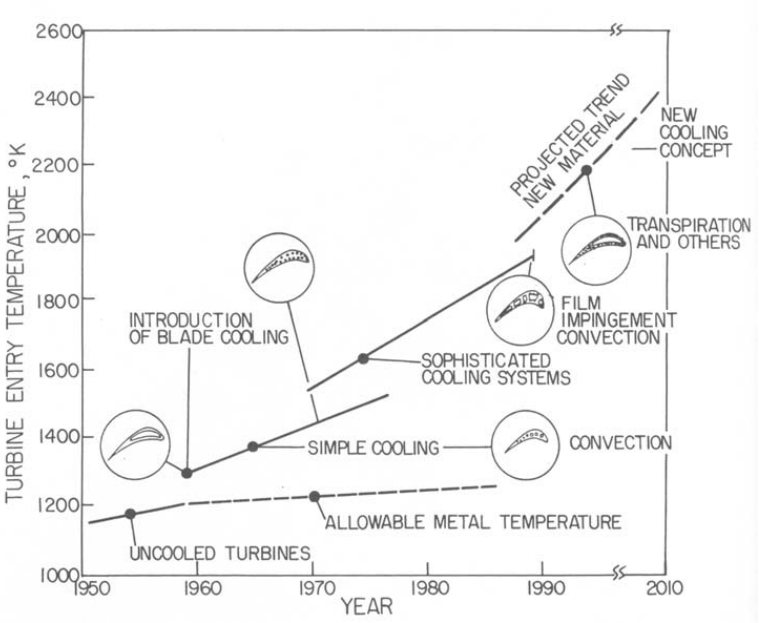

Figure 7-1 Increasing trend in turbine inlet temperature over the years. Image courtesy of Ref [141]

Internal and external cooling methods are employed to protect blades, and other engine elements from damages due to overheating. The cooling methods in which heat is removed through impingement and convection from internal surfaces of the blade fall under internal cooling techniques. On the other hand in external cooling methods, heat is removed from external surfaces of the blade through creating a thin film of coolant on top of the external surface of the blade through film cooling holes. A wide range of internal and external cooling arrangements have been designed, studied and applied in the past; however, the aim is to avoid high temperature gradient within the blade as well as maintaining the blade metal temperature reasonably low.

In the second part of this study, the film-cooling effectiveness of a highly-loaded turbine blade was investigated under steady and unsteady flow conditions. For that purpose, the surfaces of the blade were covered with pressure sensitive paint(PSP), and heat/mass transfer analogy was used to measure film-cooling effectiveness.

7.2 Turbine Film-Cooling

Goldstein, et al. [142] experimentally studied hole geometry, secondary fluid density and mainstream boundary layer thickness on film-cooling effectiveness. They instrumented an insulated test surface with 31 thermocouples to monitor the temperatures and finally determine the film-cooling effectiveness. They additionally used a fog of carbon dioxide and water vapor to visualize the flow.

Foster and Lampard [143] used mass transfer technique to research the effect of injection angle, upstream boundary layer, and holes spacing. They used a mixture of dense refrigerant vapor with air as coolant. They then drew gas samples through a katharometer to measure the concentrations and calculated the film-cooling ratio from the concentrations. They found that at low blowing ratio, small injection angles gives better cooling effectiveness while for high blowing ratio large injection angles are more preferable.

Schonung and Rodi [144] developed a two-dimensional boundary layer code to predict the film-cooling effectiveness by a row of holes. The three-dimensional nature of the flow, especially in the regions near the injection holes was modeled by dispersion terms. These terms describe the additional mixing by the laterally non-uniform flow. They predicted heat transfer and film-cooling effectiveness on a flat plate as well as gas turbine blade and compared their results with experimentally measured data. Haas, et al. [145] extended the two-dimensional boundary layer procedure of Schonung and Rodi [144] for calculating film-cooling to account for density difference between mainstream hot gas and the coolant. They researched the effect of coolant density difference between the coolant and mainstream air on film-cooling performance under different cooling hole

arrangements and blowing ratio. They reported that at constant blowing ratio, film-cooling effectiveness increases with the density ratio. Abhari and Epstein [146] performed heat transfer measurements on a film-cooled turbine blade in a turbine facility and concluded that time-averaged heat transfer could drop up to 60% on the suction surface of film-cooled blades compared to uncooled ones. Also showed that film cooling is less effective in high blowing ratios than low ones. Mehendale and co-workers [147, 148] measured film-cooling effectiveness and heat transfer coefficient on a low-pressure turbine blade in unsteady periodic wake-flow condition. They used thin-foil thermocouple method to measure the temperature and film-cooling effectiveness. In a subsequent study Teng, et al. [149] studied unsteady wake effects on film temperature and cooling effectiveness using liquid crystal method. They showed that unsteady wakes reduce film-cooling effectiveness. Also, film injection increases local heat transfer coefficient.

Abuaf, et al. [150] simultaneously determined the gas-side heat transfer coefficient and film-cooling effectiveness on the suction surface and in the leading edge showerhead region of a vane under both steady and unsteady conditions. They identified that film injection increases heat transfer coefficient levels on both suction and pressure sides. Ames [151, 152] performed extensive film-cooling research on a turbine blade and found for low turbulence intensities the heat transfer augmentation is generally higher, especially if the coolant is injected into laminar region compared to the turbulent region.

Heidmann, et al. [153] investigated the wake passing on showerhead film-cooling performance in an annular turbine cascade. They used thin-film gauges to determine local film effectiveness and Nusselt number. Their results indicated a drop in film-cooling

effectiveness with increasing wake-passing frequency. They also developed an equation to correlate the span-averaged film-effectiveness data.

Narzary, et al. [154] studied the effect of compound shaped holes on high-pressure turbine blades in a linear cascade under unsteady conditions. Bons [155] reviewed the mixed effects of surface roughness on gas turbine heat transfer and film cooling. He summarized that surface roughness at high blowing ratios can improve film-cooling effectiveness since it prevents jet lift-off from the surface. At low blowing ratios, it can, however, help jet lift-off through producing thicker boundary layer and lower near-wall velocities.

Gomes and Niehuis [156] experimented on film-cooling effectiveness in periodic and steady flow conditions on a high-pressure turbine blade in the presence of flow separation on the pressure side. They measured the surface temperature with thermochromatic liquid crystal. They reported that inside the separation region, cooling effectiveness is relatively poor due to jet lift-off and in the region of flow reattachment, film-effectiveness is quite well. Also, they observed better film-effectiveness under unsteady flow condition as they reduce jet lift-off due to stronger turbulent mixing inside the separation zone.

Heidman and co-workers [157, 158] measured surface and flow parameters on a large-scale model of an inclined row of film-cooling holes. They used IR thermography and near-wall thermocouples for measuring film-effectiveness, liquid crystal for heat transfer and hot wire anemometry for velocity and turbulence quantities. They determined the extent of mixing and captured jet lift-off from the surface. They also observed the

distinct kidney vortex that is often attributed to low effectiveness as the vortex pushes hot gas towards the blade surface.

Rallabandi, et al. [159] presented the results of their study on the compound effect of unsteady wakes and coolant density on turbine blade for a variety of blowing ratios.

8 RESEARCH OBJECTIVES

Film-cooling measurements in separated flow regions are not extensively studied in the literature. The present study[1] aims at investigating the effect of unsteady wakes on film cooling effectiveness of a low-pressure turbine (LPT) blade. The temperature at the low-pressure section hardly reaches critical temperature and cooling is not as necessary as it is in medium and high-pressure stages, yet the authors decided to perform measurements on this type of blade for the following reasons:

(1) The suction surface of a low-pressure turbine blade is subject to a strong negative pressure gradient followed by an equally strong positive pressure gradient. After reaching the minimum pressure point, the laminar boundary layer could potentially separate forming a separation bubble. Separation bubbles are not typical of LPT blades, and engine designers try to avoid suction surface separation as much as possible to minimize the loss. Yet, in considerable number of designs, separation bubbles become unavoidable, especially in off-design conditions. As the comprehensive boundary layer measurements reported in Ref [31, 137] show, the onset, the size and the location of this bubble change whenever wakes impinge on it. While the aerodynamics investigations in Ref [31, 137] explains the dynamics of the flow separation, they do not treat the question of how the separation dynamics impact the heat transfer and film coverage.

(2) The ever-increasing turbine inlet temperature, with the aim of increasing the efficiency of gas turbines, will eventually force aerodynamicists to design engines in

[1] Part of the data reported in this chapter reprinted with permission from" Experimental Investigation of Film-Cooling Effectiveness of a Highly Loaded Turbine Blade Under Steady and Periodic Unsteady Flow Conditions" By A. Nikparto, M.T. Schobeiri, 2017, ASME Journal of Heat Transfer, 139(7), 072201, Copyright 2017 by American Society of Mechanical Engineers, and "Combined Numerical and Experimental Investigations of Heat Transfer of a Highly Loaded Low-Pressure Turbine Blade Under Periodic Inlet Flow Condition" By A. Nikparto, M.T. Schobeiri, 2018, Proc IMechE Part A: Journal of Power and Energy, Copyright 2018 by SAGE publications.

which blade cooling even in the low-pressure section is mandatory. More importantly, recent publications regarding an Ultra-High Efficiency Gas Turbine Engine (UHEGT) [104, 160] have unveiled a state-of-the-art design in which blades even in the Low-Pressure stage are exposed to relatively high temperatures.

(3) This study provides researchers with a benchmark example for future reliability analysis of commercial computational codes as well as design methods. Also, such studies can be used to develop analytical models that can serve as a quick tool for the preliminary design of cooled gas turbine engine elements [161].

8.1 Film-Cooling Effectiveness Measurement Research Objectives

Understanding the effect of the complex geometry of cooling holes, their arrangement on the turbine blades and the interaction of jets and boundary layer have required detail boundary layer, film-cooling effectiveness, and heat transfer measurements.

The Reynolds number in which these measurements will be performed (Re=150,000) is based on the suction surface length and exit velocity of the cascade. It corresponds to cruise condition in which there exists a major separation region on the suction surface of the blade. This phenomenon as studied before in Refs [67, 137], has a significant influence on heat transfer and aerodynamics of the blade. In this study, it was tried to research the effect of wake impingement on film-cooling effectiveness. Blowing ratio of the coolant, based on equal mass flow distribution through the cooling holes, will be maintained at 1 for all locations on the blade and flow coefficient was kept at 0.8 in the unsteady case.

Hot-wire anemometry was previously performed to obtain boundary layer parameters. Liquid crystal technique has also been previously used to measure the heat transfer coefficient around the blade, and finally, in this stage pressure-sensitive paint (PSP) is used for film-cooling effectiveness measurement. The unsteady cascade facility described in [12, 59, 162] is used to perform the measurements above. PSP material has to be first calibrated using a calibration facility to obtain the sensitivity curve of intensity ratio with respect to pressure ratio. Partial pressure of oxygen at different locations was registered using the same calibration curve and a CCD camera. By incorporating heat/mass transfer analogy, the film-cooling effectiveness is measured. Detail description of the test facility, as well as calibration facility and theory of heat/mass analogy, are given in the following chapters.

8.2 Film-Cooling Effectiveness Simulation Research Objectives

This part of the study is dedicated to numerically simulate film-cooling and predict film-cooling effectiveness with commercial ANSYS CFX v17.1 solver. In this the strong and weak points of RANS solvers in terms of predicting film-cooling effectiveness are thoroughly discussed. The research program intended for this part of the study covers the following steps:

8.2.1 Grid Generation

- Creating high quality unstructured grid for stationary domain (turbine cascade blade) and moving domain (moving rods).
- Ensure that y+ on both suction and pressure sides is less than one, in order to make sure that the viscous sub-layer of the boundary layer is captured.
- Perform grid independency test.

8.2.2 Steady State Modeling

- Perform steady-state simulation of flow over film-cooled low-pressure turbine blade inside the linear cascade.
- Compare the numerical simulation results with previously obtained experimental measurements.
- Discuss the effect of aerodynamic flow quantities on film-cooling effectiveness.
- Evaluate the performance of transitional SST turbulence modeling on film-cooling effectiveness in steady state flow.

8.2.3 Transient Modeling

- Perform transient analysis of unsteady flow inside the linear cascade of film-cooled low-pressure turbine blades.
- Evaluate the effect of unsteady incoming wakes on time-averaged results when compared with steady-state simulation results and experimental data.
- Evaluate performance of transitional SST model in unsteady flow.

9 EXPERIMENTAL FACILITY

9.1 Linear Turbine Blade Cascade Facility

The objective of the experimental study[1] is to investigate the effect of periodic unsteady flow on film-cooling effectiveness distribution of a highly loaded low-pressure turbine blade. In addition, experiments that were performed previously using the same cascade facility serve as a benchmark for the computational purposes.

For that purpose, a multipurpose, large-scale, subsonic research facility was used that has been in operation since 1993 [137]. A thorough description of modifications and components of the cascade facility is given below.

The test section of this facility consists of single row cascade of turbine blades. The wake passing frequency can be varied from 0 to 120 Hz to simulate various turbomachinery operating conditions. The facility in its original configuration is shown in Figure 9-1. The unique capability of this facility lies in its capability to sequentially generate unsteady inlet flow conditions using moving rods. This feature allows researchers to study different unsteady wake structures, passing frequencies, and free-stream turbulence intensities. A description of various components of the test facility is given below.

[1] Part of the data reported in this chapter reprinted with permission from" Experimental Investigation of Film-Cooling Effectiveness of a Highly Loaded Turbine Blade Under Steady and Periodic Unsteady Flow Conditions" By A. Nikparto, M.T. Schobeiri, 2017, ASME Journal of Heat Transfer, 139(7), 072201, Copyright 2017 by American Society of Mechanical Engineers, and "Combined Numerical and Experimental Investigations of Heat Transfer of a Highly Loaded Low-Pressure Turbine Blade Under Periodic Inlet Flow Condition" By A. Nikparto, M.T. Schobeiri, 2018, Proc IMechE Part A: Journal of Power and Energy, Copyright 2018 by SAGE publications.

9.1.1 Air Supplier

The research facility consists of a large centrifugal fan, a diffuser, a settling chamber, a nozzle and a turbine cascade test section, as shown in Figure 9-1. The centrifugal fan has a maximum volumetric flow rate of 15 m^3/s and is driven by a 93 KW (125 hp), 3-phase AC electric motor running at a rated speed of 1760 rpm which is reduced to the fan speed of 1035 rpm by a belt-pulley transmission. It is capable of generating a maximum mean velocity of 100 m/s at the test section inlet. A variation of inlet velocities and hence Reynolds numbers can be obtained by changing the position of the throttle valve located at the fan exit. For film-cooling effectiveness experiments, the throttle is adjusted to give a Reynolds number of 150,000 at the inlet of the test section. With regard to high-pressure turbine blade benchmark data, the throttle was adjusted to

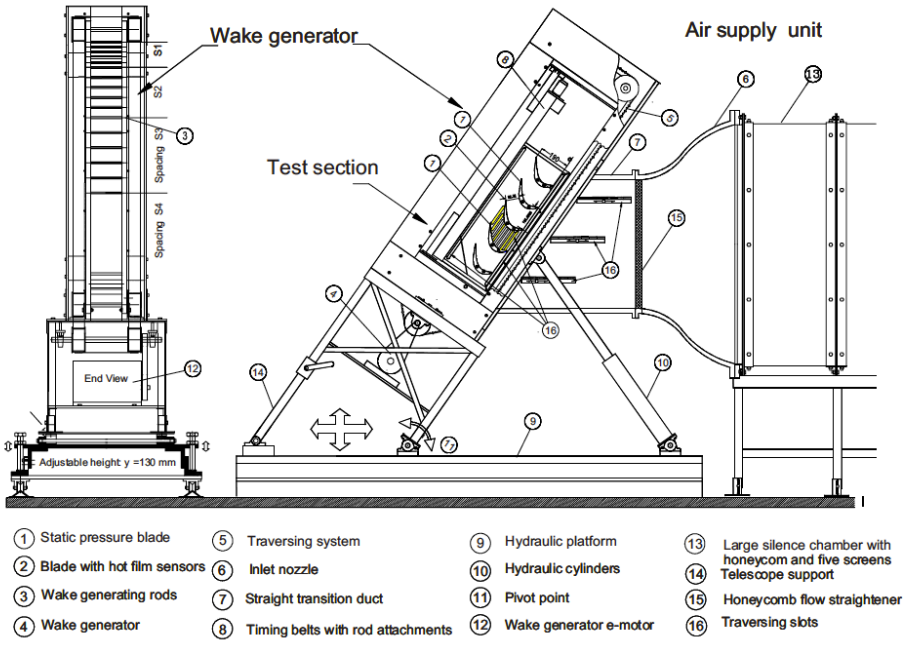

Figure 9-1 Turbine cascade test section at TPFL with components and adjustable test section as described in Refs [12, 15, 59, 67, 137, 162, 163]

produce a Reynolds number of 400,000 based on suction surface length and cascade exit velocity.

9.1.2 Diffuser, Settling Chamber, And Nozzle Assembly

A diffuser, located downstream of the straight pipe, decelerates the flow before entering the settling chamber. The diffuser is 1500 mm long and has an area ratio of 1:4.75. The settling chamber is made of four sections, each section is 900 mm long and has a cross-section of 1500mm×900mm. A number of screens along with a honeycomb flow straightener were used to ensure flow uniformity and turbulence intensity. The screens are made of stainless steel and have different mesh sizes and wire diameters.

The honeycomb and screen combination reduce the scale of vortices generated by the diffuser vanes. The first screen is located immediately after diffuser exit followed by honeycomb flow straightener between the first two settling chambers. Remaining screens are located downstream from the second, third and fourth settling chambers. The combination of screens and honeycomb flow straightener break down the large eddies exiting from the honeycomb cells into smaller eddies and provide a more uniform flow. A nozzle is used (as shown in Figure 9-1) downstream from the last settling chamber to accelerate the flow before crossing wake generators and test section. This nozzle has an area ratio of 6.75:1, for low-pressure turbine test case and 1.48 to 1 for high-pressure turbine case. A straight channel transition piece is used and placed between the nozzle and test section to accommodate the test section inclination.

9.1.3 Periodic Unsteady Wake Generator

In order to study the effect of two-dimensional wakes on film-cooling effectiveness distribution on the low-pressure turbine cascade, this facility is equipped with periodic

unsteady wake generators. In this facility, the two-dimensional unsteady wakes are produced by the translational motion of cylindrical rods attached on both sides to timing belts driven by an electric motor with the maximum power of 7.5 KW (10 hp) and a maximum rotational speed of 1745rpm. This system is equipped with a controller that allows the belt translational speed up to 25 m/s. In the current study, belt velocity of U=7.52m/s was chosen in order to maintain the flow coefficient of Φ=0.8. The timing belts, with the length of 4.96 m, span over five shaft-pulleys. The rod diameter and rod spacing can be varied to simulate the wake width and spacing that stem from the trailing edge of the rotor blades. The rod diameter and distance are chosen according to the criteria outlined by Schobeiri, et al. [164]. For current investigation, a constant rod diameter of D_R=2.5mm was chosen. The rod spacing can be varied by attaching or removing the rods to or from the timing belts. In the current study, rod-spacing is set to S_R=80mm. The translational speed of the timing belts was monitored using a fiber optic system. Figure 9-2 shows the wake generator system.

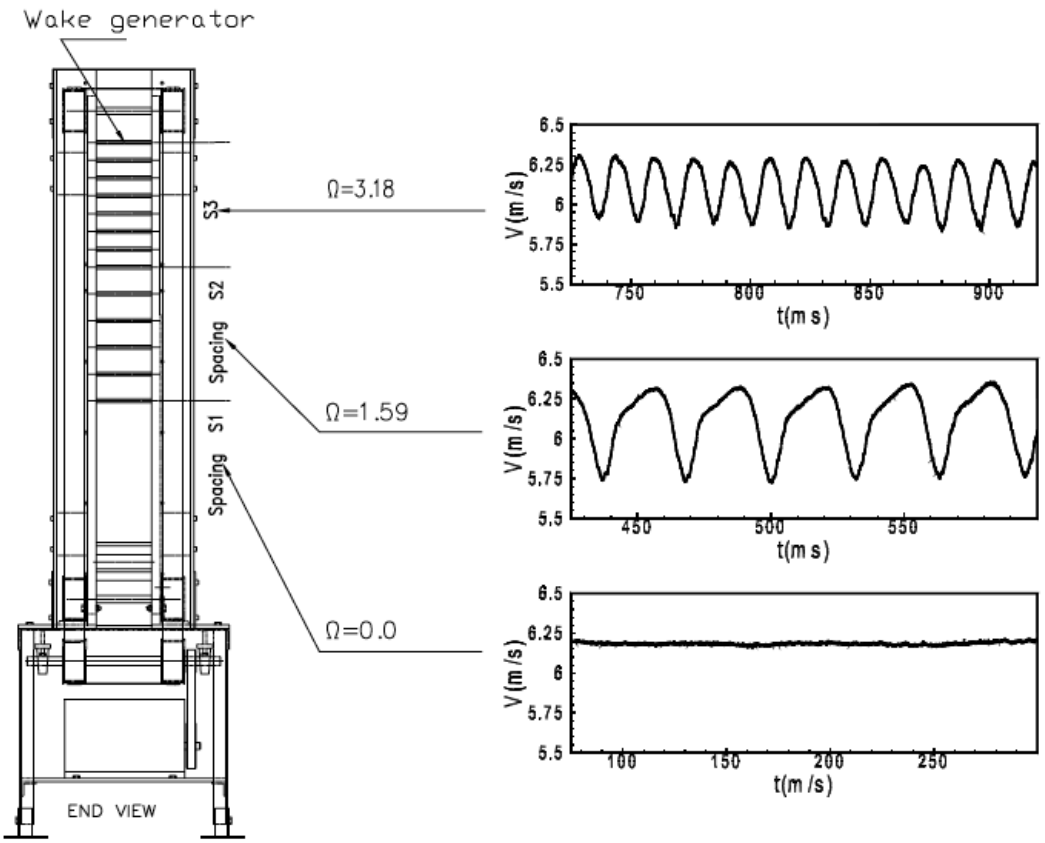

Figure 9-2 Wake generator system [67, 165]

Researchers normally use Strouhal number as an unsteady flow parameter, which includes wake frequency and inlet flow velocity. In this study, however, the reduced frequency is used as an index of unsteadiness of the flow with the following mathematical description.

$$\Omega = \frac{c}{S_R}\frac{U}{V_{ax}} = \frac{\sigma}{\phi}\frac{S_B}{S_R} \tag{9-1}$$

The reason behind this decision is that it includes cascade solidity, flow coefficient, blade spacing and rod spacing as well as previously mentioned parameters. For that reason, it could be considered as an extension to Strouhal number. Table 9-1 lists the cascade geometry and flow parameters.

Table 9-1 Cascade geometry and parameters

Parameters	Values
Inlet Velocity	$V_{in} = 5\ m/s$
Nozzle Width	$W = 200.0\ mm$
Blade chord	$c = 203.44\ mm$
Blade axial chord	$c_{ax} = 182.85\ mm$
Blade suction surface length	$L_{ss} = 270.32\ mm$
Inlet air angle to the cascade	$\alpha_1 = 0\ deg$
Inlet turbulence intensity	$Tu_{in} = 1.9\%$
Blade Re-number	$Re = 150{,}000$
Blade height	$h_B = 200\ mm$
Cascade solidity	$\sigma = 1.248$
Cascade angle	$\varphi = 55\ deg$
Belt velocity	$U_w = 7.52\ m/s$
Exit air angle from the cascade	$\alpha_2 = 90\ deg$
Flow coefficient	$\phi = 0.8$
Reduced Frequency	$\Omega = 3.18$

9.1.4 Turbine Blade Cascade Test Section

Cascade test section is located immediately downstream from the wake generators. It has an inlet cross-section of 1000mm×200mm. Five turbine blades were implemented inside the cascade facility. This blade number is necessary and sufficient to ensure the spatial periodicity of the flow [67, 165]. Regarding the film-cooling effectiveness study, low-pressure turbine blades designed by Pratt&Whittney were implemented in the cascade. The blade is designed in such a way that typical flow features such as laminar flow separation and boundary layer transition that are normally witnessed in low-pressure

turbine blades can be seen. The cascade geometry is shown in Figure 9-3 contains stagger and flow angles. The blades are attached to two Plexiglas sidewalls tightly.

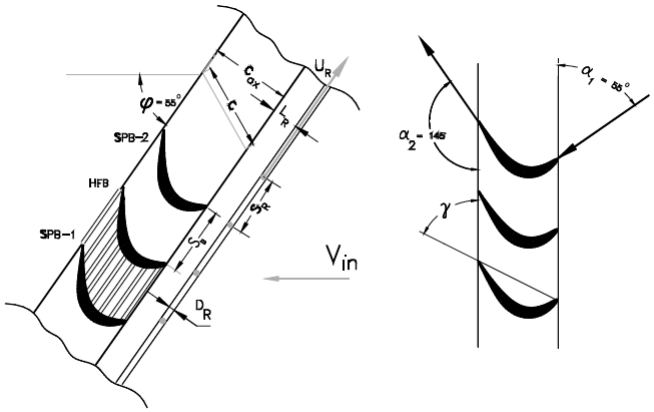

Figure 9-3- Cascade geometry with flow and stagger angles. Image courtesy of Refs [15, 67, 137]

This research facility is capable of producing 1.9% free-stream turbulence intensity in wake-less condition [30, 162]. In unsteady flow cases, higher free-stream turbulence intensity is achieved due to the wakes. For low-pressure turbine blade study, the free-stream turbulence intensity could be artificially increased up to 13% using turbulence grids installed in the chamber.

The cascade test section is shown in Figure 9-4 for low-pressure turbine blades. In this facility, the blades are inserted into two vertical Plexiglas side-walls. One of the side-walls has the boundary layer slot integrated into it as well as inlet and exit traversing slots. The turbine blades used for aerodynamics measurements are specially manufactured for boundary layer, surface pressure, and heat transfer measurements. To measure surface pressure at different locations, a blade was manufactured with static pressure taps, and for heat transfer measurement, a separate blade was instrumented with internal foil and liquid crystal.

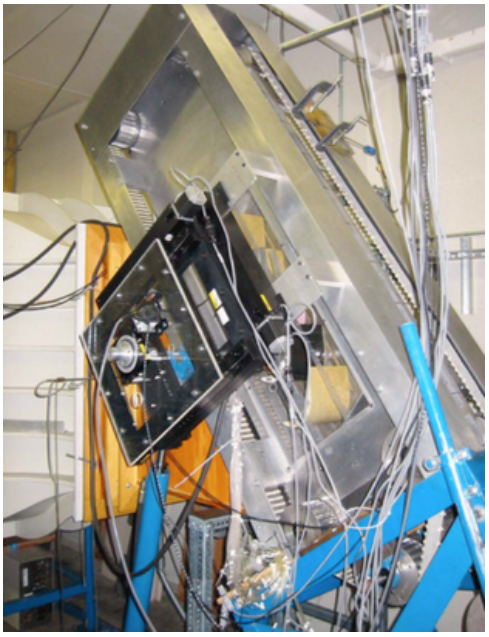

Figure 9-4 Linear cascade test section for low-pressure turbine blade [16]

Two-dimensional unsteady wakes were produced by the translational motion of wake generators as described before. Also, reduced frequency concept was used to characterize the motion of the rods.

9.1.4.1 Heat Transfer Turbine Blade

The heat transfer measurements from the blade under different working conditions was performed using an instrumented blade with internal heater and liquid crystal sheet. A Styron 10V-200A DC power supply supplies the power required for heating the blade. The current passing through the heater is measured using a multimeter and a shunt resistor. Finally, the yellow-band tracking method is used to record the data. The location of yellow band is controlled using the amount of power supplied to the blade by the power supply. Three different rod spacings are used for Low-Pressure Turbine blade measurements (Ω=3.18, 1.59 and ∞), and the high-pressure turbine blade measurements

were performed only at two reduced frequencies (Ω=1.57 and ∞). The following table summarizes the geometry and parameters for.

Table 9-2 Specification of inlet flow and wake generator characteristics for cascade test sections

Parameter	Low-pressure turbine blade
Axial velocity	V_{ax}=4, 5 and 8 m/s
Blade inlet flow angle	$\alpha_1=0^o$
Blade height	L=200.0 mm
Blade chord	C=203.44 mm
Cascade solidity	σ= 1.248 mm
Steady Reference point (no-rods)	$S_R=\infty$
Cluster 1 rod spacing	S_R=320.0 mm
Cluster 2 rod spacing	S_R=160.0 mm
Inlet turbulence intensity	Tu=1.9 and 13%
Blade exit metal angle	$\alpha_1=90^o$
Blade spacing	S_B=160 mm
Blade Re-number	Re_c=110,000/150,000 and 250,000
Cascade flow coefficient	ϕ=0.8
Rod diameter	D_R=2mm

9.1.5 Hydraulic Platform

To account for high flow deflection of this particular low-pressure turbine blade, the entire cascade test section along with the wake generators are modified to allow precise angle adjustments of the cascade relative to the flow. This is achieved by the use of a hydraulic platform, which simultaneously lifts and rotates the entire cascade test section.

10 EXPERIMENTAL PROCEDURE

In this chapter and the next[1], film-cooling effectiveness of a Low-Pressure Turbine blade in a linear turbine blade cascade has been studied under realistic flow conditions. The following includes the measurement theory, instrumentation, data acquisition and calibration procedure in this experimental study.

10.1 Film-Cooling Effectiveness Measurement Theory and Data Analysis

Film cooling as explained by Goldstein [166] is the introduction of secondary fluid (coolant) at one or more discrete locations along a surface exposed to a high-temperature environment to protect that surface not only in the immediate region of injection but also in the downstream region. This technique is being widely used to protect airfoil surfaces, shrouds, tips and end-walls from excessive corrosion and reduce the heat load. Schematic of film cooling concept is shown in Figure 10-1.

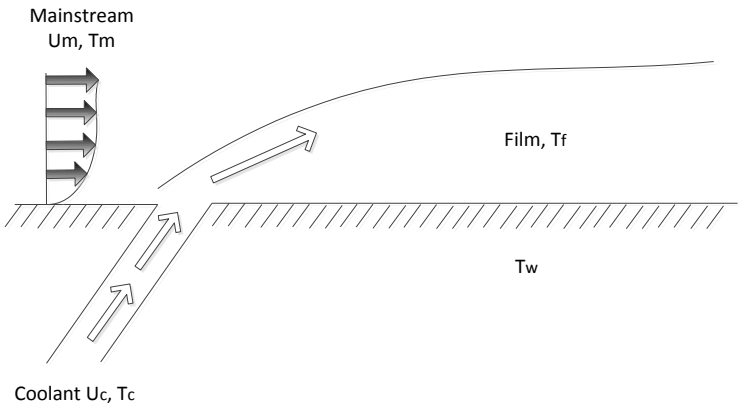

Figure 10-1 Schematic of film cooling concept

The effectiveness of film-cooling is recorded by measuring the temperature differential between the mainstream and the coolant. The film-cooling effectiveness could

[1] Part of the data reported in this chapter and the next is reprinted with permission from" Experimental Investigation of Film-Cooling Effectiveness of a Highly Loaded Turbine Blade Under Steady and Periodic Unsteady Flow Conditions" By A. Nikparto, M.T. Schobeiri, 2017, ASME Journal of Heat Transfer, 139(7), 072201, Copyright 2017 by American Society of Mechanical Engineers.

be estimated by recording the surface temperature along with coolant and mainstream temperatures, in case the cooled surface is made from low conductivity material.

10.1.1 Heat/Mass Transfer Analogy Theory

Manufacturing the test piece from low-conductivity material and incorporating mass transfer analogy method is very popular among researchers as it eliminates conductivity related errors and more importantly, techniques that fall under this category are non-intrusive which offers a great advantage. For the same reasons, this method provides acceptable and reliable results.

Figure 10-2 shows thermal and viscous boundary layer. As shown and expressed in this figure, the concentration/temperature is a function of both x and y (x is the stream-wise direction while y is the normal distance from the plate). Wall concentration/temperature is the only function of x.

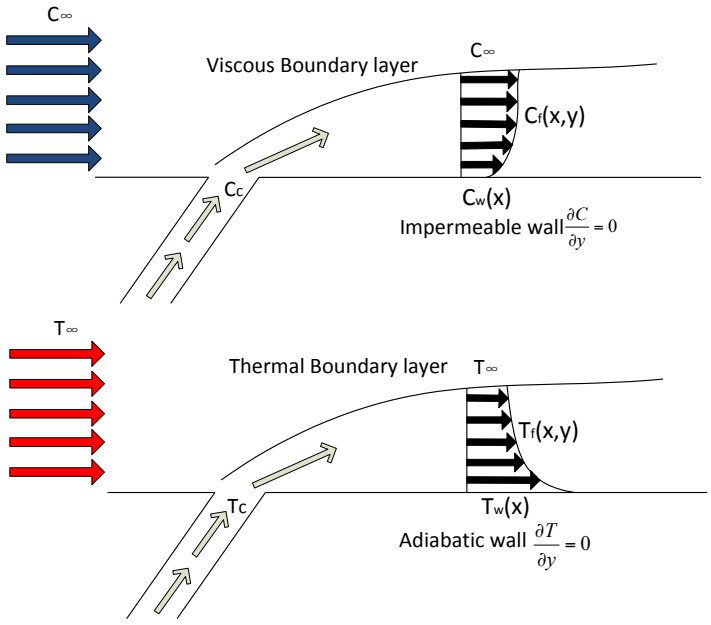

Figure 10-2 thermal and viscous boundary layer

The governing heat transfer equation as expressed in Ref [167] is:

$$G_x \frac{\partial T}{\partial x} + G_y \frac{\partial T}{\partial y} = \rho\left(\varepsilon_T + \alpha_D\right)\frac{\partial^2 T}{\partial y^2} \quad \textbf{(10-1)}$$

In this equation, α_D and ε_T are thermal diffusivity and turbulent thermal diffusivity respectively. The boundary conditions required to solve equation (10-1) are:

$$y = 0, \frac{\partial T}{\partial y} = 0 \quad \textbf{(10-2)}$$

$$y = 0, T = T_{aw} \quad \textbf{(10-3)}$$

$$y = \delta, T = T_\infty \quad \textbf{(10-4)}$$

$$x = 0, T = T_c \quad \textbf{(10-5)}$$

Similarly, mass transfer equation has the same mathematical description and boundary conditions. Considering C_∞ is the tracer concentration of the mainstream and C_c is the tracer concentration of the coolant, the mass transfer equation can be written in the following form where D is mass diffusion and ε_M is turbulent mass diffusivity.

$$G_x \frac{\partial C}{\partial x} + G_y \frac{\partial C}{\partial y} = \rho\left(\varepsilon_M + D\right)\frac{\partial^2 C}{\partial y^2} \quad \textbf{(10-6)}$$

$$y = 0, \frac{\partial C}{\partial y} = 0 \quad \textbf{(10-7)}$$

$$y = 0, C = C_W \quad \textbf{(10-8)}$$

$$y = \delta, C = C_\infty \quad \textbf{(10-9)}$$

$$x = 0, C = C_C \quad \textbf{(10-10)}$$

Comparing equations (10-1) and (10-6), one can notice the similar structures of these two equations. Also, the corresponding boundary conditions are identical in expression. This means that the two equations of mass and heat transfer have similar

solutions and in the event that turbulent Lewis number $\left(Le_T = \frac{\alpha+\epsilon_T}{D+\epsilon_M}\right)$ is equal to unity; they both will result in completely identical solutions. Refs [167, 168] among others have shown that the unity Lewis number assumption is valid especially for turbulent flow fields. Therefore film-cooling effectiveness can be expressed in-terms of concentrations:

$$\eta = \frac{T_f - T_\infty}{T_c - T_\infty} \tag{10-11}$$

Since T_f is almost equal to T_{aw} which results in:

$$\eta \approx \frac{T_{aw} - T_\infty}{T_c - T_\infty} \approx \frac{C_W - C_\infty}{C_c - C_\infty} \tag{10-12}$$

The underlying assumptions for mass transfer analogy ($Le_T=1$) require the flow to be highly turbulent while in low-pressure turbine blade especially in low Reynolds number the flow has more of a transitional nature. Since flow transition is hastened due to introduction of highly turbulent cooling jets [147], we can incorporate this technique to measure the effectiveness of film coverage in transitional regime.

10.1.2 Heat/Mass Transfer Analogy Methods

Numerous experimental methods have used mass-transfer analogy concept to measure film-cooling effectiveness indirectly. It is a very popular method since it inherently avoids conduction related issues. Nicoll and Whitelaw [169] used gas chromatographic equipment to detect the concentration of the tracer gas at various discrete locations and estimated film-cooling effectiveness using mass transfer analogy.

Goldstein and Taylor [170] used naphthalene sublimation technique to measure local convection coefficient and other local transport coefficients. In a subsequent study, Goldstein and Spores [171] incorporated the same measurement method to find mass and

eventually heat transfer coefficients in the neighborhood of a row of jets entering a cross flow on the end-wall region of a linear turbine blade cascade. Later, Goldstein and Jin [172] studied the film-cooling effectiveness downstream of rows of discrete holes with inclination and compound angles using the same technique. They found film-cooling effectiveness by comparing mass transfer coefficient obtained by injecting naphthalene-vapor-saturated air with pure air injection. Another popular method in mass transfer analogy category to measure film-cooling effectiveness is ammonia and diazo method that is a surface visualization method. The first measurement using this technique was conducted by Friedrichs, et al. [173]. They calibrated the traces of ammonia gas on diazo paper and measured film cooling effectiveness by using ammonia and water-vapor seeded in coolant air.

Among other popular mass transfer analogy methods that we can point out are swollen polymer, initially presented by Macleod and Todd [174], and Thermographic phosphors proposed by Noel, et al. [175].

10.1.2.1 Film-Cooling Effectiveness Measurement Using PSP Method

Pressure-Sensitive Paint method was first proposed by Zhang and Jaiswal [176]. This method is based on oxygen-quenched photo-luminescence property of Pressure-Sensitive Paint. Certain compounds with this property emit light after being excited by a suitable light source. The intensity of the emitted light is proportional to the partial pressure of oxygen, which directly relates to the pressure of the surrounding gas containing oxygen. Figure 10-3 shows the principle of operation of PSP material. In fact, it is the sensitivity of photo-luminescent molecules that make the PSP technique possible. Once a photo-luminescent molecule is excited by a photon, it emits a photon at a different

wavelength, which causes the molecule to return to its ground level. Oxygen quenching property of some certain photo-luminescent molecules allows them to return to their ground level energy in the presence of oxygen without emitting photon. Hence the intensity of emitted light from the photo-luminescent material is inversely proportional to the local partial pressure of oxygen. The emitted light intensity can be recorded using a CCD camera, and the corresponding partial pressure of oxygen could be obtained through a calibration curve that relates the light intensity ratio to pressure ratio.

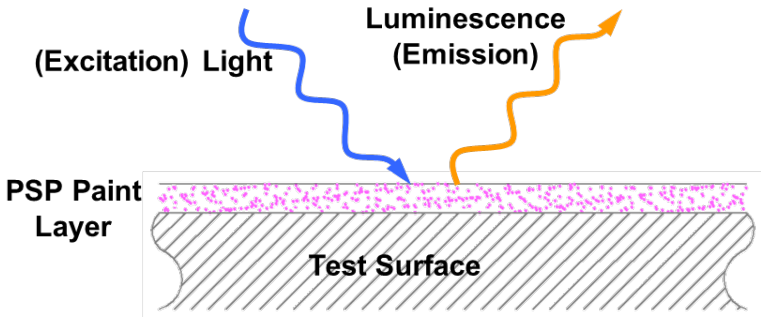

Figure 10-3 Working principle of PSP. Image courtesy of Ref [177]

Figure 10-4 shows the emission spectra of UNIFIB PSP used in this study. This graph is provided by the PSP manufacturer, Innovative Solutions Inc. This Figure clearly shows the difference between excitation and emission wavelengths. Similar to the calibration process, the intensities produced by background noise have to be removed from the image intensity obtained from cascade facility under working condition. They are then normalized with reference image intensity taken under no-flow condition.

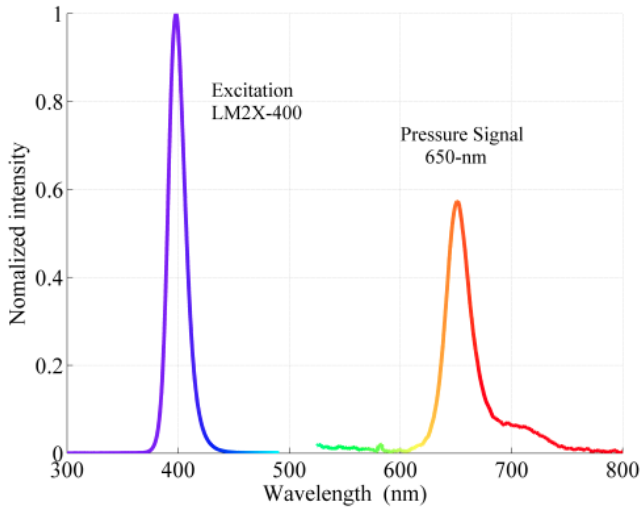

Figure 10-4 Emission spectra of UNIFIB. Provided by PSP manufacturer (Innovative solutions)

The resulting intensity ratio is then converted to pressure ratio using the previously obtained calibration curve.

$$\frac{P}{P_{ref}} = f\left(\frac{I - I_{blk}}{I_{ref} - I_{blk}}\right) \tag{10-13}$$

If mainstream is air, which is about 70% Nitrogen, and the coolant is 100% Nitrogen then the film-effectiveness could be expressed through comparison of Oxygen concentration. Nitrogen has almost the same molecular weight as air. By noting the difference between the light intensity of the two cases, film-cooling effectiveness can be determined using these equations:

$$\eta = \frac{C_{mix} - C_{air}}{C_{N_2} - C_{air}} = \frac{C_{air} - C_{mix}}{C_{air}} = \frac{\left(P_{O_2}\right)_{air} - \left(P_{O_2}\right)_{mix}}{\left(P_{O_2}\right)_{air}} \tag{10-14}$$

In this equation C_{air}, C_{mix} and C_{N_2} are oxygen concentration, air/nitrogen concentration and finally nitrogen concentration on the test surface respectively. These concentration values are directly proportional to the partial pressure of oxygen. Wright, et

al. [178] and also Rallabandi, et al. [179] compared the film-cooling effectiveness results obtained by this method with results of conventional measurement techniques such as steady-state and transient liquid crystal, IR-thermography, naphthalene mass transfer and traditional foil heater with thermocouples. They demonstrated that among all measurement methods, PSP technique demonstrates most reliability and accuracy.

10.2 Instrumentation and Data Acquisition

The blade was instrumented with white color base paint and pressure-sensitive paint and was placed inside the test section of the cascade facility. The following contains the details of the experimental set up and data acquisition system.

10.2.1 CCD Camera, Light Source, and Function Generator

To conduct the film-cooling effectiveness measurement using Pressure Sensitive Paint (PSP) technique, a strobe light source along with a CCD camera is used to excite the PSP layers and record the intensity of the incoming light respectively. More details about the theory regarding this method are given in the following chapters. The target surface was coated with nine layers of Uni FIB Pressure-Sensitive Paint developed by Innovative Scientific Solutions and is excited by a strobe light fitted with a narrow bandpass interference filter with an optical wavelength of 520nm. The time response of the paint is 300ms and pressure sensitivity is greater than 0.5% per psi. The excitation range for this specific paint is 380nm to 520nm, and the Emission range is 620nm to 750nm. Upon excitation from this green light, the PSP coated surface emitted red light with a wavelength higher than 600nm that is going to be recorded by a CCD camera.

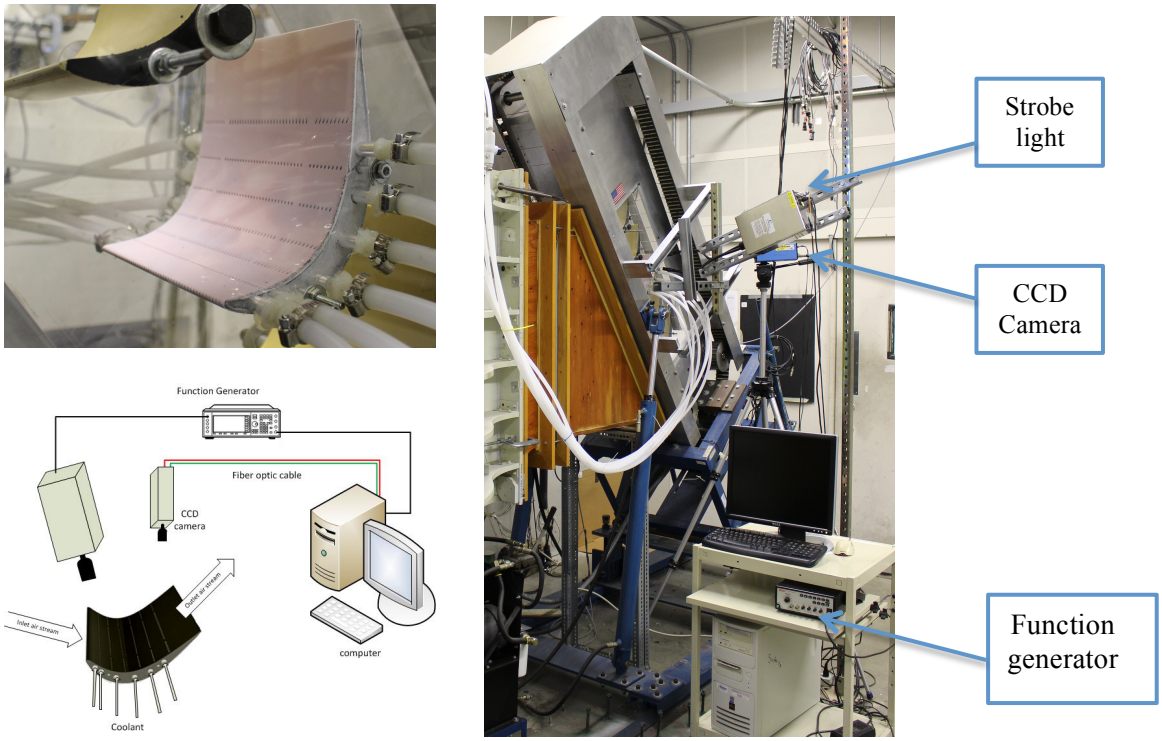

Figure 10-5 instrumented blade, schematic of setup and experimental setup [180]

A 12-bit scientific grade CCD camera (Highspeed SensiCam with CCD temperature maintained at -15^{o}C and using a two-stage Peltier cooler) outfitted with a 35mm lens and 600 nm long pass filter was used to record intensity images. The long-pass filter was used to remove the reflected portion of the incoming light for the target surface and to record only the emitted light. The camera generates 12 bit (4096 grey level) images with 640(horizontal)×480(vertical pixels). The pictures are saved on a PC using a PCI interface board. The camera, the strobe light, and the data acquisition system were triggered simultaneously using a function generator. The entire test section and experimental setup are shown in Figure 10-5.

10.2.2 Five-Hole Probe

The velocity at the inlet of the test section is measured using a fully calibrated five-hole probe. The five-hole probe is calibrated to be able to measure pressures with flow velocity, and direction with pressure values read from different ports. The calibration is highly dependent on the flow velocity, and it was calibrated using the non-nulling technique in a calibration facility in TPFL. More information regarding calibration of the five-hole probe and the calibration process is given in the following section.

10.3 Calibration Procedure

The five-hole probe and the pressure sensitive paint were calibrated at TPFL. The following contains the details of he calibrations process.

10.3.1 Five-Hole Probe Calibration

The accurate calibration of the probe is necessary and is a prerequisite in the measurement of flow quantities such as mainstream velocity and velocity fluctuation. The entire purpose of the calibration process is to eliminate parasitic effects and if done properly certainly boosts the reliability of the gathered data. The facility used in these experiments to calibrate five-hole probe is shown in Figure 10-6.

Detail descriptions of the calibration facility as well as the calibration procedure and calibration theory are given in detail in Refs [102, 177]. For that reason, only a brief description is given here. Compressed air enters the calibration facility after it is drawn from a reservoir and passes through a pressure regulator, filter and flow control valve. As shown in the figure, it consists of a settling chamber, pipe, and three axisymmetric sections. The diameter of the sections and all other dimensions are shown in Figure 10-6. The inlet and outlet of the nozzle are parallel to the axis of the facility. The nozzle is fed

from a 120 psi pressure line that creates a uniform jet. The temperature of the incoming air into the facility is constantly being monitored using several thermocouples in the first section of the facility. Also, using several pressure taps along with pressure transducers located in the last section of the pipe, the pressure difference between atmospheric pressure and the static pressure inside the pipe can be registered. The system is designed in such a way that the probe end is maintained at the center of exiting jet (Figure 10-7).

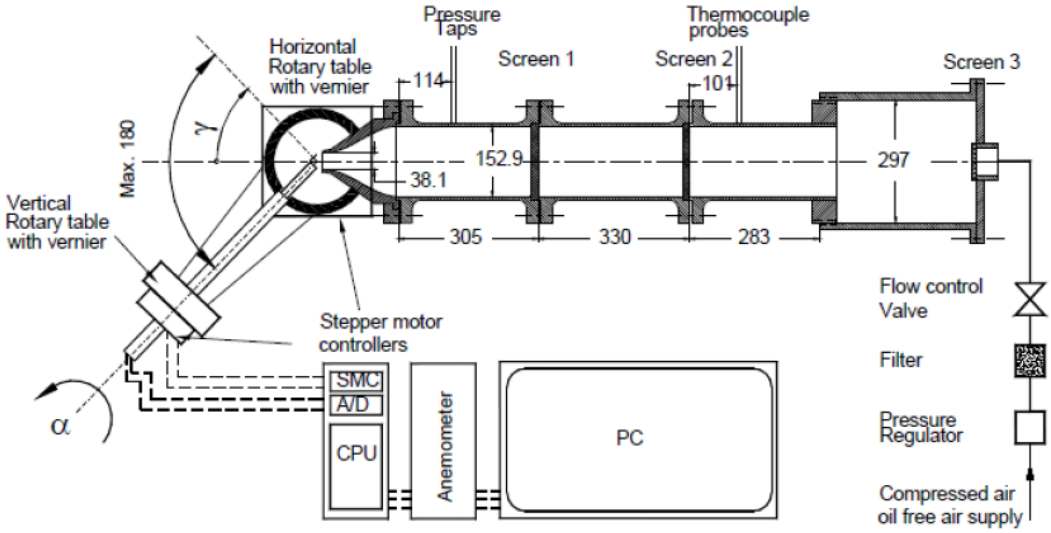

Figure 10-6 Five hole probe calibration facility[102]

This calibration facility is fully automated. Using an angular indexing mechanism, the pitch and yaw angles are changed within the range of -20 to +20 degrees in 20 increments. Two computers controlled stepper motors are used for this purpose. The stepper motors are mounted on a traversing system with an arm at 90^{o}. TURBOPROBE, an in-house computer algorithm developed in TPFL is used for the purpose of calibration. It creates a grid of pitch and yaw angles. The generated grid is then swept using the TURBOPROBE and stepper motors. Also, the pressure from the five pressure ports are registered using a PSI-9016 pressure scanner, and then the acquired data is stored in a file

along with corresponding pitch and yaw angles and calibration nozzle total pressure. This data file is then used to create calibration surfaces for the probe that are eventually used to find the velocity magnitude and direction.

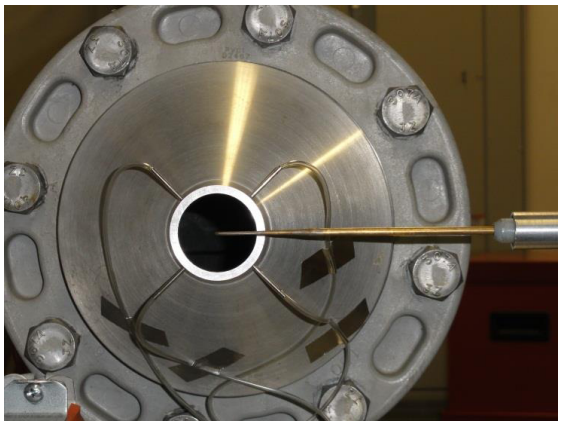

Figure 10-7 The probe tip is always maintained at the center of the nozzle outlet. Image courtesy of Ref [177]

The method introduced by Rubner and Bohn [181] is used to construct calibration surfaces. The advantage of this method over other methods that normally use an algebraic average of the static pressure of outer four holes is that it is also valid for adverse flow angles where one of the holes is located in the separated flow zone.

10.3.2 Pressure-Sensitive Paint Calibration

PSP measurement theory is extensively discussed in early sections of Chapter 4. In this section, only the description of PSP calibration facility and calibration procedure are given. Calibration of PSP was done several times using a vacuum/pressure chamber at several known pressures varying from 0 to 2 atm. As the pressure is varied from 0 to 2 atm, the corresponding intensity of the light emitted from calibration piece was recorded and later was used to construct the calibration curve. The vacuum/pressure chamber and schematic of calibration setup is shown in Figure 10-8.

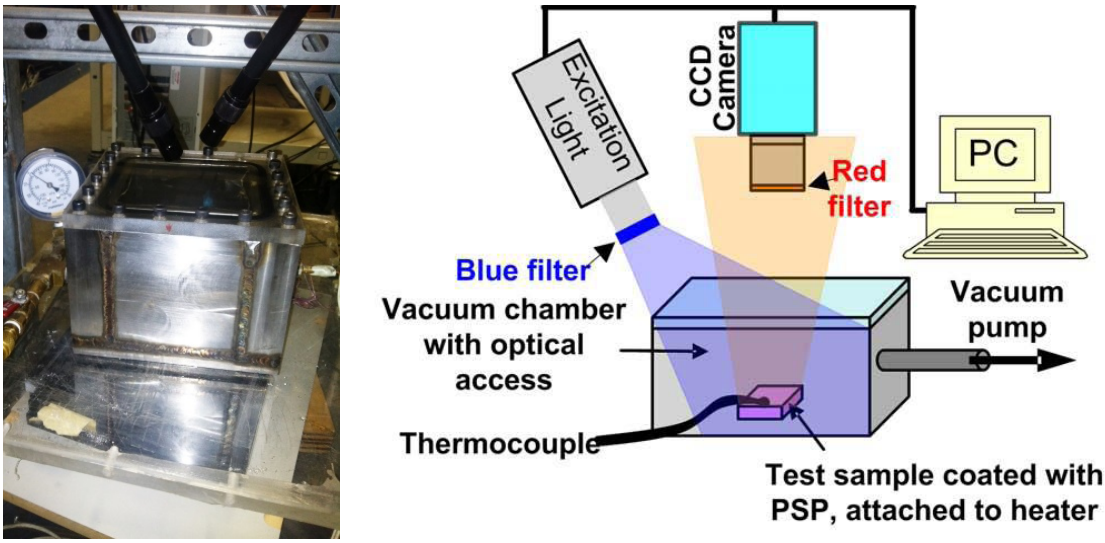

Figure 10-8 Vacuum/Pressure chamber (left) and schematic of calibration setup (right). Image courtesy of [177]

The test piece used for calibration purpose is made from the same material and same surface finish of the film-cooled low-pressure turbine blade.

To test the effect of the base paint on calibration curve and uncertainty, the test specimen was once covered with white and once with black paint before applying PSP on top of it. Then the same number of layers of PSP that is eventually applied on blade surface was sprayed on top of the calibration piece. To ensure uniform and similar thickness of PSP, the air-brush was held at the same specific distance and was always maintained perpendicular to the specimen. Then it was moved over the specimen at a constant speed. Figure 10-9 shows the two specimens with different base paint used in the calibration process.

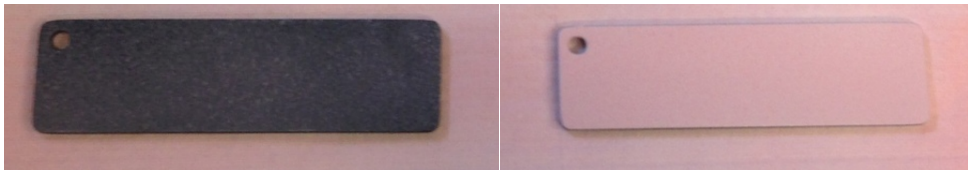

Figure 10-9 Calibration specimen covered with black base paint (left) and white base paint (right)

The intensity of the light emitted from PSP is recorded by the CCD camera during data acquisition and is then normalized with a reference image intensity taken under no-flow condition (for the calibration purpose, zero gauge pressure condition is assumed no-flow condition). To remove the background noise in optical setup from results, image intensity under the no-flow condition and no excitation is removed from image intensities and reference image intensities. The resulting intensity ratio and pressure ratio are mathematically related and the relationship between the two ratios is obtained from the calibration process.

$$\frac{I - I_{blk}}{I_{ref} - I_{blk}} = f\left(\frac{\left(P_{O_2}\right)_{air}}{\left(P_{O_2}\right)_{ref}}\right) = f\left(P_{ratio}\right) \qquad \textbf{(10-15)}$$

I denotes the intensity obtained for each pixel and $f(P_{ratio})$ is the relationship between pressure and intensity ratios obtained from calibration. Figure 10-10 shows the calibration curves obtained from calibration process of black (left) and white (right) specimen. The error bars are also included in the plots. The uncertainties of image-intensity ratios were calculated by finding the standard deviation of image intensities and propagation of uncertainty theorem. Comparison of the two plots presented above shows that the reasonable choice for base paint would be white color as it significantly reduces the uncertainty in image intensity ratio.

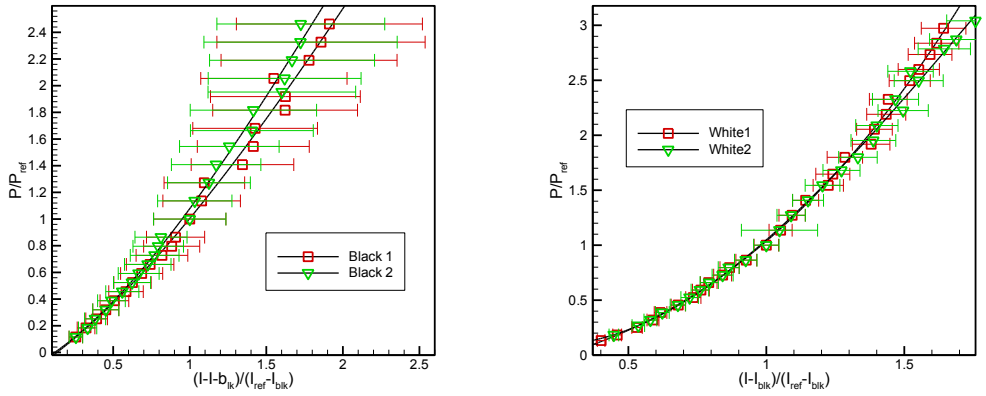

Figure 10-10 Calibration curve for black (left) and white (right) specimen

PSP is normally sensitive to temperature as well. Higher temperatures result in lower emitted light intensity. Hence for accurate measurement, the paint has to be calibrated for temperature as well. However, there is a method to eliminate temperature sensitivity of the results. It was observed that in case the taken image intensities are normalized with reference image intensity taken at the same temperature, the temperature sensitivity could be eliminated. Hence to avoid errors related to temperature variation, the reference images, in both calibration and data acquisition, were taken immediately after the experiment was completed.

10.4 Film-Cooling Effectiveness Measurement Experimental Procedure

This study measures the film-cooling effectiveness of a film-cooled low-pressure turbine blade under steady and periodic unsteady inlet flow conditions. The blade is manufactured using 3D printing technique and has six coolant passages inside. Coolant is injected into each passage. Each passage feeds one row of holes on the suction side and one row on the pressure surface of the blade. There are a total of 617 holes on the blade,

which are distributed along thirteen different rows. Six rows cover the suction side, six other rows cover the pressure side, and one last row feeds the leading edge.

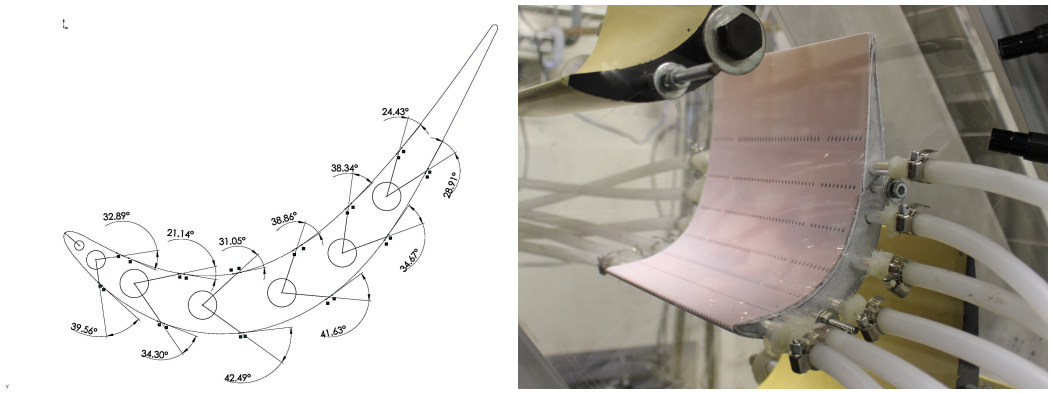

Figure 10-11 Cross section of the blade and the Instrumented blade inside the cascade [180]

The holes are shaped holes to provide better and more effective film coverage. It is obvious that the passage and horseshoe vortices deflect the coolant flow toward the blade midspan, especially on the suction surface [182, 183]. To counter this and provide better coverage for the near end-wall regions of the blade that are most susceptible to this effect, nearby holes have compound angle as well. Figure 10-11 shows the cross-section of the blade as well as instrumented blade inside the cascade facility. This figure shows the ejection angles. The blade in this study is covered initially by base coat (white color), and later nine layers of pressure sensitive paints were sprayed on top of that using airbrush. The airbrush was held perpendicular to the blade at a specified distance from it. It was then moved over the blade in a reciprocating manner at a constant and known speed to ensure about the uniformity of thickness of the PSP coating. The number of coats needed to paint the blade depends on the type of paint that has been used.

During numerous tests, it has been determined that this number of layers provides acceptable sensitivity to get sufficient response in intensity for small pressure changes.

As mentioned, the surfaces of the blade were excited using strobe light fitted with a narrow bandpass interference filter with an optical wavelength of 520nm. Upon excitation, the PSP coated surface emits red light with a wavelength of minimum 600nm. To record the intensity, a CCD camera was used. This CCD camera fits with a 35 mm lens and was used along with a long-pass filter to record intensity images. A schematic and picture of data acquisition setup are shown in Figure 10-5.

To obtain uncertainty of the PSP method, Kline and McClintock [184] method was used. The uncertainty of FCE varies along the blade surface. In the regions with effectiveness magnitude of 0.8 and higher, uncertainty drops below 1% while for regions with the effectiveness of 0.07% uncertainty can be as high as 10.3%.

10.5 Perspective Correction

Since the blade is relatively large (C_{ax}=182mm), illuminating the whole surface with the strobe light uniformly is impossible. Also due to the same problem, the whole blade could not be captured within one shot with all the details that are subject to study. To solve this problem, the research team illuminated different locations on the blade surfaces individually and took pictures of different regions. Since the camera can never be held perpendicular to the surface, the perspective correction has to be applied to the obtained images. Figure 10-12 shows the different illuminated regions. These regions are merged after the film cooling effectiveness is measured.

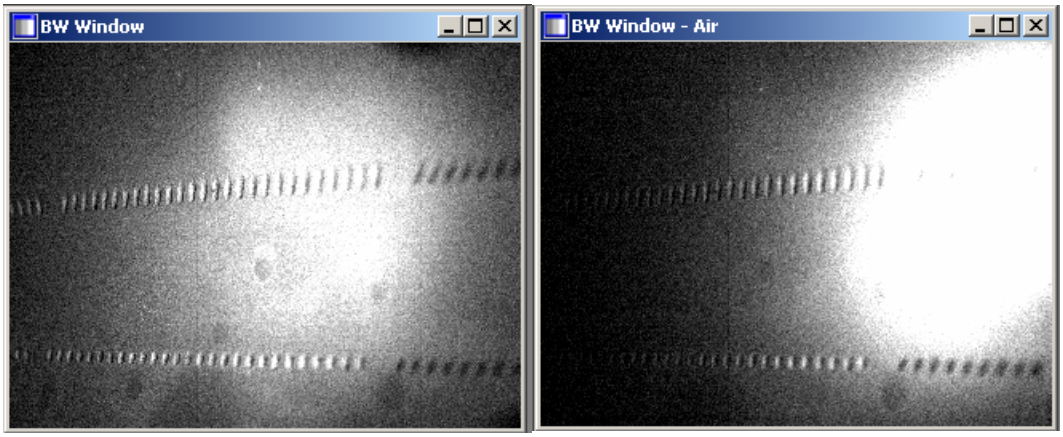

Figure 10-12 Different regions are illuminated separately and then merged

Later when the pictures are merged, they were corrected for perspective. Figure 10-13 shows that the angle at which the camera captures the images and a raw image obtained from the same angle. Perspective effect is clearly seen in this picture.

The perspective correction program is written in MATLAB. This program is written to rectify oblique images. For that reason, the image has to be of a planar surface. For the region close to trailing edge on both sides of the blade, the planar assumption of the surfaces holds true. However the same assumption is not going to be valid for other

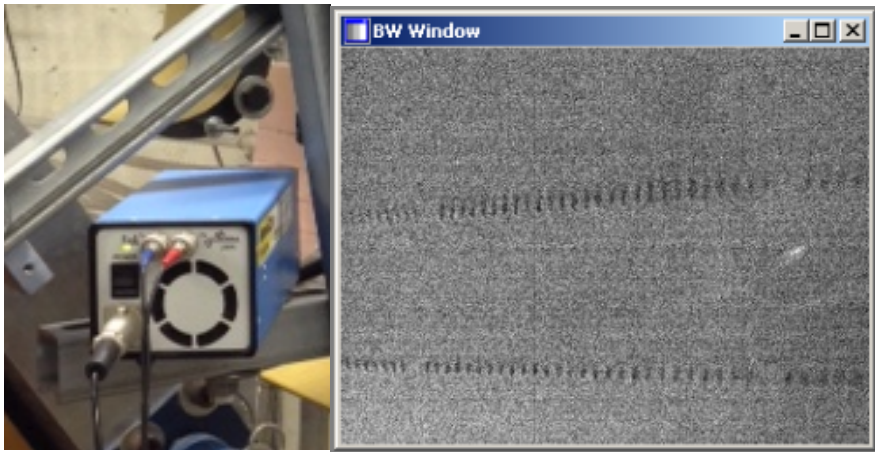

Figure 10-13 The angle at which camera is taking the images (left) which causes the perspective effect seen in the image (right)

regions of the blade as the curvature is significant. To overcome this deficiency, the blade in these regions was divided into very narrow strips. Each thin and narrow strip is then treated as a planar surface, and image rectification is then applied to it. The film-cooling coverage on all strips are later combined to obtain the coverage on the entire span of the blade. Based on the control points that the user has to input to the program, it identifies the parameters needed for spatial transformation needed (scale, rotation, translation, and shear). Then transformation structure is constructed and applied to the image. The following figure shows the same image shown in Figure 10-13 before and after applying the perspective correction.

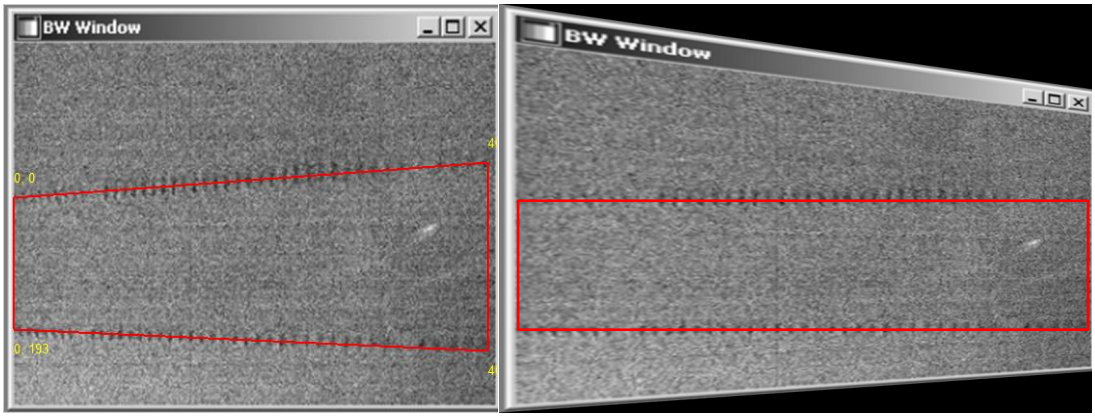

Figure 10-14 Raw image (right) before perspective correction. Rectified image (Left)

11 EXPERIMENTAL FILM-COOLING RESULTS[1]

Film-cooling effectiveness measurements were done at Reynolds number of 150,000 and turbulence intensity of 1.9%. The Reynolds number is calculated based on suction surface length and exit velocity of the cascade test section. This Reynolds number guarantees the presence of a rather large separation region on the suction surface of the blade.

The approximate blowing ratio for film-cooling effectiveness measurements, based on equal mass flux distribution, for all locations on the blade surface, was kept at 1. Coolant flow-rate for each passage was independently controlled by a separate set of valves and rotameters. This blowing ratio was chosen since the mixing losses are minimum in this condition. All experiments were performed in presence and absence of wakes. In unsteady case, the rod velocity was maintained at 7.52 m/s corresponding to Φ=0.8.

The film-cooling effectiveness results from PSP for steady and unsteady cases on pressure and suction surfaces are shown in Figure 11-1. This figure shows the entire span of the blade in the stream-wise direction in unsteady flow (top) and steady flow (bottom) conditions. The aforementioned figure, however, shows only one-half of the blade in the radial direction. The top limit of this contour plot represents the sidewall of the cascade facility, where light source and camera were installed. The bottom axis represents the mid-line of the blade.

[1] Part of the data reported in this chapter is reprinted with permission from" Experimental Investigation of Film-Cooling Effectiveness of a Highly Loaded Turbine Blade Under Steady and Periodic Unsteady Flow Conditions" By A. Nikparto, M.T. Schobeiri, 2017, ASME Journal of Heat Transfer, 139(7), 072201, Copyright 2017 by American Society of Mechanical Engineers.

11.1 Near End-Wall Regions

In this region, close to the sidewall of the facility, the effect of passage vortices is vividly seen on suction surface contours. The passage vortex as described by Sharma and Butler [185] is originated from pressure-side leg horseshoe vortex of the neighboring blade and then becomes passage vortex. It travels in the lateral direction due to the pressure difference between pressure and suction sides of adjacent blades, until the suction side horseshoe vortex wraps itself around the passage vortex. This vortex carries the inlet boundary flow away from the end-wall. The complex nature of the secondary flow in near end-wall regions has a significant impact on film-cooling characteristics of film injection. This flow is strong enough to deviate the cooling jets in near end-wall regions towards the middle section of the blade even-though in this neighborhood, jets have a compound angle of 20^{o}. This region is identified as the region with the least effective film coverage near side-walls of the suction surface in both conditions. Unsteady flow condition causes weaker coverage in this region compared to steady flow condition as it causes more diffusion of coolant into this zone. Unsteady wakes have unfavorable effects on film-cooling effectiveness in near end-wall region, and that is because they can make the passage flow more turbulent [186], which eventually can lead to better mixing of coolant and mainstream air.

11.2 Leading Edge

Effective cooling of this zone is crucial in the performance of a gas turbine engine. This region has the highest heat transfer rate over the entire airfoil [16]. Unsteady wakes have caused a significant drop in film coverage in this region [16]. This finding is in agreement with measurements of Funazaki, et al. [187]. Unsteady wakes can cause the

mainstream flow to penetrate the coolant film into this region, especially since this region is the closest region of all locations on the blade, to the wake generators. This fact will translate into lower film-cooling effectiveness under unsteady condition. In both cases, it is observed that the portion of the coolant that is being transferred downstream along the pressure side is producing better coverage than suction side although the negative pressure gradient on the suction surface should accelerate the flow more in this direction while positive pressure gradient on the other side has the opposite effect. This is due to the effect of curvature that is going to be discussed in the following section.

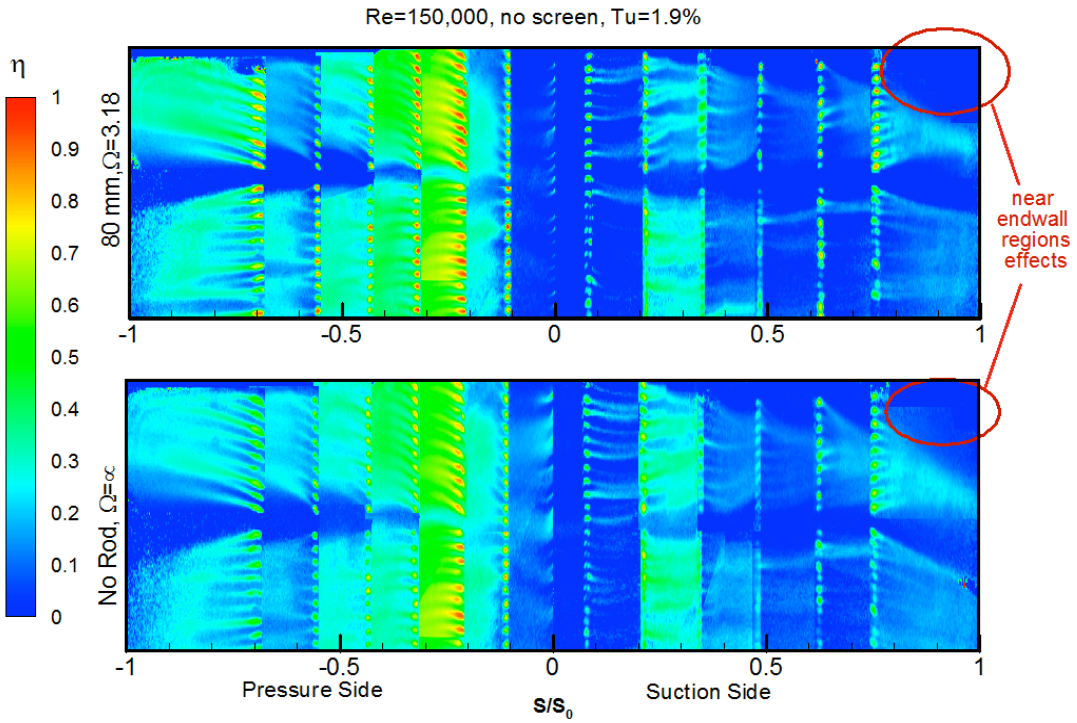

Figure 11-1 Film-Cooling Effectiveness contours of unsteady wake flow condition (top) and steady (bottom) for the entire span of the blade at Turbulence intensity of 1.9% and Ω =3.18 [180]

11.3 Suction Side

Figure 11-2 shows the averaged film-cooling effectiveness in the radial direction for the cooled blade respectively. As seen in this figure, the film-cooling effectiveness on

the suction side is not as strong as the pressure side. There are some reasons that lead to this behavior, and here we intend to identify them. The blade geometry in Figure 10-11 shows that every single channel inside the blade supplies coolant to one row on the suction side and one other row on the pressure surface. Since the static pressure on the suction side is lower than the pressure side, the majority of the coolant has to be directed towards the holes on the suction side. The higher static pressure difference between twin rows will cause more significant blowing ratio difference between twin rows. Even though more coolant is being injected through suction side holes, the overall effectiveness is lower than the identical location on the pressure side. This could be attributed to slightly higher blowing ratio for suction side rows than their respective twin rows on the pressure side. This results in having jets with relatively high momentum coming out of the suction surface. These jets will lift-off and hence we witness a sudden drop in film coverage immediately after injection. Different rows have different angles and having steep angle can increase the tendency to lift-off. Smaller angle can keep jets closer to the surface for a longer time. The peak in film effectiveness on the suction side occurs after the second row. This row has the smallest angle among the first three rows as shown in Figure 10-11. It results in having jets closer to the surface. Also, curvature at this location is slightly lower than the third row. This could increase the possibility of reattachment of the upstream jets as well [188]. This fact along with the ejection angle explains the higher effectiveness in regions downstream from the second row compared to the third row. Although convexedness of suction surface acts against re-attachment, the combined effects of locally lower curvature and smaller ejection angle resulted in locally high film coverage after the second row. Up to almost mid-span of the blade ($S/S_0=0.494$),

boundary layer remains laminar, which is characterized by the lower amount of fluctuation in the lateral direction. Hence boundary layer would not be able to transfer mass, momentum, and energy to blade surface resulting in a drop in HTC from leading edge along the suction surface. On the other hand, the same reason causes the jets to dissipate slower and having slightly higher FCE in regions before $S/S_o=0.494$. The transition is identified by an increase in turbulence level of freestream. An elevated level of velocity fluctuation is observed in transitional regime. In transitional regime, the high level of turbulence will result in having faster and more rapid dissipation of the cooling jets. Table 11-1 lists the static pressure coefficient difference of the two outlets of each passage. Hence at this location, the cooling jets that are being injected from the fourth row on suction side will have the highest blowing ratio and momentum among all jets. Thus they will have considerably higher tendency to lift off from the surface, which results in poor film coverage in the area downstream from this location. This is accompanied by a further reduction of HTC until it assumes the minimum value at the onset of separation ($S/S_o=0.583$). Figure 11-2 clearly shows unsteady wakes have caused a reduction in film effectiveness on this side. Unsteady wakes cause coolant jets to break down faster and hence reduce film coverage. This is seen more vividly in the regions closer to the leading edge.

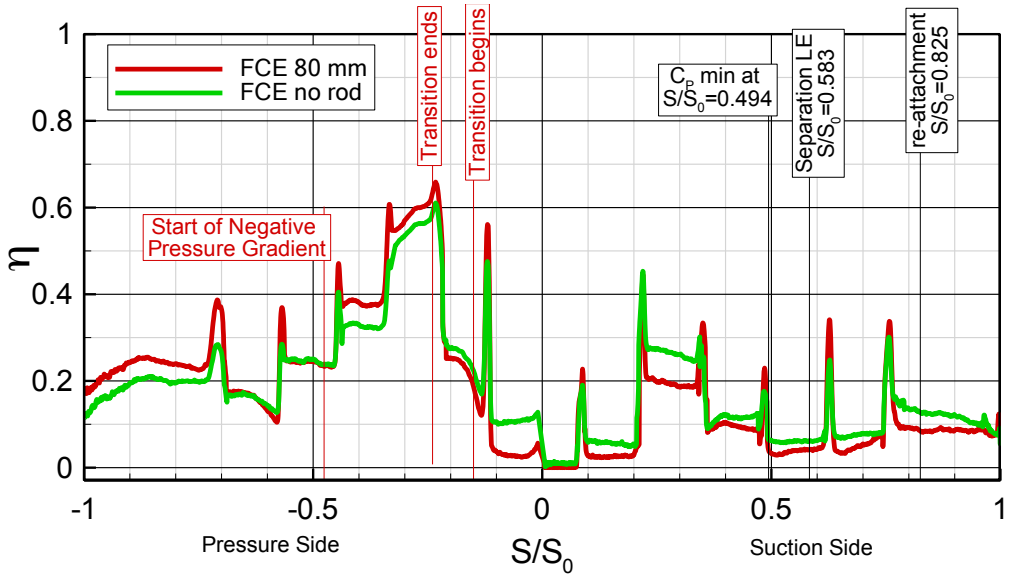

Figure 11-2 Averaged Heat transfer coefficient and film-cooling effectiveness in the radial direction [180]

In zones farther downstream on both sides wakes have to travel significantly longer distance. This fact translates into the smaller difference between film cooling effectiveness of steady and unsteady cases than upstream regions. On suction surface transition starts at an earlier location in the unsteady case compared to steady flow condition since incoming wakes increase the level of turbulence in the boundary layer. This fact is reported by Schobeiri, et al. [67]. It leads to having the separation and reattachment at slightly earlier locations. Film injection also increases local turbulence in boundary layer as well. Thus there will be even higher tendency to have earlier transition, separation and finally re-attachments in a film-cooled blade, which add to the reasons behind having less film-cooling effectiveness in unsteady case.

Table 11-1 Difference between static pressure coefficient of the two outlets of each passage

	Hole 1	Hole 2	Hole 3	Hole 4	Hole 5	Hole 6
ΔC_P	2.17	4.38	6.18	6.66	5.93	4.32

11.4 Pressure Side

For the same reasons explained in the previous section, the blowing ratio for each row on the pressure side is lower than their respective rows on the suction side. Although static pressure forces acting on jets try to move jets away from the surface, the film coverage is generally higher on this side than the suction surface of the blade. The concavity of the blade not only results in having jets with smaller angles but also acts in favor of re-attachment. This effect is clearly seen immediately downstream from the second row. This row is located where the curvature of the surface is maximum.

As stated earlier unsteady wakes cause earlier transition on both surfaces. On the pressure side transition occurs at a location which is $\Delta S/S_o=0.064$ closer to leading edge compared to steady flow. Subsequently, transition ends sooner as well resulting in a noticeable change in HTC distribution. Regarding FCE, unsteady wakes have the opposite effect on pressure side as they had on the suction surface except for the small region immediately downstream from the leading edge. At this location, where the boundary layer is laminar and also it is the closest location to wake generators, unsteady wakes produce an increased turbulence level which helps to dissipate the jets faster.

In locations downstream from this point, unsteady wakes have increased film effectiveness. It is obvious in Figure 11-1 that the jets are thicker in unsteady flow condition compared to steady flow. The concavity of the surface and low injection angle along with Blowing ratio of less than one, due to static pressure difference at the jet outlets of a single coolant passage, prevent jets from lifting off from the surface while higher lateral fluctuations in unsteady case cause diffusion of wakes in the radial

direction. Hence an increase in the radial average of film-cooling effectiveness is observed.

Farther downstream regions receive less coolant as the pressure difference between the identical rows on the suction and pressure surfaces increases. Also, curvature tends to decrease until it is not effective enough to overcome the effect of positive pressure gradient of the mainstream flow. The positive pressure gradient at these locations prevents re-attachment of the jets once they have lifted off from the surface. In this zone, which film coverage is minimum of all places on the pressure side (except for the leading edge), the difference between steady and unsteady cases drops to zero that stresses out the strength of positive pressure gradient in dissipating jets into the mainstream. Downstream from the last cooling row is the region where the curvature is not present anymore, and the smaller angles of jets would help them to remain on the surface and subsequently results in having an increase in film coverage. Again in this area, unsteady wakes have a positive effect on film-cooling effectiveness due to the same reason explained before[51].

12 NUMERICAL SIMULATION OF FILM-COOLING

This chapter[1] is dedicated to numerical simulation of the film-cooling effectiveness of a highly-loaded low-pressure turbine blade in a linear subsonic cascade facility. The following contains details about numerical simulation, grid generation and numerical results.

12.1 Numerical Simulations

Three-dimensional simulations are performed for steady (RANS) and unsteady (URANS) cases for the linear low-pressure turbine blade cascade facility using a commercial RANS-based solver, ANSYS CFX v17.1. The geometric information was taken from the cascade facility. Realistic boundary conditions were set for the computational model to be a good representation of the working condition in the cascade facility.

The model consists of two domains. The domain that contains the moving rods, is moving and the one containing the blades, is stationary. Movements of the rods produce unsteady wakes that impinge on the blade surfaces. As mentioned in the previous chapter, the mass flow-rate of the coolant in experiments was set based on the assumption of equal mass flow distribution, and the same values were prescribed at the inlets of the cooling passages.

A total of 6 simulations were done for both steady and unsteady cases. They were done in the exact same manner that experimental data were collected. In each simulation, the coolant is fed only to two of the adjacent passages and the area of focus was only the

[1] Part of the data reported in this chapter is reprinted with permission from" Experimental and Numerical Investigation of Heat Transfer and Film-Cooling Effectiveness of a Highly Loaded Turbine Blade Under Steady and Unsteady Wake Flow Condition" By A. Nikparto, T. Rice and M.T. Schobeiri, 2017, Paper No. GT2017-65012 , Copyright 2017 by American Society of Mechanical Engineers.

area downstream of the second coolant injection row. Each transient simulation was done for 1.5 seconds with the time-step of 0.01 seconds. For computational efficiency, only half of the blade was considered in the model by applying symmetry boundary condition. This is a valid approach since both the blade and the flow condition are symmetrical.

12.1.1 Mesh Generation

The cooled blade has 617 holes distributed along 13 rows on both surfaces and the leading edge. The huge number of holes on the surfaces makes it practically impossible to use structured grid. Hence, an unstructured grid was generated using ANSYS Meshing Software. This mesh consists of hybrid tetrahedral elements throughout the 3D geometry with a total of 15.5 million elements. In the region near blade surfaces, finer elements were introduced to ensure a y^+ value under 1. A grid independency test was performed to ensure the reliability of the results. Figure 12-1 shows the produced unstructured grid.

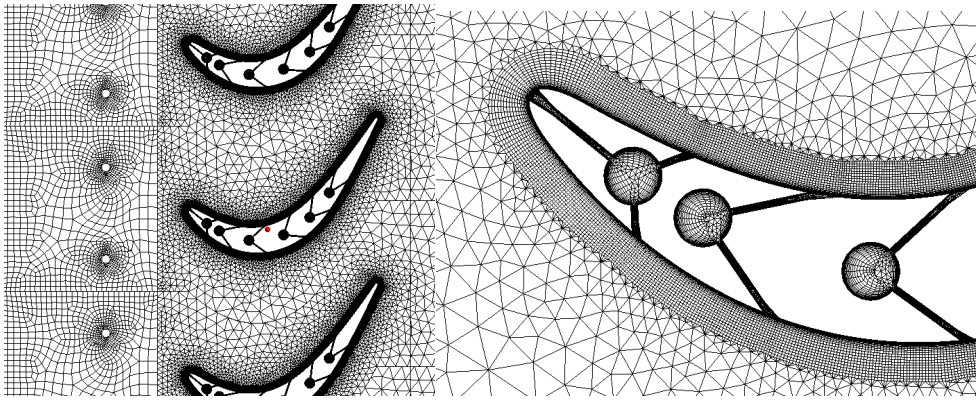

Figure 12-1 The computational domain created using ANSYS Meshing [189]

12.1.2 Boundary Conditions

Uniform velocity is prescribed at the inlet of the moving domain and the magnitude of velocity is set for Reynolds number of 150,000. The pressure at the outlet of the stationary domain is zero.

The boundaries at the top and bottom of both computational domains are periodic and mass flow rate of the coolant is prescribed at the inlet of the passages that supply coolant to the cooling holes on blade surfaces. This mass flow corresponds to blowing ratio of one based on equal mass distribution assumption. Smooth wall and symmetry boundary conditions were prescribed for the end-wall of the cascade and the (blade)model mid-section respectively. The linear velocity of the moving domain is defined based on flow coefficient of 0.8.

12.1.3 Turbulence Models

Variety of turbulence models are recommended and used in film-cooling simulations. In this particular study, the flow is of transitional nature, and as the boundary layer develops, it faces laminar separation, and re-attachment while the constant injection of the coolants continuously disrupts the boundary layer. For this complex flow, Shear Stress Transport Scale-Adaptive Simulation (SST SAS) is used. This is a RANS model and combines the advantages of k-ε and k-ω. It uses k-ω in the regions close to the wall and switched to k-ε in farther regions. To capture the transitional effects of the flow, a correlation based transitional model (transitional SST) introduced by Menter, et al. [43], is commonly used in commercial CFD solvers. This model is also known as the γ-Reθ Model and it incorporates a transport equation of intermittency factor and couples it with the SST Turbulence model by influencing the production term in turbulent kinetic energy.

The Scale-Adaptive Simulation is a modified formulation of the URANS equation. It reportedly performs superior because of the von Karman length-scale that is introduced into the source term in the transport equation for the turbulence eddy frequency. This model is developed by Menter and Egorov [190] and provides better mixing between two different streams, which is the case in film-cooling applications.

In these simulations, it is assumed that the flow is incompressible. The convection term was discretized using high-resolution scheme and for the temporal term, second order backward Euler scheme has been used.

12.2 Numerical Simulation Results

Figure 12-2 shows laterally averaged film-cooling effectiveness measurements along with CFD predictions on the surfaces of the blade. At some locations, the difference between measurements and predictions might reach 100%. A reason for the overprediction of film cooling effectiveness in the CFD calculations could be contributed to the under-prediction of turbulent lateral diffusion that is an issue in CFD models [191]. An isotropic turbulence model is used to calculate the lateral diffusion of the film cooling jets. This inaccuracy in lateral diffusion in simulations will under-predict the decay in effectiveness, specifically in diffused holes, as seen in this study**.** This discrepancy has also been a subject in recent investigations reported in Ref [191] and Ref [192].

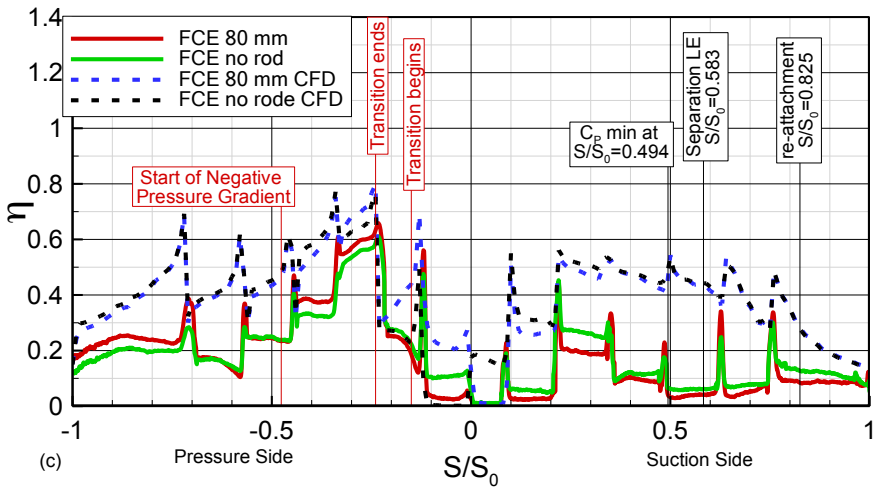

Figure 12-2 laterally averaged film cooling effectiveness obtained by PSP method (solid lines) and through CFD (dashed lines) [189]

The Laterally Averaged film-cooling effectiveness trend can be accurately predicted with the CFD across the blade except in the transitional region on the pressure surface, $S/S_o = 0.15$ to $S/S_0 = 0.24$. In this region, the film-cooling effectiveness slowly increases downstream while in the computational model the film cooling effectiveness rapidly decreases downstream. This discrepancy can be accounted to the high surface concavity in this region. This concavity can inaccurately predict the surface properties in transitional regions.

Figure 12-2 is blind to the three-dimensional effects that cause film coverage to vary in lateral direction. For this reason, Figure 12-3 is presented and investigated. Considering the distribution of film-cooling effectiveness in the lateral direction the distribution of laterally averaged FCE also can better be justified.

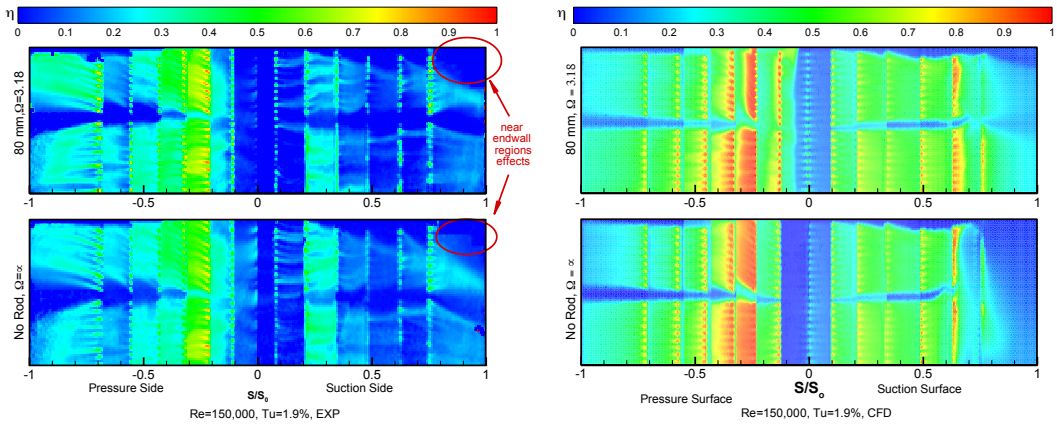

Figure 12-3 film cooling effectiveness contour plots obtained through experiments (left) and numerical simulation (right) for steady state condition (top) and unsteady wake induced flow (bottom) [189]

This figure shows the entire span of the blade in the stream-wise direction in unsteady flow (top figures) and steady flow (bottom figures) condition. However, the figure above shows only one-half of the blade in the radial direction. The top limit in this contour plot represents the sidewall of the cascade facility, where light source and camera were installed. The bottom axis represents the mid-line of the blade.

12.2.1 Near End-Wall Regions

This region is identified as the region with least effective film coverage near the side-walls of the suction surface in both conditions. Unsteady flow conditions cause stronger coverage in this region compared to steady flow condition as it causes more diffusion of coolant into this zone. It is seen in the simulation that the horseshoe and passage vortex formation approaching the trailing edge is not as strong as the experiment case. This fact is also confirmed by Ingram, et al. [193]. The turbulence length scale in CFD code is oversensitive to the free stream turbulence. A modified turbulent mixing length scale for the free stream and a less active turbulent viscosity in the CFD model can more accurately predict the physics.

12.2.2 Leading Edge

This region has the highest heat transfer coefficient and subsequently a very significant thermal load. For that reason, it is very prone to thermal damage. As stated in the previous chapter, since this location is the closest to wake generators, the effect of unsteady incoming wakes are more obvious in this region than all other locations. It can be observed in the computational model that at the leading edge, the pressure surface film-cooling effectiveness has a high sensitivity to the upstream wakes. It can be seen that the unsteady wakes significantly increase the effectiveness in this region. This differs from the experimental findings. The film-cooling effectiveness increase on the pressure side in the unsteady case is contributed to the stagnation turbulent kinetic energy [194]. The effect is going to enhance the film cooling effectiveness when the lateral dissipation is not correctly accounted for, which is observed in many other instances. The primary vortex that occurs in this region is going to in turn displace the coolant on the pressure surface of the film-cooling hole.

12.2.3 Suction Side

Figure 12-2 and Figure 12-3 show that film-cooling effectiveness on the suction side is not as strong as pressure side. There are a number of reasons that lead to this behavior, and here we intend to identify those reasons. The uneven distribution of coolant between twin rows results in having jets with relatively high momentum coming out of the suction surface. These jets will tend to lift off, and hence we witness a sudden drop in film coverage in the locations immediately after injection. The CFD model tends to overestimate the jet's wall attachment downstream of the cooling holes. This overestimation is the reason for a slow dissipation of the thermal energy downstream of

the wall. Kampe and Völker [195] contribute this to the difference in jet-to-coolant ratios between the simulation and experiment thus affecting the jet momentum. This, in turn, causes the jet to remain attached to the wall and can contribute to higher effectiveness.

According to experimental results, the most effective film-coverage on suction side corresponds to the region downstream of the second row. This row has the smallest ejection angle among the first three rows. It results in having jets closer to the surface. Also, curvature at this location is a slightly lower than the third row. This could increase the possibility of reattachment of the upstream jets as well [188]. This fact along with the ejection angle can explain the higher effectiveness in regions downstream from the second row compared to the third row. According to Berhe and Patankar [196], one of the effects of streamline curvature is to alter near-wall shear stresses. For that reason, on convex surfaces the shear stress is damped thus at the location with higher curvature on the suction side, the shear stress decreases which in turn decreases the film-cooling effectiveness in the computational model.

Figure 12-2 and Figure 12-3 show that unsteady wakes have negative effects on film-cooling effectiveness on this side. Unsteady wakes cause coolant jets to break down faster and allow mainstream to penetrate the coolant film more easily. In zones farther downstream on both sides, wakes have to travel significantly longer distances. This fact translates into smaller difference between the measured film-cooling effectiveness of steady and unsteady cases than upstream regions. This is opposite of the trend observed in computational model where the difference between steady and unsteady cases keep increasing as we move downstream. The lateral diffusion of the coolant is inaccurate in this model. This lack of prediction in conjunction with incorrect turbulent length scale

allows the wakes to have more significant impact farther downstream in simulated results compared to experimental results.

12.2.4 Pressure Side

For the same reasons explained in the previous section and chapter regarding the difference between surface pressures at the outlets of each passage, the blowing ratio of rows on pressure side is lower than their respective rows on the suction side.

Unsteady wakes have the opposite effects on the film-cooling effectiveness on the pressure side as they had on the suction surface except for a small region in the immediate neighborhood of the leading edge. At this location, where the boundary layer is laminar and also it is the closest location to wake generators, unsteady wakes cause an increased turbulence level which helps to dissipate the jets faster. The CFD model captures this trend incorrectly on the pressure surface because the diffusion of the coolant is inaccurately assumed. Modifications to the turbulent diffusion of the jet need to be put in place in the simulation. Farther downstream regions receive less coolant because of the pressure difference between twin rows of the same passage and the effect of curvature also decreases until it is not effective enough to overcome the effect of the positive pressure gradient of the mainstream flow. The positive pressure gradient hinders re-attachment of the coolant jets once they have lifted off. In this zone, the difference between steady and unsteady cases drops to zero. This stresses out the strength of positive pressure gradient in dissipating jets into the mainstream. CFD results at this location, unlike the suction surface, show very similar results for film-cooling effectiveness between the steady and unsteady case which is because of lack of flow complexities that are observed on the suction side such as change in the sign of pressure gradient and flow

separation. Also, the effect of stagnation turbulent kinetic energy that had caused a large difference between steady and unsteady cases in the leading edge area, is no longer present in this area.

Downstream from the last cooling row is the region where curvature is not a defining parameter anymore and injection angles are smaller. This allows the jets to remain close to the surface and have better film-coverage. CFD, on the other hand, shows a decline in film effectiveness.

12.2.5 Flow Separation

This part of the study deals with the investigation of interactions of cooling jets and the separation bubble. Incoming coolant jets have two inherent effects on the flow field. It acts as flow disturbance and also can displace the main flow [197]. For that reason, the location of the injection becomes an important parameter regarding occurrence of the bubble. In the current configuration, rows five and six on the suction side of the blade inject coolants into the separation zone. Deinert and Hourmouziadis [197] have reported that injection of coolant at an upstream location of the separation point can suppress and prevent the separation bubble. However, if the coolant is injected at some location downstream from the separation onset, the bubble still develops.

Figure 12-4 shows the separation bubble on the suction surface of this blade. In this figure, velocity magnitude contour plot for the cooled blade is shown.

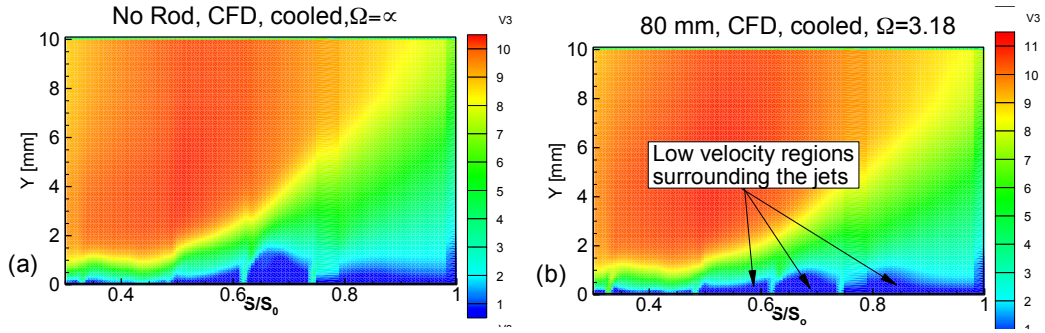

Figure 12-4 Flow separation on the suction surface of the blade. (a) steady and (b) unsteady [189]

The last two injection rows that are seen in Figure 12-4(a) and (b) are discharging coolant into a zone with positive pressure gradient. This fact, along with the injection angle has apparently caused a major lift-off from the surface. The low-velocity region seen in the these figures upstream from the fifth injection hole is primarily due to the separation bubble, which still exists despite the coolant injection from the fourth row. The wake that occurs behind the cooling jets [198](and not the kind of wake that originates from rods), has also suppressed this recirculation zone and as we observe, this region has decreased in size and extent.

The same explanation applies to the low-velocity region surrounding the last cooling jet. The coolant injected from the suction surface rows has promoted separation regions to the extent that has prevented the flow from reattaching to the surface. This fact can for sure impact the C_P distribution as well. As unsteady incoming wakes are introduced into the system, the separation bubble is suppressed by facilitating more mass, momentum and energy exchange between the boundary layer and the mainstream.

13 CONCLUSION

Higher efficiencies are achieved in gas turbine engines by increasing the turbine inlet temperature. This increase although is beneficial in-terms of thermal efficiency, has a drawback. Higher working temperature translates into elevated thermal loads on engine elements and more pronounced maintenance costs. To reduce and prevent that, cooling technologies have to be put in place to protect surfaces of engine components from hot gas. This study investigates the film-cooling effectiveness of a highly loaded turbine blade under steady and unsteady flow conditions. The same blade was investigated before thoroughly from aerodynamics and heat transfer perspective and is now considered for film-cooling effectiveness study.

After performing experimental measurements and numerical simulations, the following observations are made:

5. Film-cooling effectiveness on pressure side is stronger than the suction surface. This kind of behavior is attributed to larger blowing ratio for the jets on the suction surface, concavity and convexedness of pressure and suction side which act respectively in favor and against re-attachment of cooling jets as well as larger ejection angle for the rows on the suction side.
6. CFD consistently over-predicts film-cooling effectiveness on both surfaces of the blade. This behavior could be attributed to incorrect prediction of lateral diffusion in simulations. This fact will under-predict the decay in effectiveness. For that reason, FCE maintains higher value in CFD simulations, although the trend is almost correctly captured. The only location that the CFD solver fails to predict the trend correctly, is the transitional region.

7. The trend of laterally averaged effectiveness can be correctly captured by CFD across the blade except for the transitional region. This discrepancy can be due to the high surface concavity. This concavity can inaccurately predict the heat transfer properties in the transitional region.
8. Film-cooling could displace the mainstream flow. Also, they could potentially produce disturbances, which could result in enormous effects on flow separation. Coolant discharge, upstream of separation bubble, could potentially suppress the separation. In this case, despite the fact that there are upstream coolant injections, flow separation is still present. The last two injections, located inside the bubble, promote flow separation and act against re-attachment.
9. Heat transfer coefficient and film-cooling effectiveness, for the most part, act against one another. This is justified form velocity fluctuation point of view. Higher velocity fluctuation cause higher rate of momentum and energy transfer between the flow and boundary layer. For the same reason, in turbulent boundary layer, mainstream can penetrate easier to the boundary layer and reduce the effect of coolant injections.
10. Unsteady wakes show opposite effects on suction and pressure sides. On the suction surface unsteady wakes have unfavorable effect on FCE. This is attributed to faster break down and dissipation of jets into mainstream in unsteady case. Inside the transitional and eventually separation region, the difference between FCE in steady and unsteady conditions becomes less apparent. CFD however shows completely different trends. Unsteady wakes have consistently increased film-cooling effectiveness. This is again due to higher mixing of the coolant with

mainstream air than reality which is because of incorrect lateral fluctuation and unrealistic turbulent length scale.

REFERENCES

[1] P. Chakka and M. Schobeiri, "Modeling unsteady boundary layer transition on a curved plate under periodic unsteady flow conditions: Aerodynamic and heat transfer investigations," *Journal of turbomachinery,* vol. 121, no. 1, pp. 88-97, 1999.

[2] M. T. Schobeiri and P. Chakka, "Prediction of turbine blade heat transfer and aerodynamics using a new unsteady boundary layer transition model," *International Journal of Heat and Mass Transfer,* vol. 45, no. 4, pp. 815-829, 2002.

[3] S. A. E. Outlook, "World energy outlook special report," *France International Energy Agency (IEA),* 2013.

[4] N. Davey, *The Gas Turbine – Development and Engineering*. Watchmaker Publishing, 2003.

[5] R. J. Hunt, "The History of the Industrial Gas Turbine (Part 1 The First Fifty Years 1940–1990)," ed, 1990.

[6] F. Haselbach, H.-P. Schiffer, M. Horsman, S. Dressen, N. Harvey, and S. Read, "The application of ultra high lift blading in the BR715 LP turbine," in *ASME Turbo Expo 2001: Power for Land, Sea, and Air*, 2001, pp. V001T03A058-V001T03A058: American Society of Mechanical Engineers.

[7] R. Sondergaard, J. P. Bons, M. Sucher, and R. B. Rivir, "Reducing low-pressure turbine stage blade count using vortex generator jet separation control," in *ASME Turbo Expo 2002: Power for Land, Sea, and Air*, 2002, pp. 1055-1061: American Society of Mechanical Engineers.

[8] H. Pfeil and R. Herbst, "Transition procedure of instationary boundary layers," in *ASME 1979 International Gas Turbine Conference and Exhibit and Solar Energy Conference*, 1979, pp. V01BT02A027-V01BT02A027: American Society of Mechanical Engineers.

[9] H. Pfeil, R. Herbst, and T. Schröder, "Investigation of the laminar-turbulent transition of boundary layers disturbed by wakes," in *ASME 1982 International Gas Turbine Conference and Exhibit*, 1982, pp. V001T01A050-V001T01A050: American Society of Mechanical Engineers.

[10] U. Orth, "Unsteady boundary-layer transition in flow periodically disturbed by wakes," in *ASME 1992 International Gas Turbine and Aeroengine Congress and Exposition*, 1992, pp. V001T01A093-V001T01A093: American Society of Mechanical Engineers.

[11] M. T. Schobeiri and R. Radke, "Effects of Periodic Unsteady Wake Flow and Pressure Gradient on Boundary Layer Transition Along the Concave Surface of a Curved Plate," presented at the ASME 1994 International Gas Turbine and Aeroengine Congress and Exposition, The Hague, Netherlands, 1994.

[12] M. T. Schobeiri and K. Pappu, "Experimental study on the effect of unsteadiness on boundary layer development on a linear turbine cascade," *Experiments in Fluids,* vol. 23, no. 4, pp. 306-316, 1997.

[13] P. Stadtmüller and L. Fottner, "A test case for the numerical investigation of wake passing effects on a highly loaded LP turbine cascade blade," in *ASME Turbo Expo 2001: Power for Land, Sea, and Air*, 2001, pp. V001T03A015-V001T03A015: American Society of Mechanical Engineers.

[14] I. Popovic, J. Zhu, W. Dai, S. Sjolander, T. Praisner, and E. Grover, "Aerodynamics of a Family of Three Highly Loaded Low-Pressure Turbine Airfoils: Measured Effects of Reynolds Number and Turbulence Intensity in Steady Flow," in *ASME Turbo Expo 2006: Power for Land, Sea, and Air*, 2006, pp. 961-969: American Society of Mechanical Engineers.

[15] M. T. Schobeiri, B. Öztürk, and D. E. Ashpis, "Effect of Reynolds Number and Periodic Unsteady Wake Flow Condition on Boundary Layer Development, Separation, and Intermittency Behavior Along the Suction Surface of a Low Pressure Turbine Blade," *Journal of Turbomachinery,* vol. 129, no. 1, pp. 92-107, 2005.

[16] M. T. Schobeiri, B. Öztürk, and D. E. Ashpis, "Effect of reynolds number and periodic unsteady wake flow condition on boundary layer development, separation, and intermittency behavior along the suction surface of a low pressure turbine blade," *Journal of Turbomachinery,* vol. 129, no. 1, pp. 92-107, 2007.

[17] A. Mahallati and S. A. Sjolander, "Aerodynamics of a Low-Pressure Turbine Airfoil at Low Reynolds Numbers—Part II: Blade-Wake Interaction," *Journal of Turbomachinery,* vol. 135, no. 1, pp. 011011-011011, 2013.

[18] A. Mahallati, B. R. McAuliffe, S. A. Sjolander, and T. J. Praisner, "Aerodynamics of a Low-Pressure Turbine Airfoil at Low Reynolds Numbers—Part I: Steady Flow Measurements," *Journal of Turbomachinery,* vol. 135, no. 1, p. 011010, 2013.

[19] Y. Liang, Z.-P. Zou, H.-X. Liu, and W.-H. Zhang, "Experimental investigation on the effects of wake passing frequency on boundary layer transition in high-lift low-pressure turbines," *Experiments in Fluids,* vol. 56, no. 4, pp. 1-13, 2015.

[20] D. E. Halstead, D. C. Wisler, T. H. Okiishi, G. J. Walker, H. P. Hodson, and H. W. Shin, "Boundary Layer Development in Axial Compressors and Turbines: Part 1 of 4—Composite Picture," *Journal of turbomachinery,* vol. 119, no. 1, pp. 114-127, 1997.

[21] D. E. Halstead, D. C. Wisler, T. H. Okiishi, G. J. Walker, H. P. Hodson, and H. W. Shin, "Boundary Layer Development in Axial Compressors and Turbines: Part 2 of 4—Compressors," *Journal of turbomachinery,* vol. 119, no. 3, pp. 426-444, 1997.

[22] D. E. Halstead, D. C. Wisler, T. H. Okiishi, G. J. Walker, H. P. Hodson, and H. W. Shin, "Boundary Layer Development in Axial Compressors and Turbines: Part 3 of 4—LP Turbines," *Journal of turbomachinery,* vol. 119, no. 2, pp. 225-237, 1997.

[23] D. E. Halstead, D. C. Wisler, T. H. Okiishi, G. J. Walker, H. P. Hodson, and H. W. Shin, "Boundary Layer Development in Axial Compressors and Turbines: Part 4 of 4—Computations and Analyses," *Journal of turbomachinery,* vol. 119, no. 1, pp. 128-139, 1997.

[24] W. Lou and J. Hourmouziadis, "Separation bubbles under steady and periodic-unsteady main flow conditions," *Journal of Turbomachinery,* vol. 122, no. 4, pp. 634-643, 2000.

[25] M. Talan and J. Hourmouziadis, "Characteristic regimes of transitional separation bubbles in unsteady flow," *Flow, turbulence and combustion,* vol. 69, no. 3-4, pp. 207-227, 2002.

[26] J. P. Gostelow and R. L. Thomas, "Interactions between propagating wakes and flow instabilities in the presence of a laminar separation bubble," in *ASME Turbo Expo 2006: Power for Land, Sea, and Air*, 2006, pp. 1261-1269: American Society of Mechanical Engineers.

[27] J. Dähnert, C. Lyko, and D. Peitsch, "Transition Mechanisms in Laminar Separated Flow Under Simulated Low Pressure Turbine Aerofoil Conditions," *Journal of Turbomachinery,* vol. 135, no. 1, p. 011007, 2013.

[28] X. Liu and W. Rodi, "Experiments on transitional boundary layers with wake-induced unsteadiness," *Journal of Fluid Mechanics,* vol. 231, pp. 229-256, 1991.

[29] R. W. Kaszeta, T. W. Simon, and D. E. Ashpis, "Experimental investigation of transition to turbulence as affected by passing wakes," in *ASME Turbo Expo 2001: Power for Land, Sea, and Air*, 2001, pp. V003T01A069-V003T01A069: American Society of Mechanical Engineers.

[30] B. Öztürk, M. Schobeiri, and D. E. Ashpis, "Intermittent Behavior of the Separated Boundary Layer along the Suction Surface of a Low Pressure Turbine Blade under Periodic Unsteady Flow Conditions," in *ASME Turbo Expo: Power for Land, Sea, and Air*, 2005: ASME.

[31] B. Öztürk and M. Schobeiri, "Effect of turbulence intensity and periodic unsteady wake flow condition on boundary layer development, separation, and

reattachment along the suction surface of a low-pressure turbine blade," *Journal of fluids engineering,* vol. 129, no. 6, pp. 747-763, 2007.

[32] V. Michelassi, J. Wissink, and W. Rodi, "DNS, LES and URANS of periodic unsteady flow in a LP turbine cascade: a comparison," in *Proceedings 5th European Conference on Turbomachinery: Fluid Dynamics and Thermodynamics, Prague*, 2003.

[33] J. Wissink, "DNS of separating, low Reynolds number flow in a turbine cascade with incoming wakes," *International journal of heat and fluid flow,* vol. 24, no. 4, pp. 626-635, 2003.

[34] W. Höhn and K. Heinig, "Numerical and Experimental Investigation of Unsteady Flow Interaction in a Low-Pressure Multistage Turbine," *Journal of Turbomachinery,* vol. 122, no. 4, pp. 628-633, 2000.

[35] R. Meyer, "The effect of wakes on the transient pressure and velocity distributions in turbomachines," *Trans. ASME,* vol. 80, no. 7, pp. 1544-1552, 1958.

[36] M. Lefcort, "An investigation into unsteady blade forces in turbomachines," *Journal of Engineering for Gas Turbines and Power,* vol. 87, no. 4, pp. 345-354, 1965.

[37] J. R. Cho and M. K. Chung, "AK—ε—γ equation turbulence model," *Journal of Fluid Mechanics,* vol. 237, pp. 301-322, 1992.

[38] J. Steelant and E. Dick, "Modelling of bypass transition with conditioned Navier–Stokes equations coupled to an intermittency transport equation," *International journal for numerical methods in fluids,* vol. 23, no. 3, pp. 193-220, 1996.

[39] S. Dhawan and R. Narasimha, "Some properties of boundary layer flow during the transition from laminar to turbulent motion," *Journal of Fluid Mechanics,* vol. 3, no. 04, pp. 418-436, 1958.

[40] Y. B. Suzen and P. G. Huang, "Modeling of Flow Transition Using an Intermittency Transport Equation," *Journal of Fluids Engineering,* vol. 122, no. 2, pp. 273-284, 2000.

[41] Y. Suzen and P. Huang, "Numerical simulation of unsteady wake/blade interactions in low-pressure turbine flows using an intermittency transport equation," *Journal of turbomachinery,* vol. 127, no. 3, pp. 431-444, 2005.

[42] F. R. Menter, "Two-equation eddy-viscosity turbulence models for engineering applications," *AIAA journal,* vol. 32, no. 8, pp. 1598-1605, 1994.

[43] F. Menter, R. Langtry, S. Likki, Y. Suzen, P. Huang, and S. Völker, "A correlation-based transition model using local variables—Part I: model formulation," *Journal of turbomachinery,* vol. 128, no. 3, pp. 413-422, 2006.

[44] R. B. Langtry, F. Menter, S. Likki, Y. Suzen, P. Huang, and S. Völker, "A correlation-based transition model using local variables—Part II: Test cases and industrial applications," *Journal of Turbomachinery,* vol. 128, no. 3, pp. 423-434, 2006.

[45] J. Steelant and E. Dick, "Modeling of laminar-turbulent transition for high freestream turbulence," *Journal of Fluids Engineering,* vol. 123, no. 1, pp. 22-30, 2001.

[46] F. Menter, M. Kuntz, and R. Langtry, "Ten years of industrial experience with the SST turbulence model," *Turbulence, heat and mass transfer,* vol. 4, pp. 625-632, 2003.

[47] R. Langtry and F. Menter, "Transition modeling for general CFD applications in aeronautics," *AIAA paper,* vol. 522, p. 2005, 2005.

[48] K. Lodefier, B. Merci, C. De Langhe, and E. Dick, "Transition modelling with the k-Ω turbulence model and an intermittency transport equation," *Journal of Thermal Science,* vol. 13, no. 3, pp. 220-225, 2004.

[49] P. Durbin, "An intermittency model for bypass transition," *International Journal of Heat and Fluid Flow,* vol. 36, pp. 1-6, 2012.

[50] X. Ge, S. Arolla, and P. Durbin, "A bypass transition model based on the intermittency function," *Flow, turbulence and combustion,* vol. 93, no. 1, pp. 37-61, 2014.

[51] A. Nikparto and M. T. Schobeiri, "Investigation of Aerodynamics and Heat Transfer of a Highly Loaded Turbine Blade Using the Universal Intermittency Function," in *ASME Turbo Expo 2017: Turbomachinery Technical Conference and Exposition*, 2017, pp. V02DT46A030-V02DT46A030: American Society of Mechanical Engineers.

[52] J. G. Wissink and W. Rodi, "Direct numerical simulation of flow and heat transfer in a turbine cascade with incoming wakes," *Journal of Fluid Mechanics,* vol. 569, pp. 209-247, 2006.

[53] W. Rodi, "DNS and LES of some engineering flows," *Fluid Dynamics Research,* vol. 38, no. 2, pp. 145-173, 2006.

[54] T. Praisner and J. Clark, "Predicting transition in turbomachinery—Part I: A review and new model development," *Journal of Turbomachinery,* vol. 129, no. 1, pp. 1-13, 2007.

[55] S. Sarkar, "Influence of wake structure on unsteady flow in a low pressure turbine blade passage," *Journal of turbomachinery,* vol. 131, no. 4, p. 041016, 2009.

[56] S. Jagannathan, M. Schwänen, and A. Duggleby, "Low Pressure Turbine Relaminarization Bubble Characterization using Massively-Parallel Large Eddy Simulations," *Journal of Fluids Engineering,* vol. 134, no. 2, p. 021102, 2012.

[57] M. B. Ibrahim, S. Vinci, O. Kartuzova, and R. J. Volino, "CFD Simulations of Unsteady Wakes on a Highly Loaded Low Pressure Turbine Airfoil (L1A)," in *ASME Turbo Expo 2012: Turbine Technical Conference and Exposition*, 2012, pp. 843-856: American Society of Mechanical Engineers.

[58] R. Ciorciari, I. Kirik, and R. Niehuis, "Effects of Unsteady Wakes on the Secondary Flows in the Linear T106 Turbine Cascade," *Journal of Turbomachinery,* vol. 136, no. 9, p. 091010, 2014.

[59] M. T. Schobeiri and A. Nikparto, "A Comparative Numerical Study of Aerodynamics and Heat Transfer on Transitional Flow Around a Highly Loaded Turbine Blade with Flow Separation Using RANS, URANS and LES," in *ASME Turbo Expo 2014: Turbine Technical Conference and Exposition*, 2014, pp. V05CT17A001-V05CT17A001: American Society of Mechanical Engineers.

[60] J. C. Han, L. Zhang, and S. Ou, "Influence of unsteady wake on heat transfer coefficient from a gas turbine blade," *Journal of heat transfer,* vol. 115, no. 4, pp. 904-911, 1993.

[61] K. Dullenkopf and R. E. Mayle, "The effects of incident turbulence and moving wakes on laminar heat transfer in gas turbines," *Journal of turbomachinery,* vol. 116, no. 1, pp. 23-28, 1994.

[62] P. J. Magari and L. E. LaGraff, "Wake-induced unsteady stagnation-region heat transfer measurements," *Journal of turbomachinery,* vol. 116, no. 1, pp. 29-38, 1994.

[63] P. W. Giel, G. J. Van Fossen, R. J. Boyle, D. R. Thurman, and K. C. Civinskas, "Blade heat transfer measurements and predictions in a transonic turbine cascade," in *ASME 1999 International Gas Turbine and Aeroengine Congress and Exhibition*, 1999, pp. V003T01A029-V003T01A029: American Society of Mechanical Engineers.

[64] P. W. Giel, R. J. Boyle, and R. S. Bunker, "Measurements and predictions of heat transfer on rotor blades in a transonic turbine cascade," *Transactions of the ASME-T-Journal of Turbomachinery,* vol. 126, no. 1, pp. 110-121, 2004.

[65] J. A. Tallman, C. W. Haldeman, M. G. Dunn, A. K. Tolpadi, and R. F. Bergholz, "Heat Transfer Measurements and Predictions for a Modern, High-Pressure, Transonic Turbine, Including Endwalls," *Journal of Turbomachinery,* vol. 131, no. 2, p. 021001, 2009.

[66] J. S. Carullo *et al.*, "The Effects of Freestream Turbulence, Turbulence Length Scale, and Exit Reynolds Number on Turbine Blade Heat Transfer in a Transonic Cascade," *Journal of Turbomachinery,* vol. 133, no. 1, p. 011030, 2011.

[67] M. T. Schobeiri, B. Öztürk, M. Kegalj, and D. Bensing, "On the physics of heat transfer and aerodynamic behavior of separated flow along a highly loaded low

pressure turbine blade under periodic unsteady wake flow and varying of turbulence intensity," *Journal of heat transfer,* vol. 130, no. 5, p. 051703, 2008.

[68] S. Wolff, L. Homeier, and L. Fottner, "Experimental investigation of heat transfer in separated flow on a highly loaded LP turbine cascade," DTIC Document2003.

[69] S. M. Choi, J. S. Park, H. Chung, B. M. Chang, and H. H. Cho, "Effect of Unsteady Wakes on Local Heat Transer of 1st Stage Blade Endwall," in *ASME Turbo Expo 2015: Turbine Technical Conference and Exposition*, 2015, pp. V05BT13A024-V05BT13A024: American Society of Mechanical Engineers.

[70] J. S. Park *et al.*, "Effects of Unsteady Wake on Heat Transfer of Endwall Surface in Linear Cascade," *Journal of Heat Transfer,* vol. 136, no. 6, p. 061701, 2014.

[71] K. Abe, T. Kondoh, and Y. Nagano, "A new turbulence model for predicting fluid flow and heat transfer in separating and reattaching flows—I. Flow field calculations," *International Journal of Heat and Mass Transfer,* vol. 37, no. 1, pp. 139-151, 1994.

[72] K. Abe, T. Kondoh, and Y. Nagano, "A new turbulence model for predicting fluid flow and heat transfer in separating and reattaching flows—II. Thermal field calculations," *International Journal of Heat and Mass Transfer,* vol. 38, no. 8, pp. 1467-1481, 1995.

[73] K. Heyerichs and A. Pollard, "Heat transfer in separated and impinging turbulent flows," *International Journal of Heat and Mass Transfer,* vol. 39, no. 12, pp. 2385-2400, 1996.

[74] M. G. Dunn, "Convection heat transfer and aerodynamics in axial flow turbines," *ASME Journal of Turbomachinery,* vol. 123, no. 4, p. 50, 2001.

[75] G. Medic and P. Durbin, "Toward improved prediction of heat transfer on turbine blades," *Journal of turbomachinery,* vol. 124, no. 2, pp. 187-192, 2002.

[76] K. Hermanson, S. Kern, G. Picker, and S. Parneix, "Predictions of external heat transfer for turbine vanes and blades with secondary flowfields," *Journal of turbomachinery,* vol. 125, no. 1, pp. 107-113, 2003.

[77] P. De la Calzada and A. Alonso, "Numerical investigation of heat transfer in turbine cascades with separated flows," *Journal of turbomachinery,* vol. 125, no. 2, pp. 260-266, 2003.

[78] J. A. Tallman, "CFD Heat Transfer Predictions for a High-Pressure Turbine Stage," in *ASME Turbo Expo 2004: Power for Land, Sea, and Air*, 2004, pp. 577-588: American Society of Mechanical Engineers.

[79] C. W. Haldeman, M. G. Dunn, J. W. Barter, B. R. Green, and R. F. Bergholz, "Aerodynamic and heat-flux measurements with predictions on a modern one and one-half state high pressure transonic turbine," *Journal of Turbomachinery,* vol. 127, no. 3, pp. 522-531, 2005.

[80] M. B. Giles, "Calculation of unsteady wake/rotor interaction," *Journal of Propulsion and Power,* vol. 4, no. 4, pp. 356-362, 1988.

[81] M. B. Giles, "Nonreflecting boundary conditions for Euler equation calculations," *AIAA journal,* vol. 28, no. 12, pp. 2050-2058, 1990.

[82] P. De La Calzada, M. Valdes, and M. Burgos, "Heat transfer in separated flows on the pressure side of turbine blades," *Numerical Heat Transfer, Part A: Applications,* vol. 60, no. 8, pp. 666-684, 2011.

[83] C. Wang *et al.*, "Experimental and numerical investigation of outlet guide vane and endwall heat transfer with various inlet flow angles," *International Journal of Heat and Mass Transfer,* vol. 95, pp. 355-367, 2016.

[84] O. Reynolds, "On the experimental investigation of the circumstances which determine whether the motion of water in parallel channels shall be direct of sinuous and of the law of resistance in parallel channels," *Philosophical Transactions of the Royal society of London,* vol. 174, 1883.

[85] J. M. Burgers, *The motion of a fluid in the boundary layer along a plane smooth surface*. Waltman, 1925.

[86] B. G. Van der Hegge Zijnen, "Measurements of the velocity distribution in the boundary layer along a plane surface," TU Delft, Delft University of Technology, 1924.

[87] L. Prandtl, "Über die Entstehung der Turbulenz," *ZAMM‐Journal of Applied Mathematics and Mechanics/Zeitschrift für Angewandte Mathematik und Mechanik,* vol. 11, no. 6, pp. 407-409, 1931.

[88] H. Schlichting, "Zur enstehung der turbulenz bei der plattenströmung," *Nachrichten von der Gesellschaft der Wissenschaften zu Göttingen, Mathematisch-Physikalische Klasse,* vol. 1933, pp. 181-208, 1933.

[89] A. Sommerfeld, "Ein beitrag zur hydrodynamischen erklaerung der turbulenten fluessigkeitsbewegungen," *Atti del,* vol. 4, pp. 116-124, 1908.

[90] W. M. F. Orr, "The stability or instability of the steady motions of a perfect liquid and of a viscous liquid. Part II: A viscous liquid," in *Proceedings of the Royal*

Irish Academy. Section A: Mathematical and Physical Sciences, 1907, vol. 27, pp. 69-138: JSTOR.

[91] A. Hatman and T. Wang, "A prediction model for separated-flow transition," *Journal of Turbomachinery,* vol. 121, no. 3, pp. 594-602, 1999.

[92] R. Mayle, "The role of laminar-turbulent transition in gas turbine engines," in *(ASME, International Gas Turbine and Aeroengine Congress and Exposition, 36 th, Orlando, FL, June 3-6, 1991) ASME, Transactions, Journal of Turbomachinery*, 1991, vol. 113, pp. 509-537.

[93] M. V. Morkovin, "On the many faces of transition," in *Viscous drag reduction*: Springer, 1969, pp. 1-31.

[94] H. W. Emmons, "The laminar-turbulent transition in a boundary layer-Part I," *Journal of the Aeronautical Sciences,* 1951.

[95] J. Dey and R. Narasimha, *An integral method for the calculation of 2-D transitional boundary layers*. Indian Institute of Science, 1988.

[96] A. A. Townsend, "The Fully Developed Wake of a Circular Cylinder," *Australian Journal of Scientific Research,* vol. 2, no. 4, pp. 451-468, 1949.

[97] T. B. Hedley and J. F. Keffer, "Turbulent/non-turbulent decisions in an intermittent flow," *Journal of Fluid Mechanics,* vol. 64, no. 04, pp. 625-644, 1974.

[98] D. E. Paxson and R. E. Mayle, "Laminar boundary layer interaction with an unsteady passing wake," *Journal of turbomachinery,* vol. 113, no. 3, pp. 419-427, 1991.

[99] B. Abu-Ghannam and R. Shaw, "Natural transition of boundary layers—the effects of turbulence, pressure gradient, and flow history," *Journal of Mechanical Engineering Science,* vol. 22, no. 5, pp. 213-228, 1980.

[100] G. J. Walker and J. P. Gostelow, "Effects of adverse pressure gradients on the nature and length of boundary layer transition," in *ASME 1989 International Gas Turbine and Aeroengine Congress and Exposition*, 1989, pp. V001T01A096-V001T01A096: American Society of Mechanical Engineers.

[101] J. Gostelow, A. Blunden, and G. Walker, "Effects of free-stream turbulence and adverse pressure gradients on boundary layer transition," *Journal of turbomachinery,* vol. 116, no. 3, pp. 392-404, 1994.

[102] M. T. Schobeiri, *Applied fluid mechanics for engineers*. McGraw-Hill Professional Publishing, 2014.

[103] L. S. Kovasznay, "The turbulent boundary layer," *Annual review of fluid mechanics,* vol. 2, no. 1, pp. 95-112, 1970.

[104] M. T. Schobeiri, "The Ultra-High Efficiency Gas Turbine Engine With Stator Internal Combustion, UHEGT," *US patent application,* vol. 62, no. 046,542, 2014.

[105] G. B. Schubauer and P. S. Klebanoff, "Contributions on the mechanics of boundary-layer transition," 1955.

[106] R. Herbst, *Entwicklung von Grenzschichten bei instationärer Zuströmung*. na, 1980.

[107] O. Reynolds, "XXIX. An experimental investigation of the circumstances which determine whether the motion of water shall he direct or sinuous, and of the law

of resistance in parallel channels," *Philosophical Transactions of the Royal Society of London,* vol. 174, pp. 935-982, 1884.

[108] R. H. Pletcher, J. C. Tannehill, and D. Anderson, *Computational fluid mechanics and heat transfer*. CRC Press, 2012.

[109] M. T. Schobeiri, *Fluid Mechanics for Engineers: A Graduate Textbook*. Springer Science & Business Media, 2010.

[110] A. Smith and T. Cebeci, "Numerical Solution of the Turbulent-boundary-layer Equations," DTIC Document1967.

[111] P. Klebanoff, "Characteristics of turbulence in boundary layer with zero pressure gradient," 1955.

[112] L. Prandtl, "Über ein neues formelsystem für die ausgebildete turbulenz, nachr. d. akad. d. wiss," *Göttingen, Math.-nat. Klasse,* pp. 6-20, 1945.

[113] B. S. Baldwin and T. J. Barth, *A one-equation turbulence transport model for high Reynolds number wall-bounded flows*. National Aeronautics and Space Administration, Ames Research Center, 1990.

[114] P. R. Spalart and S. R. Allmaras, "A one equation turbulence model for aerodinamic flows," *AIAA journal,* vol. 94, 1992.

[115] B. E. Launder and D. Spalding, "The numerical computation of turbulent flows," *Computer methods in applied mechanics and engineering,* vol. 3, no. 2, pp. 269-289, 1974.

[116] D. C. Wilcox, "Turbulent modeling for CFD," *DCW Industries, La Candad, CA, USA,* 1998.

[117] P. R. Spalart and M. Shur, "On the sensitization of turbulence models to rotation and curvature," *Aerospace Science and Technology,* vol. 1, no. 5, pp. 297-302, 1997.

[118] A. M. O. Smith and N. Gamberoni, "Transition, pressure gradient and stability theory," *Douglas Aircraft Co., Report ES 26388,* 1956.

[119] J. Van Ingen, "A suggested semi-empirical method for the calculation of the boundary layer transition region," *Technische Hogeschool Delft, Vliegtuigbouwkunde, Rapport VTH-74,* 1956.

[120] H. Schlichting, "Boundary layer theory; Trans. J. Kestin," 1960.

[121] C. Sheng and J. Wang, *Advances in Transitional Flow Modeling: Applications to Helicopter Rotors*. Springer, 2017.

[122] H. W. Stock and W. Haase, "Navier-Stokes Airfoil Computations with e Transition Prediction Including Transitional Flow Regions," *AIAA journal,* vol. 38, no. 11, pp. 2059-2066, 2000.

[123] J. Van Ingen, "The eN method for transition prediction. Historical review of work at TU Delft," in *38th Fluid Dynamics Conference and Exhibit*, 2008, pp. 23-26.

[124] B. S. Baldwin and H. Lomax, *Thin layer approximation and algebraic model for separated turbulent flows*. American Institute of Aeronautics and Astronautics, 1978.

[125] J. Lumley, "Second order modeling of turbulent flows," in *Von Karman Inst. for Fluid Dynamics: Prediction Methods for Turbulent Flows*, 1979.

[126] P. A. Libby, "On the prediction of intermittent turbulent flows," *Journal of Fluid Mechanics,* vol. 68, no. 02, pp. 273-295, 1975.

[127] S. Byggstøyl and W. Kollmann, "Closure model for intermittent turbulent flows," *International Journal of Heat and Mass Transfer,* vol. 24, no. 11, pp. 1811-1822, 1981.

[128] P. Huang and G. Xiong, "Transition and turbulence modeling of low pressure turbine flows," *AIAA paper,* no. 98-0039, 1998.

[129] A. Nikparto and M. T. Schobeiri, "Combined numerical and experimental investigations of heat transfer of a highly loaded low-pressure turbine blade under periodic inlet flow condition," *Proceedings of the Institution of Mechanical Engineers, Part A: Journal of Power and Energy,* p. 0957650918758158, 2018.

[130] L. Prandtl, "Bericht über Untersuchungen zur ausgebildeten Turbulenz," *Z. Angew. Math. Mech,* vol. 5, no. 2, pp. 136-139, 1925.

[131] J. D. Denton, "Some limitations of turbomachinery CFD," *ASME Paper No. GT2010-22540,* pp. 735-745, 2010.

[132] B. Ozturk, "Combined effects of Reynolds number, turbulence intensity and periodic unsteady wake flow conditions on boundary layer development and heat transfer of a low pressure turbine blade," 69, Department of Mechanical Engineering, Texas A&M University, 01, 2006.

[133] M. T. Schobeiri, S. Abdelfattah, and H. Chibli, "Investigating the cause of computational fluid dynamics deficiencies in accurately predicting the efficiency and performance of high pressure turbines: A combined experimental and numerical study," *Journal of fluids engineering,* vol. 134, no. 10, p. 101104, 2012.

[134] P. Chakka and M. Schobeiri, "Scales of turbulence during boundary layer transition under steady and unsteady flow conditions," in *ASME 1999*

International Gas Turbine and Aeroengine Congress and Exhibition, 1999, pp. V003T01A063-V003T01A063: American Society of Mechanical Engineers.

[135] J. Bredberg, "On the wall boundary condition for turbulence models," *Chalmers University of Technology, Department of Thermo and Fluid Dynamics. Internal Report 00/4. G oteborg,* 2000.

[136] H. Tennekes and J. L. Lumley, *A first course in turbulence*. MIT press, 1972.

[137] M. T. Schobeiri, B. Öztürk, and D. E. Ashpis, "On the physics of flow separation along a low pressure turbine blade under unsteady flow conditions," *Journal of fluids engineering,* vol. 127, no. 3, pp. 503-513, 2005.

[138] P. Chakka, "Unsteady wake effects on boundary layer transition and heat transfew characteristics of curved plate and turbine blade," Texas A & M University, 1998.

[139] M. T. Schobeiri, "Influence of Curvature and Pressure Gradient on Turbulent Wake Development in Curved Channels," *Journal of Fluids Engineering,* vol. 130, no. 9, p. 091201, 2008.

[140] M. R. Khajavi and M. H. Shariat, "Failure of first stage gas turbine blades," *Engineering Failure Analysis,* vol. 11, no. 4, pp. 589-597, 2004.

[141] B. Lakshminarayana, "Turbine Cooling and Heat Transfer," *Fluid Dynamics and Heat Transfer of Turbomachinery,* 1996.

[142] R. J. Goldstein, E. R. G. Eckert, and F. Burggraf, "Effects of hole geometry and density on three-dimensional film cooling," *International Journal of Heat and Mass Transfer,* vol. 17, no. 5, pp. 595-607, 1974.

[143] N. W. Foster and D. Lampard, "The flow and film cooling effectiveness following injection through a row of holes," *Journal of Engineering for Power,* vol. 102, no. 3, pp. 584-588, 1980.

[144] B. Schonung and W. Rodi, "Prediction of film cooling by a row of holes with a two-dimensional boundary-layer procedure," *Journal of turbomachinery,* vol. 109, no. 4, pp. 579-587, 1987.

[145] W. Haas, W. Rodi, and B. Schonung, "The influence of density difference between hot and coolant gas on film cooling by a row of holes: predictions and experiments," *Journal of turbomachinery,* vol. 114, no. 4, pp. 747-755, 1992.

[146] R. S. Abhari and A. H. Epstein, "An experimental study of film cooling in a rotating transonic turbine," in *ASME 1992 International Gas Turbine and Aeroengine Congress and Exposition*, 1992, pp. V004T09A018-V004T09A018: American Society of Mechanical Engineers.

[147] S. Ou, J. C. Han, A. B. Mehendale, and C. P. Lee, "Unsteady Wake Over a Linear Turbine Blade Cascade With Air and CO2 Film Injection: Part I—Effect on Heat Transfer Coefficients," *Journal of Turbomachinery,* vol. 116, no. 4, pp. 721-729, 1994.

[148] A. B. Mehendale, J. C. Han, S. Ou, and C. P. Lee, "Unsteady Wake Over a Linear Turbine Blade Cascade With Air and CO2 Film Injection: Part II—Effect on Film Effectiveness and Heat Transfer Distributions," *Journal of turbomachinery,* vol. 116, no. 4, pp. 730-737, 1994.

[149] S. Teng, D. K. Sohn, and J.-C. Han, "Unsteady wake effect on film temperature and effectiveness distributions for a gas turbine blade," *Journal of turbomachinery,* vol. 122, no. 2, pp. 340-347, 2000.

[150] N. Abuaf, R. Bunker, and C. P. Lee, "Heat transfer and film cooling effectiveness in a linear airfoil cascade," *Journal of turbomachinery,* vol. 119, no. 2, pp. 302-309, 1997.

[151] F. E. Ames, "Aspects of Vane Film Cooling With High Turbulence: Part I—Heat Transfer," *Journal of turbomachinery,* vol. 120, no. 4, pp. 768-776, 1998.

[152] F. E. Ames, "Aspects of Vane Film Cooling With High Turbulence: Part II—Adiabatic Effectiveness," *Journal of Turbomachinery,* vol. 120, no. 4, pp. 777-784, 1998.

[153] J. D. Heidmann, B. L. Lucci, and E. Reshotko, "An experimental study of the effect of wake passing on turbine blade film cooling," *Journal of Turbomachinery,* vol. 123, no. 2, pp. 214-221, 2001.

[154] D. P. Narzary, Z. Gao, S. Mhetras, and J.-C. Han, "Effect of unsteady wake on film-cooling effectiveness distribution on a gas turbine blade with compound shaped holes," in *ASME Turbo Expo 2007: Power for Land, Sea, and Air*, 2007, pp. 79-91: American Society of Mechanical Engineers.

[155] J. P. Bons, "A review of surface roughness effects in gas turbines," *Journal of turbomachinery,* vol. 132, no. 2, p. 021004, 2010.

[156] R. A. Gomes and R. Niehuis, "Film cooling effectiveness measurements with periodic unsteady inflow on highly loaded blades with main flow separation," *Journal of Turbomachinery,* vol. 133, no. 2, p. 021019, 2011.

[157] L. A. El-Gabry, D. R. Thurman, P. E. Poinsatte, and J. D. Heidmann, "Turbulence and Heat Transfer Measurements in an Inclined Large Scale Film Cooling Array: Part I—Velocity and Turbulence Measurements," in *ASME 2011 Turbo Expo: Turbine Technical Conference and Exposition*, 2011, pp. 541-550: American Society of Mechanical Engineers.

[158] D. R. Thurman, L. A. El-Gabry, P. E. Poinsatte, and J. D. Heidmann, "Turbulence and Heat Transfer Measurements in an Inclined Large Scale Film Cooling Array: Part II—Temperature and Heat Transfer Measurements," in *ASME 2011 Turbo Expo: Turbine Technical Conference and Exposition*, 2011, pp. 551-558: American Society of Mechanical Engineers.

[159] A. P. Rallabandi, S.-J. Li, and J.-C. Han, "Unsteady Wake and Coolant Density Effects on Turbine Blade Film Cooling Using Pressure Sensitive Paint Technique," *Journal of Heat Transfer,* vol. 134, no. 8, p. 081701, 2012.

[160] M. T. Schobeiri and S. M. Ghoreyshi, "The Ultrahigh Efficiency Gas Turbine Engine With Stator Internal Combustion," *Journal of Engineering for Gas Turbines and Power,* vol. 138, no. 2, p. 021506, 2016.

[161] N. H. Chowdhury, H. Zirakzadeh, and J.-C. Han, "A Predictive Model for Preliminary Gas Turbine Blade Cooling Analysis," in *ASME Turbo Expo 2015: Turbine Technical Conference and Exposition*, 2015, pp. V05BT13A002-V05BT13A002: American Society of Mechanical Engineers.

[162] M. T. Schobeiri, K. Pappu, and L. Wright, "Experimental study of the unsteady boundary layer behavior on a turbine cascade," in *ASME 1995 International Gas*

Turbine and Aeroengine Congress and Exposition, 1995, pp. V001T01A100-V001T01A100: American Society of Mechanical Engineers.

[163] M. T. Schobeiri and B. Özturk, "Turbulence Development and Decay Upstream of the LPT-Cascade," *NASA GRC LPT-Project Progress Report,* no. 2004-2, 2004.

[164] M. T. Schobeiri, J. John, and K. Pappu, "Development of Two-Dimensional Wakes Within Curved Channels, Theoretical Framework and Experimental Investigation," in *ASME 1994 International Gas Turbine and Aeroengine Congress and Exposition*, 1994, pp. V001T01A127-V001T01A127: American Society of Mechanical Engineers.

[165] B. ÖZtÜRk, "Combined effects of Reynolds number, turbulence intensity and periodic unsteady wake flow conditions on boundary layer development and heat transfer of a low pressure turbine blade," Texas A&M University, 2006.

[166] R. J. Goldstein, "Film cooling," *Advances in heat transfer,* vol. 7, pp. 321-379, 1971.

[167] W. M. Kays, M. E. Crawford, and B. Weigand, *Convective heat and mass transfer*. Tata McGraw-Hill Education, 2012.

[168] T. V. Jones, "Theory for the use of foreign gas in simulating film cooling," *International Journal of Heat and Fluid Flow,* vol. 20, no. 3, pp. 349-354, 1999.

[169] W. B. Nicoll and J. H. Whitelaw, "The effectiveness of the uniform density, two-dimensional wall jet," *International Journal of Heat and Mass Transfer,* vol. 10, no. 5, pp. 623-639, 1967.

[170] R. J. Goldstein and J. R. Taylor, "Mass transfer in the neighborhood of jets entering a crossflow," *Journal of Heat Transfer,* vol. 104, no. 4, pp. 715-721, 1982.

[171] R. J. Goldstein and R. A. Spores, "Turbulent transport on the endwall in the region between adjacent turbine blades," *Journal of Heat Transfer,* vol. 110, no. 4a, pp. 862-869, 1988.

[172] R. J. Goldstein and P. Jin, "Film cooling downstream of a row of discrete holes with compound angle," in *ASME Turbo Expo 2000: Power for Land, Sea, and Air*, 2000, pp. V003T01A054-V003T01A054: American Society of Mechanical Engineers.

[173] S. Friedrichs, H. P. Hodson, and W. N. Dawes, "Distribution of film-cooling effectiveness on a turbine endwall measured using the ammonia and diazo technique," in *ASME 1995 International Gas Turbine and Aeroengine Congress and Exposition*, 1995, pp. V004T09A001-V004T09A001: American Society of Mechanical Engineers.

[174] N. Macleod and R. B. Todd, "The experimental determination of wall-fluid mass transfer coefficients using plasticized polymer surface coatings," *International Journal of Heat and Mass Transfer,* vol. 16, no. 2, pp. 485-504, 1973.

[175] B. W. Noel *et al.*, "Evaluating thermographic phosphors in an operating turbine engine," in *ASME 1990 International Gas Turbine and Aeroengine Congress and Exposition*, 1990, pp. V002T02A022-V002T02A022: American Society of Mechanical Engineers.

[176] L. J. Zhang and R. S. Jaiswal, "Turbine nozzle endwall film cooling study using pressure-sensitive paint," *Journal of Turbomachinery,* vol. 123, no. 4, pp. 730-738, 2001.

[177] M. Rezasoltani, "Experimental invesitgation of flow and film cooling with endwall contouring and blade tip ejection under rotating turbine conditions," Texas A&M University, 2015.

[178] L. M. Wright, Z. Gao, T. A. Varvel, and J.-C. Han, "Assessment of steady state PSP, TSP, and IR measurement techniques for flat plate film cooling," in *ASME 2005 Summer Heat Transfer Conference collocated with the ASME 2005 Pacific Rim Technical Conference and Exhibition on Integration and Packaging of MEMS, NEMS, and Electronic Systems*, 2005, pp. 37-46: American Society of Mechanical Engineers.

[179] A. P. Rallabandi, J. Grizzle, and J.-C. Han, "Effect of upstream step on flat plate film-cooling effectiveness using PSP," *Journal of Turbomachinery,* vol. 133, no. 4, p. 041024, 2011.

[180] A. Nikparto and M. T. Schobeiri, "Experimental Investigation of Film Cooling Effectiveness of a Highly Loaded Turbine Blade Under Steady and Periodic Unsteady Flow Conditions," *Journal of Heat Transfer,* vol. 139, no. 7, 2017.

[181] K. Rubner and D. Bohn, "Verfahren für die Auswertung der Messergebnisse von Strömungssonden durch mehrdimensionale Approximation der Eichkurven und Eichflächen Z," *Flugwiss,* vol. 20, pp. 36-42, 1972.

[182] Z. Gao, D. P. Narzary, and J.-C. Han, "Film-Cooling on a Gas Turbine Blade Pressure Side or Suction Side With Compound Angle Shaped Holes," *Journal of Turbomachinery,* vol. 131, no. 1, pp. 011019-011019, 2008.

[183] K. Liu, S.-F. Yang, and J.-C. Han, "Influence of Coolant Density on Turbine Blade Film-Cooling With Compound-Angle Shaped Holes," in *ASME Turbo Expo 2012: Turbine Technical Conference and Exposition*, 2012, pp. 1559-1569: American Society of Mechanical Engineers.

[184] S. J. Kline and F. A. McClintock, "Describing uncertainties in single-sample experiments," *Mechanical engineering,* vol. 75, no. 1, pp. 3-8, 1953.

[185] O. P. Sharma and T. L. Butler, "Predictions of endwall losses and secondary flows in axial flow turbine cascades," in *ASME 1986 International Gas Turbine Conference and Exhibit*, 1986, pp. V001T01A098-V001T01A098: American Society of Mechanical Engineers.

[186] J. Wang, B. Sundén, M. Zeng, and Q.-W. Wang, "Effect of Upstream Wake on Passage Flow and Tip Film Cooling Characteristics," in *ASME Turbo Expo 2012: Turbine Technical Conference and Exposition*, 2012, pp. 1381-1387: American Society of Mechanical Engineers.

[187] K. Funazaki, M. Yokota, and S. Yamawaki, "Effect of periodic wake passing on film effectiveness of discrete cooling holes around the leading edge of a blunt body," *Journal of Turbomachinery,* vol. 119, no. 2, pp. 292-301, 1997.

[188] S. G. Schwarz, R. J. Goldstein, and E. R. G. Eckert, "The Influence of Curvature on Film Cooling Performance," *Journal of Turbomachinery,* vol. 113, no. 3, pp. 472-478, 1991.

[189] A. Nikparto, T. Rice, and M. Schobeiri, "Experimental And Numerical Investigation Of Heat Transfer And Film Cooling Effectiveness Of A Highly Loaded Turbine Blade Under Steady And Unsteady Wake Flow Condition," in *ASME Turbo Expo 2017: Turbomachinery Technical Conference and Exposition*, 2017, pp. V05CT19A029-V05CT19A029: American Society of Mechanical Engineers.

[190] F. R. Menter and Y. Egorov, "The scale-adaptive simulation method for unsteady turbulent flow predictions. Part 1: theory and model description," *Flow, Turbulence and Combustion,* vol. 85, no. 1, pp. 113-138, 2010.

[191] T. auf dem Kampe *et al.*, "Experimental and Numerical Investigation of Flow Field and Downstream Surface Temperatures of Cylindrical and Diffuser Shaped Film Cooling Holes1," *Journal of Turbomachinery,* vol. 135, no. 1, p. 011026, 2013.

[192] D. Lakehal, G. Theodoridis, and W. Rodi, "Three-dimensional flow and heat transfer calculations of film cooling at the leading edge of a symmetrical turbine blade model," *International journal of heat and fluid flow,* vol. 22, no. 2, pp. 113-122, 2001.

[193] G. Ingram, D. Gregory-Smith, M. Rose, N. Harvey, and G. Brennan, "The effect of end-wall profiling on secondary flow and loss development in a turbine cascade," in *ASME Turbo Expo 2002: Power for Land, Sea, and Air*, 2002, pp. 135-145: American Society of Mechanical Engineers.

[194] A. Rozati and D. K. Tafti, "Effect of coolant–mainstream blowing ratio on leading edge film cooling flow and heat transfer–LES investigation," *International Journal of Heat and Fluid Flow,* vol. 29, no. 4, pp. 857-873, 2008.

[195] T. a. d. Kampe and S. Völker, "A Model for Cylindrical Hole Film Cooling—Part II: Model Formulation, Implementation and Results," *Journal of Turbomachinery,* vol. 134, no. 6, pp. 061011-061011, 2012.

[196] M. K. Berhe and S. V. Patankar, "Curvature effects on discrete-hole film cooling," *Journal of turbomachinery,* vol. 121, no. 4, pp. 781-791, 1999.

[197] M. Deinert and J. Hourmouziadis, "Film Cooling in unsteady flow with separation bubble," in *ASME Turbo Expo 2004: Power for Land, Sea, and Air*, 2004, pp. 55-66: American Society of Mechanical Engineers.

[198] A. Krothapalli, L. Lourenco, and J. M. Buchlin, "Separated flow upstream of a jet in a crossflow," *AIAA journal,* vol. 28, no. 3, pp. 414-420, 1990.

APPENDIX A

Perspective correction code

```
%%
% read original image

% clear; close all
  filename = 'WO.png';
  img = im2double(rgb2gray(imread(filename)));
  name = 'check2';
  msgid = 'Images:initSize:adjustingMag';
  warning('off',msgid);
  imshow(img);


%%
%[c r p] = impixel;
c = [ 167 232 281 214 ]';
r = [ 149 174 138 119 ]';
base = [0 300; 30/53*500 300; 30/53*500 0; 0 0];
tf = cp2tform([c r],base*1,'projective');
disp('tf = ');
disp(tf)
disp('tf.tdata = ');
disp(tf.tdata);

T = tf.tdata.T;
disp('T =');
format short g
disp(T);
format

%%
% overlay control points on image

% imshow(img);
% hold on;
% plot([c;c(1)],[r;r(1)],'r','Linewidth',2);
% text(c(1),r(1)+20,'0, 193','Color','y');
% text(c(2),r(2)+20,'400, 193','Color','y');
% text(c(3),r(3)-20,'400, 0','Color','y');
% text(c(4),r(4)-20,'0, 0','Color','y');
% hold off;
% F = getframe();
% g = frame2im(F);
% imwrite(g,[name '_overlay.jpg']);

%%
% do image transform

[xf1, XData, YData] = imtransform(eta,tf);
imshow(xf1)
imwrite(xf1,[name '_registeredWO.jpg']);
```

Film cooling effectiveness code(Air.m)

```
% clear all
% close all


tic

X0 = 1;
Y0 = 1;

W   = 320;
H   = 240;

Start=1
End=100

% Start=101
% End=200


'air'
name = 'air_';
sumair=zeros(H,W);


for i = Start:End

    if( ~mod(i,10) )
        fprintf('%d\n',End-i)
    end

    num = sprintf('%04d',i);
    ifile = strcat( name,num,'.tif');

    I = imread( ifile, 'tif' );
    I = I(Y0:Y0+H-1,X0:X0+W-1);
    intenair=double(I);
    sumair=sumair+intenair;


end


   toc
```

Film cooling effectiveness code(Black.m)

```
tic

X0 = 1;
Y0 = 1;

W   = 320;
H   = 240;

Start=1
End=100


name = 'black_';
sumblack=zeros(H,W);


for i = Start:End

    if( ~mod(i,10) )
        fprintf('%d\n',End-i)
    end

    num = sprintf('%04d',i);
    ifile = strcat( name,num,'.tif');

    I = imread( ifile, 'tif' );
    I = I(Y0:Y0+H-1,X0:X0+W-1);
    intenblack=double(I);
    sumblack=sumblack+intenblack;


end

   toc
```

Film cooling effectiveness code(N.m)

```
% clear all
% close all


tic

X0 = 1;
Y0 = 1;

W   = 320;
H   = 240;

Start=1
End=100

% Start=101
% End=200


'N'
name = 'N_';
sumN=zeros(H,W);


for i = Start:End

    if( ~mod(i,10) )
        fprintf('%d\n',End-i)
    end

    num = sprintf('%04d',i);
    ifile = strcat( name,num,'.tif');

    I = imread( ifile, 'tif' );
    I = I(Y0:Y0+H-1,X0:X0+W-1);
    intenN=double(I);
    sumN=sumN+intenN;


end


   toc
```

Film cooling effectiveness code(ref.m)

```
% clear all
% close all

tic

X0 = 1;
Y0 = 1;

W   = 320;
H   = 240;

Start=1
End=100


name = 'Ref_';
sumref=zeros(H,W);


for i = Start:End

    if( ~mod(i,10) )
        fprintf('%d\n',End-i)
    end

    num = sprintf('%04d',i);
    ifile = strcat( name,num,'.tif');

    I = imread( ifile, 'tif' );
    I = I(Y0:Y0+H-1,X0:X0+W-1);
    intenref=double(I);
    sumref=sumref+intenref;


end

   toc
```

Film cooling effectiveness code(etha.m)

```
%-- 12/10/14, 9:36 AM --%
sum=zeros(H,W);
sumA=(sumref-sumblack)./(sumair-sumblack);
sumN2=(sumref-sumblack)./(sumN-sumblack);
ydenominator=-0.112*sumA.^3+1.38735*sumA.^2-0.2582*sumA+0.02595;
ynumerator=-0.112*sumN2.^3+1.38735*sumN2.^2-0.2582*sumN2+0.02595;
eta=1-ynumerator./ydenominator;
% contourf(eta)
ofile = strcat( 'etaRcrop.dat');
fid = fopen(ofile,'w');
fprintf(fid,'zone j=240 i=320\n');
for ii = 1:H
for jj = 1:W
fprintf(fid, '%6.2f  %6.2f    %12.2f',jj,ii,eta(ii,jj));
fprintf(fid, '\n');
end
end
contourf(eta)
```

Pitot tube code(etha.f)

```
      PROGRAM CASCADE
      DOUBLE PRECISION PI,KELVIN,C
      PARAMETER (PI=3.14159265D0,KELVIN=273.15D0,C=0.20344D0)
      DOUBLE PRECISION TT,TS,PT,PS,PD,V,VX,VY,VZ,ALPHA,BETA,DEGREE,
     $                 P1,P2,P3,P4,P5,RH,RHO,RE,BAR,MU
      CHARACTER TITLE*100
      INTEGER Q
C read inout file name

      OPEN(UNIT=45,FILE='info.txt',STATUS='OLD')
      READ(45,*)
      READ(45,'(A)') TITLE
      CALL CLEAN(TITLE,Q)
C open files for input/output
      OPEN(UNIT=50,FILE='out.dat',STATUS='UNKNOWN')
      OPEN(UNIT=40,FILE=TITLE(1:Q),STATUS='OLD')
C read basic data from input file
      READ(40,*)
      READ(40,*)
      READ(40,*)
      READ(40,*)
      READ(40,*) TT
      READ(40,*)
      READ(40,*)
      READ(40,*)
      READ(40,*)
      READ(40,*)
      READ(40,*)
      READ(40,*)
      READ(40,*) BAR
      READ(40,*)
      READ(40,*)
      READ(40,*)
      READ(40,*) RH
      READ(40,*)
      READ(40,*)
      READ(40,*)
      READ(40,*)
      READ(40,*)
      READ(40,*)
      READ(40,*)
      READ(40,*)
      READ(40,*)
      READ(40,*)
      READ(40,*)
      READ(40,*)
      READ(40,*) P1
      READ(40,*) P2
      READ(40,*) P3
      READ(40,*) P4
      READ(40,*) P5
C change the total temperature unit to Kelvin

      TT=TT+KELVIN
C call calibration subroutines to reduce 5-hole-probe data (Cobra Probe)
      CALL CLB8(P1,P2,P3,P4,P5,PS,PT,ALPHA,BETA)
```

```
C calculate the dynamic head
      PD=PT-PS
C calculate the static temperature

      CALL TSTAT(TT,PT+BAR,PS+BAR,TS)
C calculate the static density

      CALL DEN(TS,PS+BAR,RH,RHO)
C calculate the velocities

      DEGREE=PI/180.0D0
      IF(PT.LT.PS) THEN
        PRINT*,'ERROR: BAD DATA POINT'
        STOP
      ENDIF
      V=(2.0D0*(PT-PS)/(RHO))**0.5D0
      VX=V*DCOS(BETA*DEGREE)*DCOS(ALPHA*DEGREE)
      VY=-V*DSIN(BETA*DEGREE)
      VZ=V*DCOS(BETA*DEGREE)*DSIN(ALPHA*DEGREE)

C calculate the viscosity
      MU=1.46D-06*((TS**1.5D0)/(TS+111.0D0))
C calculate the same number

      RE=RHO*V*C/MU
C write full data to output file

      WRITE(50,100)
      WRITE(50,300) TT,TS,PT,PS,PD,ALPHA,BETA,V,VX,VY,VZ,RHO,RE

  100 FORMAT(2X,'Tt [K]',3X,'Ts [K]',2X,'Pt [PA]',2X,'Ps [PA]',

     $      2X,'Pd [PA]',2X,'ALPHA [DEG]',2X,'BETA [DEG]',
     $      2X,'V [M/SEC]',2X,'Vx [M/SEC]',2X,'Vy [M/SEC]',
     $      2X,'Vz [M/SEC]',2X,'Rho [KG/M**3]',7X,'Re []',//)

  300 FORMAT(1X,F7.2,2X,F7.2,2X,F7.1,2X,F7.1,2X,F7.1,2X,

     $      F11.3,2X,F10.3,2X,F9.2,2X,F10.2,2X,
     $      F10.2,2X,F10.2,2X,F13.3,2X,F10.1)

      PRINT*, 'END OF ANALYSIS'
      STOP

      END

*************************************************************************
* This subroutine will read the five probe pressures and use the       *
* calibration subroutines to calculate the total and static flow       *
* pressures as well as the flow angles. It utilizes the Bohn's method  *
* of calibration.
* Input Files : N/A                                                    *
* Output Files: N/A                                                    *
* Experimental Procedure: Cascade Facility of the DOOSAN II Blade      *

      SUBROUTINE CLB8(P1,P2,P3,P4,P5,PS,PT,ALPHA,BETA)

C Define variables, parameters and constants to use
```

```
      DOUBLE PRECISION P1,P2,P3,P4,P5,PS,PT,ALPHA,BETA,PI,GUESS,ER,
     $                 LIMIT,INITIAL,CHECK,Q1,Q2,Q3,Q4,Q5
      INTEGER M
      PARAMETER(PI=3.141592654D0,INITIAL=0.8D0,LIMIT=0.001D0)
      GUESS=INITIAL*P1
      M=0
    3 Q1=(P4-P5)/(P1-GUESS)
      Q2=(P3-P2)/(P1-GUESS)
      M=M+1
C Call calibration subroutines

      CALL GETAFA1(Q1,Q2,ALPHA)
      CALL GETBTA1(Q1,Q2,BETA)
      CALL GETQ31(ALPHA,BETA,Q3)
      CALL GETQ41(ALPHA,BETA,Q4)
      CALL GETQ51(ALPHA,BETA,Q5)
      CHECK=P1-(Q3*0.5D0)*((P1-P4)/Q4+(P1-P5)/Q5)
      PRINT*, M,' PS =',CHECK


C Check convergence
      ER=CHECK-GUESS
      IF(DABS(ER).LE.LIMIT) THEN
        PS=GUESS
        PT=(P1-PS)/Q3+PS
C Interate
      ELSE
          GUESS=CHECK
          GO TO 3
      ENDIF

      PRINT*, 'CONVERGENCE'
      PRINT*
      RETURN
      END

C Define the GETAFA1 calibration subroutine

      SUBROUTINE GETAFA1(X,Y,Z)
      DOUBLE PRECISION X,Y,Z
      DOUBLE PRECISION C(65+1)
      C(1)=-0.4947922117603512D0
      C(2)=-14.07462149683684D0
      C(3)=1.002798586216142D0
      C(4)=-0.9089782903386343D0
      C(5)=-0.2515175863888643D0

      C(6)=1.721587127162820D0
      C(7)=-0.9042934593837612D0
      C(8)=0.5348059114568949D0
      C(9)=1.266907533831120D0
      C(10)=0.04704325100122424D0
      C(11)=-0.5528558669025064D0
      C(12)=0.09826354216296073D0
      C(13)=1.080145768303006D0
      C(14)=-0.4012782144300249D0
      C(15)=-0.1695283098145600D0
      C(16)=-0.4298104927130132D0
```

```
      C(17)=0.2239804185829672D0
      C(18)=0.5566342158673149D0
      C(19)=0.2463124866362337D0
      C(20)=-1.012878262728827D0
      C(21)=0.2719412003998710D0
      C(22)=-0.3111232864976958D0
      C(23)=0.1333797637042657D0
      C(24)=0.6501657110097862D0
      C(25)=-0.2925679788206455D0
      C(26)=-0.0788138095001405 4D0
      C(27)=-0.2640198045325519D0
      C(28)=0.2443408136292149D0
      C(29)=-0.1586707339103677D0
      C(30)=0.06403538605573093D0
      C(31)=0.3522782715555045D0
      C(32)=-0.007193783134164450D0
      C(33)=-0.3488982537229980D0
      C(34)=0.1374233372595653D0
      C(35)=-0.009487709511147204D0
      C(36)=0.0649829256561 6107D0
      C(37)=-0.1022849428099059D0
      C(38)=0.07998059686845754D0
      C(39)=0.2097873051513047D0
      C(40)=-0.06065075532299433D0
      C(41)=-0.1538672375831830D0
      C(42)=-0.04158385705160976D0
      C(43)=0.1767443643580735D0
      C(44)=-0.1426922359732421D0
      C(45)=0.01601018348666392D0
      C(46)=-0.05209387355661335D0
      C(47)=0.03098027187442168D0
      C(48)=0.1377368940287400D0
      C(49)=-0.02000305255684690D0
      C(50)=-0.1570905187123795D0
      C(51)=0.07704021533890866D0
      C(52)=0.00965945255292 7446D0
      C(53)=0.07770609387969569D0
      C(54)=-0.09186177084551033D0
      C(55)=0.03636580876483153D0
      C(56)=-0.01409911959738719D0
      C(57)=0.00824895174621 4132D0
      C(58)=0.03682068587734224D0
      C(59)=-0.007983614459775487D0
      C(60)=-0.07547515224235249D0
      C(61)=-0.009968370784086921D0
      C(62)=0.08528485658416125D0
      C(63)=-0.04518317936535089D0

      C(64)=0.01206354411750311D0
      C(65)=-0.01345861258767677D0
      C(66)=0.01159181475482130D0
      CALL AFA1(65,0,0,X,Y,C,Z)
      RETURN
      END

C Define the AFA1 calibration subroutine
      SUBROUTINE AFA1(ORDER,LOGX,LOGY,X,Y,C,Z)
      INTEGER ORDER,LOGX,LOG
```

```
      DOUBLE PRECISION X,Y,C(ORDER+1),Z
      INTEGER TCNT,J,M,IV
      DOUBLE PRECISION TX(12),TY(12),V(70),A,B
      A=X
      B=Y
      IF(LOGX.NE.1) THEN
        X=(X-(0.1060700000000000D0))/(0.8188000000000000D0)
      ELSE
          X=(DLOG(X)-(0.0000000000000000D0))/(0.0000000000000000D0)
      ENDIF
      IF(LOGY.NE.1) THEN
        Y=(Y-(0.1018750000000000D0))/(0.7973050000000000D0)
      ELSE
          Y=(DLOG(Y)-(0.0000000000000000D0))/(0.0000000000000000D0)
      ENDIF
      IF(ORDER.EQ.5) THEN
        TCNT=3
      ELSEIF(ORDER.EQ.9) THEN
            TCNT=4
      ELSEIF(ORDER.EQ.14) THEN
            TCNT=5
      ELSEIF(ORDER.EQ.20) THEN
            TCNT=6
      ELSEIF(ORDER.EQ.27) THEN
            TCNT=7
      ELSEIF(ORDER.EQ.35) THEN
            TCNT=8
      ELSEIF(ORDER.EQ.44) THEN
            TCNT=9
      ELSEIF(ORDER.EQ.54) THEN
            TCNT=10
      ELSEIF(ORDER.EQ.65) THEN
            TCNT=11
      ELSE
          Z=0.0D0
          RETURN
      ENDIF
      IF(TCNT.GT.6) THEN
        IF(X.LT.-1.0D0) X=-1.0D0
        IF(X.GT.1.0D0) X=1.0D0
        IF(Y.LT.-1.0D0) Y=-1.0D0
        IF(Y.GT.1.0D0) Y=1.0D0
      ENDIF
      TX(1)=1.0D0
      TY(1)=1.0D0
      TX(2)=X
      TY(2)=Y
      DO 10 J=3,TCNT
         TX(J)=2.0D0*X*TX(J-1)-TX(J-2)
         TY(J)=2.0D0*Y*TY(J-1)-TY(J-2)
   10 CONTINUE
      IV=1
      DO 30 J=1,TCNT
         DO 20 M=J,1,-1
            V(IV)=TX(M)*TY(J-M+1)
            IV=IV+1
   20    CONTINUE
   30 CONTINUE
```

```
      Z=0.0D0
      DO 40 J=1,ORDER+1
         Z=Z+C(J)*V(J)
   40 CONTINUE
      X=A
      Y=B
      RETURN
      END
C Define the GETBTA1 calibration subroutine
      SUBROUTINE GETBTA1(X,Y,Z)
      DOUBLE PRECISION X,Y,Z
      DOUBLE PRECISION C(65+1)
      C(1)=1.464494463796203D0
      C(2)=-0.3639480885788627D0
      C(3)=12.57174599068600D0
      C(4)=0.2021605573995462D0
      C(5)=-0.06679095906494099D0
      C(6)=-0.5772767357252061D0
      C(7)=0.3037723630375943D0
      C(8)=-0.6554932442471144D0
      C(9)=0.5612368125054552D0
      C(10)=-0.3391792063407376D0
      C(11)=0.2667316277376342D0
      C(12)=-0.01697684205109785D0
      C(13)=-0.5770052175537242D0
      C(14)=0.8531813818367191D0
      C(15)=-0.3708153184216640D0
      C(16)=0.1506524581318745D0
      C(17)=-0.1127054388340002D0
      C(18)=-0.1682113090658785D0
      C(19)=-0.2852923501952031D0
      C(20)=0.5838566331528313D0
      C(21)=-0.2258800750450802D0
      C(22)=0.2132137290083969D0
      C(23)=-0.1855590498601526D0
      C(24)=-0.2433022507154371D0
      C(25)=0.2209712002660320D0
      C(26)=-0.1734439008497397D0
      C(27)=0.3411593533049114D0
      C(28)=-0.2051695452391891D0
      C(29)=0.06327770309617324D0
      C(30)=-0.06912535795494032D0
      C(31)=-0.1044990224527455D0
      C(32)=-0.00257412203057671 8D0
      C(33)=0.1605001010286113D0
      C(34)=-0.1942336779733035D0
      C(35)=0.2095927377915376D0
      C(36)=-0.1047733197025534D0
      C(37)=0.1009772166030449D0
      C(38)=-0.1114610779300688D0
      C(39)=-0.06755391690102624D0
      C(40)=0.05634850250914567D0
      C(41)=0.00251506591742678 1D0
      C(42)=0.02923025284860159D0
      C(43)=-0.1198373388189299D0
      C(44)=0.1705132307880497D0
      C(45)=-0.06794525170002242D0
      C(46)=0.01025714200695684D0
```

```
      C(47)=-0.006295986288742057D0
      C(48)=-0.04151410453110352D0
      C(49)=0.00204101384850054 4D0
      C(50)=0.00207256203806179 3D0
      C(51)=-0.02669704046478444D0
      C(52)=0.02010237761017030D0
      C(53)=-0.04253796751112192D0
      C(54)=0.1001171698606914D0
      C(55)=-0.03363624378966472D0
      C(56)=0.03838743609783978D0
      C(57)=-0.04239787461602097D0
      C(58)=-0.02117001167549666D0
      C(59)=0.02069454531659663D0
      C(60)=0.01317674629786139D0
      C(61)=-0.02186992287945034D0
      C(62)=0.01434565068310362D0
      C(63)=0.02104150343058827D0
      C(64)=-0.03409026187940914D0
      C(65)=0.03553325214485656D0
      C(66)=-0.03297290436033017D0
      CALL BTA1(65,0,0,X,Y,C,Z)
      RETURN
      END

C Define the BTA1 calibration subroutine
      SUBROUTINE BTA1(ORDER,LOGX,LOGY,X,Y,C,Z)
      INTEGER ORDER,LOGX,LOGY
      DOUBLE PRECISION X,Y,C(ORDER+1),Z
      INTEGER TCNT,J,M,IV
      DOUBLE PRECISION TX(12),TY(12),V(70),A,B
      A=X
      B=Y
      IF(LOGX.NE.1) THEN
        X=(X-(0.1060700000000000D0))/(0.8188000000000000D0)
      ELSE
          X=(DLOG(X)-(0.0000000000000000D0))/(0.0000000000000000D0)
      ENDIF
      IF(LOGY.NE.1) THEN
        Y=(Y-(0.1018750000000000D0))/(0.7973050000000000D0)
      ELSE
          Y=(DLOG(Y)-(0.0000000000000000D0))/(0.0000000000000000D0)
      ENDIF
      IF(ORDER.EQ.5) THEN
        TCNT=3
      ELSEIF(ORDER.EQ.9) THEN
            TCNT=4
      ELSEIF(ORDER.EQ.14) THEN
            TCNT=5
      ELSEIF(ORDER.EQ.20) THEN
            TCNT=6
      ELSEIF(ORDER.EQ.27) THEN
            TCNT=7
      ELSEIF(ORDER.EQ.35) THEN
            TCNT=8
      ELSEIF(ORDER.EQ.44) THEN
            TCNT=9
      ELSEIF(ORDER.EQ.54) THEN
            TCNT=10
```

```
      ELSEIF(ORDER.EQ.65) THEN
            TCNT=11
      ELSE
          Z=0.0D0
          RETURN
      ENDIF
      IF(TCNT.GT.6) THEN
        IF(X.LT.-1.0D0) X=-1.0D0
        IF(X.GT.1.0D0) X=1.0D0
        IF(Y.LT.-1.0D0) Y=-1.0D0
        IF(Y.GT.1.0D0) Y=1.0D0
      ENDIF
      TX(1)=1.0D0
      TY(1)=1.0D0
      TX(2)=X
      TY(2)=Y
      DO 10 J=3,TCNT
         TX(J)=2.0D0*X*TX(J-1)-TX(J-2)
         TY(J)=2.0D0*Y*TY(J-1)-TY(J-2)
   10 CONTINUE
      IV=1
      DO 30 J=1,TCNT
         DO 20 M=J,1,-1
            V(IV)=TX(M)*TY(J-M+1)
            IV=IV+1
   20    CONTINUE
   30 CONTINUE
      Z=0.0D0
      DO 40 J=1,ORDER+1
         Z=Z+C(J)*V(J)
   40 CONTINUE
      X=A
      Y=B
      RETURN
      END
C Define the GETQ31 calibration subroutine
      SUBROUTINE GETQ31(X,Y,Z)
      DOUBLE PRECISION X,Y,Z
      DOUBLE PRECISION C(65+1)
      C(1)=0.9234909571243205D0
      C(2)=0.002386212161812133D0
      C(3)=-0.01758809515937948D0
      C(4)=-0.01629373488144844D0
      C(5)=-0.0008749045103179078D0
      C(6)=-0.01632480377421287D0
      C(7)=0.00026076866566757 18D0
      C(8)=-0.001797836002805579D0

      C(9)=0.00137082708607678 7D0
      C(10)=-0.00201015609635827 0D0
      C(11)=-0.00063926658783436 07D0
      C(12)=-0.00025158460804063 54D0
      C(13)=-0.00327970497595136 1D0
      C(14)=0.00019573501610448 62D0
      C(15)=-0.00073474526759263 10D0
      C(16)=-0.00037614045682244 94D0
      C(17)=0.00031429345825782 74D0
      C(18)=0.00032687171816172 70D0
```

```
      C(19)=0.00056560809514189540
      C(20)=-7.921954963871735D-05
      C(21)=0.00023851762882725290
      C(22)=0.00028279418701853900
      C(23)=-0.00010569757628233590
      C(24)=0.00054379827968171850
      C(25)=-8.378195190854679D-05
      C(26)=0.00022892883343165100
      C(27)=4.131432021394701D-05
      C(28)=-4.201080365302302D-05
      C(29)=-0.00026209207082290320
      C(30)=-0.00011345442587893140
      C(31)=-0.00014837229043150800
      C(32)=-0.00019790424267917240
      C(33)=-5.434025203832655D-05
      C(34)=-0.00014216643322854150
      C(35)=0.00012745385932536470
      C(36)=-3.643126368134031D-05
      C(37)=0.00016682822405828470
      C(38)=-7.259094525813377D-05
      C(39)=-5.445923273050906D-05
      C(40)=-2.881015065873074D-05
      C(41)=-0.00018305817121181250
      C(42)=9.784079922159035D-05
      C(43)=-0.00010525574336470620
      C(44)=-4.829130045653886D-06
      C(45)=-3.982671060334190D-05
      C(46)=-0.00014378029655957790
      C(47)=7.360321470653733D-05
      C(48)=-0.00015038097082265590
      C(49)=5.302005711996412D-05
      C(50)=-8.560788533359879D-05
      C(51)=-1.159615364676245D-05
      C(52)=6.838099865319695D-05
      C(53)=-0.00016978594111534460
      C(54)=-8.780688275408046D-06
      C(55)=3.095228984906968D-06
      C(56)=0.00016674943283526770
      C(57)=8.095931201137700D-06
      C(58)=-7.017426935541312D-05
      C(59)=-0.00016454642463232880
      C(60)=-6.836517407650457D-05
      C(61)=-2.846627580911882D-06
      C(62)=-0.00021081188847796840
      C(63)=8.988585416270986D-05
      C(64)=-2.851372694264651D-05
      C(65)=-1.463832056564014D-05
      C(66)=0.00012347300704042960
      CALL Q31(65,0,0,X,Y,C,Z)
      RETURN
      END
C Define the Q31 calibration subroutine
      SUBROUTINE Q31(ORDER,LOGX,LOGY,X,Y,C,Z)
      INTEGER ORDER,LOGX,LOGY
      DOUBLE PRECISION X,Y,C(ORDER+1),Z
      INTEGER TCNT,J,M,IV
      DOUBLE PRECISION TX(12),TY(12),V(70),A,B
      A=X
```

```
   B=Y
   IF(LOGX.NE.1) THEN
     X=(X-(0.000000000000000D0))/(12.00000000000000D0)
   ELSE
       X=(DLOG(X)-(0.000000000000000D0))/(0.000000000000000D0)
   ENDIF
   IF(LOGY.NE.1) THEN
     Y=(Y-(1.000000000000000D0))/(12.00000000000000D0)
   ELSE
       Y=(DLOG(Y)-(0.000000000000000D0))/(0.000000000000000D0)
   ENDIF
   IF(ORDER.EQ.5) THEN
     TCNT=3
   ELSEIF(ORDER.EQ.9) THEN
         TCNT=4
   ELSEIF(ORDER.EQ.14) THEN
         TCNT=5
   ELSEIF(ORDER.EQ.20) THEN
         TCNT=6
   ELSEIF(ORDER.EQ.27) THEN
         TCNT=7
   ELSEIF(ORDER.EQ.35) THEN
         TCNT=8
   ELSEIF(ORDER.EQ.44) THEN
         TCNT=9
   ELSEIF(ORDER.EQ.54) THEN
         TCNT=10
   ELSEIF(ORDER.EQ.65) THEN
         TCNT=11
   ELSE
       Z=0.0D0
       RETURN
   ENDIF
   IF(TCNT.GT.6) THEN
     IF(X.LT.-1.0D0) X=-1.0D0
     IF(X.GT.1.0D0) X=1.0D0
     IF(Y.LT.-1.0D0) Y=-1.0D0
     IF(Y.GT.1.0D0) Y=1.0D0
   ENDIF
   TX(1)=1.0D0
   TY(1)=1.0D0
   TX(2)=X
   TY(2)=Y
   DO 10 J=3,TCNT
      TX(J)=2.0D0*X*TX(J-1)-TX(J-2)
      TY(J)=2.0D0*Y*TY(J-1)-TY(J-2)
10 CONTINUE
   IV=1
   DO 30 J=1,TCNT
      DO 20 M=J,1,-1
         V(IV)=TX(M)*TY(J-M+1)
         IV=IV+1
20    CONTINUE
30 CONTINUE
   Z=0.0D0
   DO 40 J=1,ORDER+1
      Z=Z+C(J)*V(J)
40 CONTINUE
```

```
      X=A
      Y=B
      RETURN
      END

C Define the GETQ41 calibration subroutine

      SUBROUTINE GETQ41(X,Y,Z)
      DOUBLE PRECISION X,Y,Z
      DOUBLE PRECISION C(65+1)
      C(1)=0.6015829503293724D0
      C(2)=0.3566024941843957D0
      C(3)=-0.02650957897989382D0
      C(4)=0.005454197969938864D0
      C(5)=-0.002578422852972686D0
      C(6)=-0.05047968060779283D0
      C(7)=-0.007466122341066878D0
      C(8)=-0.003402996923618451D0
      C(9)=0.01298257898201791D0
      C(10)=0.005520393643494750D0
      C(11)=6.754605639881305D-05
      C(12)=0.0004076519792293319D0
      C(13)=0.004902794091352159D0
      C(14)=0.001140201846855865D0
      C(15)=0.01025990405203386D0
      C(16)=-0.0008816205783805175D0
      C(17)=0.001064973248306213D0
      C(18)=-0.001374791035505072D0
      C(19)=-0.002582867246575045D0
      C(20)=-0.007689419696451734D0
      C(21)=-0.002092827117947516D0
      C(22)=0.0008927054838681323D0
      C(23)=0.0003610768490998064D0
      C(24)=2.357557952827548D-05
      C(25)=-0.0008500285363731533D0
      C(26)=-0.001582590088245257D0
      C(27)=0.0008463818445155461D0
      C(28)=-0.002207047179611928D0
      C(29)=-0.0005848393913951134D0
      C(30)=0.0003740607078106732D0
      C(31)=0.0003782681155945040D0
      C(32)=-0.0001619585347891636D0
      C(33)=0.001258010382095577D0
      C(34)=0.001616838704969343D0
      C(35)=0.002945171564198078D0
      C(36)=0.0003277408357333410D0
      C(37)=0.0007072919099651712D0
      C(38)=0.0001149987384101525D0
      C(39)=-0.0001937177806070648D0
      C(40)=6.811070604743140D-05
      C(41)=1.296225535862642D-05
      C(42)=-0.0001700063878623275D0
      C(43)=0.0004432718415233325D0
      C(44)=-0.0008589978395198041D0
      C(45)=0.0005617721544746778D0
      C(46)=-0.0004041858847881445D0
      C(47)=0.0002499588125304835D0
      C(48)=0.0002561203868030188D0
```

```
      C(49)=-0.00012854057820222l0D0
      C(50)=-5.900409403739397D-05
      C(51)=-0.000149359588899418 2D0
      C(52)=-0.000525168826336629 4D0
      C(53)=-0.001008287121607359D0
      C(54)=-0.000936967630807354 7D0
      C(55)=-0.000166533328737540 5D0
      C(56)=4.772438351747833D-05
      C(57)=0.000209150956981851 8D0
      C(58)=0.000125211604582464 2D0
      C(59)=-0.000219205421675362 2D0
      C(60)=0.000249836535923213 9D0
      C(61)=0.000156088021607812 0D0
      C(62)=-0.000330157376546100 0D0
      C(63)=0.000228706988655829 2D0
      C(64)=-9.346849569257237D-05
      C(65)=0.000492824722165186 6D0
      C(66)=-0.000533734126532537 3D0
      CALL Q41(65,0,0,X,Y,C,Z)
      RETURN
      END

C Define the Q41 calibration subroutine
      SUBROUTINE Q41(ORDER,LOGX,LOGY,X,Y,C,Z)
      INTEGER ORDER,LOGX,LOGY
      DOUBLE PRECISION X,Y,C(ORDER+1),Z
      INTEGER TCNT,J,M,IV
      DOUBLE PRECISION TX(12),TY(12),V(70),A,B

      A=X
      B=Y
      IF(LOGX.NE.1) THEN
        X=(X-(0.000000000000000D0))/(12.00000000000000D0)
      ELSE
          X=(DLOG(X)-(0.000000000000000D0))/(0.000000000000000D0)
      ENDIF
      IF(LOGY.NE.1) THEN
        Y=(Y-(1.000000000000000D0))/(12.00000000000000D0)
      ELSE
          Y=(DLOG(Y)-(0.000000000000000D0))/(0.000000000000000D0)
      ENDIF
      IF(ORDER.EQ.5) THEN
        TCNT=3
      ELSEIF(ORDER.EQ.9) THEN
            TCNT=4
      ELSEIF(ORDER.EQ.14) THEN
            TCNT=5
      ELSEIF(ORDER.EQ.20) THEN
            TCNT=6
      ELSEIF(ORDER.EQ.27) THEN
            TCNT=7
      ELSEIF(ORDER.EQ.35) THEN
            TCNT=8
      ELSEIF(ORDER.EQ.44) THEN
            TCNT=9
      ELSEIF(ORDER.EQ.54) THEN
            TCNT=10
      ELSEIF(ORDER.EQ.65) THEN
```

```
            TCNT=11
         ELSE
             Z=0.0D0
             RETURN
         ENDIF
         IF(TCNT.GT.6) THEN
           IF(X.LT.-1.0D0) X=-1.0D0
           IF(X.GT.1.0D0) X=1.0D0
           IF(Y.LT.-1.0D0) Y=-1.0D0
           IF(Y.GT.1.0D0) Y=1.0D0
         ENDIF
         TX(1)=1.0D0
         TY(1)=1.0D0
         TX(2)=X
         TY(2)=Y
         DO 10 J=3,TCNT
            TX(J)=2.0D0*X*TX(J-1)-TX(J-2)
            TY(J)=2.0D0*Y*TY(J-1)-TY(J-2)
   10    CONTINUE
         IV=1
         DO 30 J=1,TCNT
            DO 20 M=J,1,-1
               V(IV)=TX(M)*TY(J-M+1)
               IV=IV+1
   20       CONTINUE
   30    CONTINUE
         Z=0.0D0
         DO 40 J=1,ORDER+1
            Z=Z+C(J)*V(J)
   40    CONTINUE
         X=A
         Y=B
         RETURN
         END
C Define the GETQ51 calibration subroutine
         SUBROUTINE GETQ51(X,Y,Z)
         DOUBLE PRECISION X,Y,Z
         DOUBLE PRECISION C(60+1)
         C(1)=0.3855913172489723D0
         C(2)=0.3948535699615429D0
         C(3)=-0.01197090644223909D0
         C(4)=0.4313277544247362D0
         C(5)=0.1984927290962567D0
         C(6)=0.2723635793487473D0
         C(7)=0.09005123093615874D0
         C(8)=-0.06213365883958835D0
         C(9)=0.02455330825934042D0
         C(10)=0.00257382120094387 3D0
         C(11)=0.02352244354707 06D0
         C(12)=-0.1062952116952013D0
         C(13)=-0.01938423683057163D0
         C(14)=-0.02464847961289058D0
         C(15)=-0.007076728226756137D0
         C(16)=-0.008925490730165078D0
         C(17)=-0.01198723350007794D0
         C(18)=-0.003371763531054488D0
         C(19)=-0.004057065579427144D0
         C(20)=0.002816146306274347D0
```

```
      C(21)=0.00248303274608541 6D0
      C(22)=0.01017762919065674D0
      C(23)=-0.1181943930588326D0
      C(24)=-0.009149302655458441D0
      C(25)=-0.06389314069957745D0
      C(26)=-0.0007489213651800374D0
      C(27)=-0.006347089218184335D0
      C(28)=0.002921636393052933D0
      C(29)=-0.006654885066818091D0
      C(30)=0.00335707809962479 8D0
      C(31)=0.03170858098237441D0
      C(32)=-0.0009166192421926052D0
      C(33)=0.00734733241168540 9D0
      C(34)=-0.0009211628780123822D0
      C(35)=0.003269910629993158D0
      C(36)=-0.001016111182227205D0
      C(37)=-0.1881635184082286D0
      C(38)=-0.05622338157011206D0
      C(39)=-0.1305940460435432D0
      C(40)=-0.008305552167759665D0
      C(41)=0.01566515591581697D0
      C(42)=1.261518857347943D-05
      C(43)=0.008584020790992765D0
      C(44)=-0.01427648485581545D0
      C(45)=0.03779954261799028D0
      C(46)=-0.006674601573309596D0
      C(47)=0.002929103250012088D0
      C(48)=0.000661057354967379 5D0
      C(49)=-0.003300802266849534D0
      C(50)=-0.05364583586957544D0
      C(51)=-0.006181978276211888D0
      C(52)=0.005262345810640981D0
      C(53)=-0.000515653734330786 1D0
      C(54)=0.000208394755033448 4D0
      C(55)=0.001128740122156783D0
      C(56)=0.013615044993694 19D0
      C(57)=0.002580197374949741D0
      C(58)=0.001385478479881508D0
      C(59)=-0.000726513880807810 6D0
      C(60)=-0.001410407045664493D0
      C(61)=0.002780521542016731D0
      CALL Q51(60,X,Y,C,Z)
      RETURN
      END

C Define the Q51 calibration subroutine

      SUBROUTINE Q51(ORDER,X,Y,C,Z)
      INTEGER ORDER
      DOUBLE PRECISION X,Y,C(ORDER+1),Z
      INTEGER I,SICNT,J,K,M,N1,N2
      DOUBLE PRECISION VX(10),VY(10),V(70),A,B
      A=X
      B=Y
      X=(X-(-12.00000000000000D0))/(7.639437268410977D0)
      Y=(Y-(-11.00000000000000D0))/(7.639437268410977D0)
      IF(X.LT.0.0D0) X=0.0D0
      IF(X.GT.3.14159265358979323846D0) X=3.14159265358979323846D0
```

```
   IF(Y.LT.0.0D0) Y=0.0D0
   IF(Y.GT.3.14159265358979323846D0) Y=3.14159265358979323846D0
   IF(ORDER.EQ.12) THEN
     SICNT=2
   ELSEIF(ORDER.EQ.24) THEN
         SICNT=3
   ELSEIF(ORDER.EQ.40) THEN
         SICNT=4
   ELSEIF(ORDER.EQ.60) THEN
         SICNT=5
   ELSE
       Z=0.0D0
       RETURN
   ENDIF
   J=1
   DO 10 I=1,SICNT
      VX(J)=DCOS(DBLE(I)*X)
      VX(J+1)=DSIN(DBLE(I)*X)
      VY(J)=DCOS(DBLE(I)*Y)
      VY(J+1)=DSIN(DBLE(I)*Y)
      J=J+2
10 CONTINUE
   IF(SICNT.EQ.2) THEN
     M=4
     N1=2
     N2=2
   ELSEIF(SICNT.EQ.3) THEN
         M=6
         N1=2
         N2=4
   ELSEIF(SICNT.EQ.4) THEN
         M=8
         N1=4
         N2=6
   ELSEIF(SICNT.EQ.5) THEN
         M=10
         N1=4
         N2=8
   ENDIF
   V(1)=1.0D0
   K=2
   DO 20 I=1,M
      V(K)=VX(I)
      K=K+1
      V(K)=VY(I)
      K=K+1
20 CONTINUE
   DO 40 I=1,N1
      IF(I.EQ.3) N2=N2-2
      DO 30 J=I,N2
         V(K)=VX(I)*VY(J)
         K=K+1
         IF(J.NE.I) THEN
           V(K)=VX(J)*VY(I)
           K=K+1
         ENDIF
30    CONTINUE
40 CONTINUE
```

```
      Z=0.0D0
      DO 50 J=1,ORDER+1
         Z=Z+C(J)*V(J)
   50 CONTINUE
      X=A
      Y=B
      RETURN
      END
************************************************************************
* This subroutine calculates the density of humid air.                 *
* Input Files : N/A                                                    *
* Output Files: N/A                                                    *
      SUBROUTINE DEN(ATS,APS,RH,RHO)
C define variables, parameters and constants to use
      DOUBLE PRECISION RA,RV,KELVIN,SVP,VPP,DPP,RH,APS,ATS,RHO
      PARAMETER(RA=286.9D0,RV=461.495D0,KELVIN=273.15D0)
C calculate saturation vapor pressure
      SVP=6.1078D0*100.0D0*10.0D0**((7.5D0*(ATS-KELVIN))/
     $    (237.3D0+ATS-KELVIN))
C calculate vapor partial pressure
      VPP=SVP*RH/100.0D0
C calculate dry air partial pressure
      DPP=APS-VPP
C calculate flow density
      RHO=DPP/(RA*ATS)+VPP/(RV*ATS)
      RETURN
      END
************************************************************************
* This subroutine calculates the static temperature.                   *
* Input Files : N/A                                                    *
* Output Files: N/A                                                    *
************************************************************************
      SUBROUTINE TSTAT(ATT,APT,APS,ATS)
C define variables and constants
      DOUBLE PRECISION ATT,ATS,APT,APS,GAMMA
      PARAMETER(GAMMA=1.4D0)
C use ideal gas relationship to calculate the static temperature
      ATS=ATT*(APS/APT)**((GAMMA-1.0D0)/GAMMA)
      RETURN
      END
```

APPENDIX B

Producing Contour plots from numerical simulation files

```
clear all
clc

for i=400:640

    data(:,i-399)=csvread(sprintf('%d.csv',i),6,3);
end


ofile = strcat( 'new1.dat');
fid = fopen(ofile,'w');

fprintf(fid,'zone j=241 i=300\n');  % j=time, i=X
for ii = 1:241 %time
    for jj = 1:300 %X

        fprintf(fid, '%6.2f  %6.2f    %12.2f',jj,ii,data(jj,ii));
        fprintf(fid, '\n');
    end

end

fprintf(fid, '\n');
fclose(fid);
```

APPENDIX C

gamma codes

The following code produced the inlet boundary conditions

```
#include "udf.h"
#include "math.h"

#define PI 3.14159;

DEFINE_PROFILE(inlet_g, thread, position)
{
  real x[ND_ND];        /* this will hold the position vector */
  real y, X0;
  face_t f;
  real tt, tau;    /*time*/

    /*tau=0.01803; /*wake period=S_R/U_w, U_in=14m/2, phi=2.14*/
    tau=0.02445714;
    tt=fmod(CURRENT_TIME,tau);

  begin_f_loop(f, thread)
    {
      F_CENTROID(x,f,thread);
      /*y = x[1];*/

      X0=-0.136447892+6.54*tt; /*bottom of the domain is located at Y=-
0.136447892*/

      if ((x[1]<=0.00125+X0) && (x[1]>=-0.00125+X0)) {

      F_PROFILE(f, thread, position)=0.9;
    }
      else{
        F_PROFILE(f, thread, position)=0;

    }
    }
  end_f_loop(f, thread)
}

DEFINE_PROFILE(inlet_u, thread, position){

  real x[ND_ND];        /* this will hold the position vector */
  real y, X0;
  face_t f;
  real tt, tau;    /*time*/
    tau=0.0244571; /*wake period=S_R/U_w, U_in=19m/2, phi=2.14*/
    tt=fmod(CURRENT_TIME,tau);

  begin_f_loop(f, thread)
    {
      F_CENTROID(x,f,thread);

      X0=-0.136447892+6.54*tt; /*bottom of the domain is located at Y=-
```

```
0.136447892*/

      if ((x[1]<=0.00025+X0) && (x[1]>-0.00025+X0)) {

        F_PROFILE(f, thread, position)=14-2*(1+cos(2*3.1415*(x[1]-
X0)/0.005));
    }
      else{
        F_PROFILE(f, thread, position)=14;
    }
    }
  end_f_loop(f, thread)

}

DEFINE_PROFILE(inlet_v, thread, position){

  real x[ND_ND];        /* this will hold the position vector */
  real y, X0;
  face_t f;
  real tt, tau;    /*time*/
    tau=0.0244571; /*wake period=S_R/U_w, U_in=19m/2, phi=2.14*/
    tt=fmod(CURRENT_TIME,tau);

  begin_f_loop(f, thread)
    {
      F_CENTROID(x,f,thread);

      if ((x[1]<=0.00025+X0) && (x[1]>-0.00025+X0)) {

        F_PROFILE(f, thread, position)=5+3*(cos(2*3.1415*(x[1]-
X0)/0.005));
    }
      else{
        F_PROFILE(f, thread, position)=2;
}
    }
  end_f_loop(f, thread)

}
```

The following code calculates the distance from the closest wall boundary and stores in a User Defined Memory

```
#include "udf.h"
#include "prox.h"

static cxboolean wall_dist_set = FALSE;

DEFINE_ON_DEMAND(set_wall_dist_udm1)
{
#if !RP_HOST

  Domain *domain;
  Thread *t;
  cell_t c;

  if (! wall_dist_set)
  {
     domain = Get_Domain(ROOT_DOMAIN_ID);
     Alloc_Storage_Vars(domain, SV_RTMP_0, SV_NULL);
     Calc_Cell_Wall_Distance_New(domain, SV_RTMP_0);
     thread_loop_c(t,domain)
      {
        begin_c_loop(c,t)
        {
            C_UDMI(c,t,1) = C_TMP0(c,t);
        }
        end_c_loop(c,t)
      }

     wall_dist_set = TRUE;
  }
#endif /* !RP_HOST */
}

DEFINE_ON_DEMAND(reset_udm_1_to_3)
{
#if !RP_HOST

  Domain *domain;
  Thread *t;
  cell_t c;

  domain = Get_Domain(ROOT_DOMAIN_ID);

  thread_loop_c(t,domain)
  {
    begin_c_loop(c,t)
    {
      C_UDMI(c,t,1) = 0.01;
      C_UDMI(c,t,2) = 1;
      C_UDMI(c,t,3) = 1;
    }
    end_c_loop(c,t)
  }
#endif /* !RP_HOST */
  wall_dist_set = FALSE;}
```

The following code produces the streamwise coordinate and stores it UDM4

```
#include "math.h"
#include "mem.h"
#include "prox.h"

enum
{
    k,
    g,
    tau,
    N_REQUIRED_UDS
};

static cxboolean wall_dist_set = FALSE;

real mu(cell_t c, Thread *t){

    real y;
    y=MIN(C_UDMI(c,t,1), 0.008);
    return 0.0256*(y*1000)+0.8144;
}

real sigma(cell_t c, Thread *t){

    real y;
    y=MIN(C_UDMI(c,t,1), 0.008);
    return 0.0419*(y*1000)+0.3638;
}

DEFINE_ON_DEMAND(uds_for_udm4)
{
#if !RP_HOST

  Domain *domain;
  Thread *t;
  cell_t c;
  real xc[ND_ND];
  real a, b, c1, d, AA, BB, CC, XS;
    /*Message("Boooo\n");*/
  domain = Get_Domain(ROOT_DOMAIN_ID);
    /*Message("Ali1\n");*/
  thread_loop_c(t,domain)
  {
      /*Message("Ali\n");*/
    begin_c_loop(c,t)
    {

        C_UDSI(c,t,2)=C_UDMI(c,t,4);
        C_UDSI(c,t,5)=C_UDMI(c,t,1);    /*C_UDSI(c,t,5) is the wall
distance*/
        /*C_UDMI(c,t,5)=C_UDSI(c,t,g)+C_UDSI(c,t,tau);*/

        if (C_UDMI(c,t,4)>=0.33*mu(c,t)){   /*g remains constant after
the location of maximum is met*/

            C_UDSI(c,t,6)=1/(sigma(c,t)*sqrt(2*3.1415));
```

```
        }else{
            C_UDSI(c,t,6)=1/(sigma(c,t)*sqrt(2*3.1415))*exp(-
pow(C_UDMI(c,t,4)/0.33-mu(c,t),2)/(2*sigma(c,t)));
    }
    }
    end_c_loop(c,t)
  }
}
```

The following code stores UDM4 in a user defined scalar for the purpose of facilitating derivation

```
#include "udf.h"
#include "math.h"

#define PI 3.14159;

DEFINE_PROFILE(UDS2_fixed, thread, position)
{
  real x[ND_ND];        /* this will hold the position vector */
  real X0;
  cell_t c;
  face_t f;

  begin_c_loop(c, thread)
    {
      C_CENTROID(x,c,thread);
      /*y = x[1];*/

        C_PROFILE(c, thread, position)=C_UDMI(c,thread,4);
    }
  end_c_loop(c, thread)
}

DEFINE_PROFILE(UDS7_fixed, thread, position)
{
    real x[ND_ND];
    real gmin;
    cell_t c;
    face_t f;

    begin_c_loop(c, thread)
    {
        C_CENTROID(x,c,thread);
            if (C_UDMI(c,thread ,4)<0.207)
                gmin=0;
            else
                gmin=0.1*(1+cos((C_UDMI(c,thread ,4)-0.32)/(0.32-
0.207)*3.1415));

            C_PROFILE(c, thread, position)=gmin*(1-
2/3.1415*atan(C_UDMI(c,thread ,1)*1000));
    }
    end_c_loop(c, thread)
}
```

The following is the main intermittency transport code that includes the source terms and advection terms

```
#include "udf.h"
#include "math.h"
#include "mem.h"
#include "prox.h"

#define domain_ID 10

#define alpha1 0.31
#define alpha2 0.44
#define alpha_inf_star 1
#define alpha_inf 0.52
#define alpha0 0.1111
#define alpha0_star 0.025

#define beta1 0.075
#define beta2 0.0828
#define beta_inf_star 0.09
#define beta_i 0.072

#define sigma_k 2
#define sigma_k1 1.176
#define sigma_k2 1
#define sigma_w 2
#define sigma_w1 2.0
#define sigma_w2 1.168

#define R_beta 8
#define R_k 6
#define R_w 2.95
#define ksi_star 1.5
#define M_t0 0.25   /*Equation 4.92*/
#define kappa 0.4187  /*von karman constant*/
#define C_mu 0.09    /*assuming this is a constant. Use eq 4.50 for non-
constant one*/

#define m 4 /*used in the diffusion term of gamma*/

#define C1 0.57     /*for unsteady frequency of 1.033*/
#define C2 0.80
#define C3 1.00
#define C4 0.85
#define sigma_g 2   /*same as sigma_k*/

#define C_1  0.1  /*used in diffusion and dissipation terms of gamma*/
#define C_3 0.1   /*used in dissipation term of gamma*/

#define Re_xs 55000 /*Reynolds number at the start of transition___From
schob paper*/
#define Re_xe 155000    /*Reynolds number at the end of
transition___From schob paper*/

#define PI 3.14159;

enum
{
```

```
    k,
    g,
    sc2,
    sc3,
    fr,
    N_REQUIRED_UDS
};

/*==================U_inf==================*/
real U_inf(cell_t c, Thread *t){

    real v;
    real x[ND_ND];
    C_CENTROID(x,c,t);

        v=-416.17*pow(C_UDMI(c,t,4),2)+143.47*C_UDMI(c,t,4)+20.592;

    return v;
}
/*==================delta_w==================*/
real delta_w(cell_t c, Thread *t){

    real x[ND_ND];
    real d;
    C_CENTROID(x,c,t);


    d=-
142.11*pow(C_UDMI(c,t,4),3)+8.6075*pow(C_UDMI(c,t,4),2)+30.136*C_UDMI(c,
t,4)-0.3815;

    return d;
}
/*============normalvector==============
real ntvec[2](cell_t c, Thread *t){

    real t[2];
    real xc[ND_ND];

    C_CENTROID(xc,c,t);

    if (xc[0]<0.203640)

        alpha=-98485*pow(xc[0],4)+43152*pow(xc[0],3)-
5454.1*pow(xc[0],2)+426.45*xc[0]-60.113;
    else

        alpha=-500935.89*pow(xc[0],3)+340919.69*pow(xc[0],2)-
75707.54*xc[0]+5510.84;

    t[0]=cos(alpha);
    t[1]=sin(alpha);

return t[2];
}*/

/*==================U_t==================*/
/*========used in gamma source term======*/
```

```
real U_t(cell_t c, Thread *t){

        real Utan, alpha;
        real xc[ND_ND];
        real tg[2]; /* vector */

        alpha=-115650*pow(C_UDMI(c,t,4),6)+119202*pow(C_UDMI(c,t,4),5)-
48092*pow(C_UDMI(c,t,4),4)+9657.5*pow(C_UDMI(c,t,4),3)-
1030.3*pow(C_UDMI(c,t,4),2)+61.845*C_UDMI(c,t,4)-1.4274;

        tg[0]=cos(alpha);
        tg[1]=sin(alpha);


            Utan=C_U(c,t)*tg[0]+C_V(c,t)*tg[1];

return Utan;
}

/*==================f_mu_tau==================*/
/*======used in diffusion term for gamma======*/

real f_mu_tau(cell_t c, Thread *t){

    real h;

    h=1-exp(-256*(C_UDMI(c,t,1)*U_inf(c,t)*C_R(c,t)/C_MU_L(c,t)));  /*
from steelant and Dick article*/

    return h;
}

/*==================fbeta_star==================*/
real fbeta_star(cell_t c, Thread *t){

    real Xk, a;

    /*Equation 4.79*/
    Xk=C_UDMI(c,t,0)/pow(C_O(c,t),3);

    /*Equation 4.78*/
    if (Xk<=0){

         a=1;
    }else{

        a=(1+680*pow(Xk,2))/(1+400*pow(Xk,2));
    }

    return a;
}

/*==================FMt==================*/
real FMt(cell_t c, Thread *t){

    real Mt, a, gamma;

    /*Equation 4.93 and 4.91*/
```

```
    gamma=C_CP(c,t)/(C_CP(c,t)-C_RGAS(c,t));

    a=sqrt(gamma*C_RGAS(c,t)*C_T(c,t));

    Mt= sqrt(2*C_UDSI(c,t,k))/a;

    /*Equation 4.90*/
    if(Mt<=M_t0){

        return 0;
    }else{

        return pow(Mt,2)-pow(M_t0,2);
    }
}

/*==================Ret=================================================
===========*/
real Ret(cell_t c, Thread *t){

    /* Equation 4.69*/
    return C_R(c,t)*C_UDSI(c,t,k)/(C_MU_L(c,t)*C_O(c,t));
}

/*==================F1==================================================
=============*/

real F1(cell_t c, Thread *t){

    /* Equation 4.100 */
    real a,a1,a2,b,d ;

    a1=sqrt(C_UDSI(c,t,k))/(0.09*C_O(c,t)*C_UDMI(c,t,1));
    a2=500*C_MU_L(c,t)/C_R(c,t)/(pow(C_UDMI(c,t,1),2)*C_O(c,t));

    a=MAX((a1),(a2));


b=4*C_R(c,t)*C_UDSI(c,t,k)/(sigma_w2*CD_kw(c,t)*pow(C_UDMI(c,t,1),2));

    d=MIN((a),(b));

    return tanh(d*d*d*d) ;
}

/*==================F2==================================================
=============*/
/*==================F2==================seems not
used*=========================*/
real F2(cell_t c, Thread *t){

    real c1,c2,d1;

    c1=2*sqrt(C_UDSI(c,t,k))/(0.09*C_O(c,t)*C_UDMI(c,t,1));
    c2=500*C_MU_L(c,t)/C_R(c,t)/(pow(C_UDMI(c,t,1),2)*C_O(c,t));

    d1= MAX(c1,c2);
```

```
    return tanh(d1*d1);
}

/*====================F_s================================*/
/*=======================================================*/
real F_s(cell_t c, Thread *t){

    real F1;

    F1=9/3.14159*atan(20*(-C_UDMI(c,t,4)/0.33+0.4))+5.5;

    return F1;
}

/*=============================================================*/
/*============ADJUST==========================================*/
=============================================================*/

DEFINE_ADJUST(adjust, domain){

    Thread *t;
    cell_t c;

    /*domain=Get_Domain(11);*/

    thread_loop_c (t,domain)
    {
        begin_c_loop(c,t){

            /*j*
            C_UDMI(c,t,0)=-100000;
            /*8*

            Message ("here\n");*/
            C_UDMI(c,t,0)=NV_DOT(C_UDSI_G(c,t,k),C_O_G(c,t));

            /*real tg[2]; /* vector
            real alpha;
            real xc[ND_ND];

            C_CENTROID(xc,c,t);

            if (xc[0]<0.203640)

                alpha=-98485*pow(xc[0],4)+43152*pow(xc[0],3)-
5454.1*pow(xc[0],2)+426.45*xc[0]-60.113;
            else

                alpha=-500935.89*pow(xc[0],3)+340919.69*pow(xc[0],2)-
75707.54*xc[0]+5510.84;

            tg[0]=cos(alpha);
            tg[1]=sin(alpha);*
            Message("here is A1\n");
            C_UDMI(c,t,2)=U_t(c,t);

            C_UDSI(c,t,3)=sqrt(pow(C_U(c,t),2)+pow(C_V(c,t),2));
            C_UDMI(c,t,5)=C_UDSI(c,t,1)+C_UDSI(c,t,4);
```

```
            }
            end_c_loop(c,t)
    }
}
/*=====================================================*/
/*=======ADJUST WALL SHEAR/ y+ for suction=============*/
/*=====================================================*/

DEFINE_ADJUST(adjust_ws_yplus_suction, domain){

    cell_t c, c0;
    Thread *t, *t0;

    face_t f;
    real A[ND_ND], y_p;
    int Zone_ID=41;
    real wall_shear_force, area, u_tau;

    t=Lookup_Thread(domain,Zone_ID);

    begin_f_loop(f, t)
    {
        F_AREA(A,f,t);
        area = NV_MAG(A);
        wall_shear_force = NV_MAG(F_STORAGE_R_N3V(f,t, SV_WALL_SHEAR));
        c0 = F_C0(f,t);
        t0 = THREAD_T0(t);
        /*C_UDMI(c0,t0,2)= wall_shear_force/area;*/
        C_UDMI(c0,t0,3)= C_STORAGE_R(f,t, SV_WALL_YPLUS_UTAU);  /*y+*/
/*
        u_tau=pow(C_UDMI(c0,t0,2)/C_R(c0,t0),0.5); /*shear velocity
        C_UDMI(c0,t0,3)=C_U(c0,t0)/u_tau; /*Correct this line*/
    }
    end_f_loop(f, t)
}

/*=====================================================*/
/*=======ADJUST WALL SHEARWALL SHEAR/ y+ for pressure====*/
/*=====================================================*/

DEFINE_ADJUST(adjust_ws_yplus_pressure, domain){

    cell_t c, c0;
    Thread *t, *t0;

    face_t f;
    real A[ND_ND], y_p;
    int Zone_ID=26;
    real wall_shear_force, area, u_tau;

    t=Lookup_Thread(domain,Zone_ID);

    begin_f_loop(f, t)
    {
        F_AREA(A,f,t);
        area = NV_MAG(A);
        wall_shear_force = NV_MAG(F_STORAGE_R_N3V(f,t, SV_WALL_SHEAR));
        c0 = F_C0(f,t);
```

```
        t0 = THREAD_T0(t);
        C_UDMI(c0,t0,2)= wall_shear_force/area;

        C_UDMI(c0,t0,3)= C_STORAGE_R(f,t, SV_WALL_YPLUS_UTAU);  /*y+*/
    }
    end_f_loop(f, t)
}

/*=======================================================*/
/*============SOURCES=====================================*/
/*=======================================================*/

DEFINE_SOURCE(k_source, c, t, dS, eqn)
{
    real source, s1, y_k, beta_star, beta_i_star;

        /* Source term for TKE: Equation 4.74 */
        s1=(C_MU_T(c,t))*pow(C_STRAIN_RATE_MAG(c,t),2);

        /*Dissipation of TKE*/

        /* Equation 4.81*/

beta_i_star=beta_inf_star*(4/15+pow((Ret(c,t)/R_beta),4))/(1+pow((Ret(c,
t)/R_beta),4));

        /* Equation 4.80*/
        beta_star=beta_i_star*(1+ksi_star*FMt(c,t));

        /* Equation 4.77*/
        y_k=C_R(c,t)*beta_star*fbeta_star(c,t)*C_UDSI(c,t,k)*C_O(c,t);

        /*source =s1*(C_UDSI(c,t,g)+1-MAX(C_UDSI(c,t,g)*(1.58*exp(-
pow(C_UDMI(c,t,1)/(delta_w(c,t)/1000),4))-0.59),0))-y_k;*/
        source =s1*MAX(0, C_UDMI(c,t,5));
        dS[eqn] =-C_R(c,t)*beta_star*fbeta_star(c,t)*C_O(c,t);

    return source;
}

DEFINE_SOURCE(g_source, c, t, dS, eqn)
{
        real Pt, Sg1, Sg2, Sg3, Sg4, Yg, diff_coef, X, Y, alpha;
        real gr[2];
        real dSdx, dSdy, dgdS, dg_maxdS, dg_mindS, dg_avgdS, dgdn;
        real xc[ND_ND];
        real tg[2], n[2]; /* vector */
        real tt, tau;    /*time*/
        real b, beta;
        real gmin, gmax;  /*minimum and maximum intermittency*/

        tau=0.0228; /*wake period=S_R/U_w*/
        tt=fmod(CURRENT_TIME,tau);
        b=0.075;        /*wake width*/
        beta=0.160/b;

        if (C_UDMI(c,t,4)<0.207)
```

```
            gmin=0;
        else
            gmin=0.22*(1-exp(-pow((C_UDMI(c,t,4)-0.207)/(0.284-
0.207),2)));

        gmax=0.8*(1-0.25*exp(-pow((C_UDMI(c,t,4)-0.102)/(0.153-
0.102),2)));

        Pt=U_t(c,t)*-2*pow(beta/tau,2)*tt*(gmax-gmin)*exp(-
pow(beta*tt/tau,2));     /*transient term*/

        C_CENTROID(xc,c,t);

        alpha=-115650*pow(C_UDMI(c,t,4),6)+119202*pow(C_UDMI(c,t,4),5)-
48092*pow(C_UDMI(c,t,4),4)+9657.5*pow(C_UDMI(c,t,4),3)-
1030.3*pow(C_UDMI(c,t,4),2)+61.845*C_UDMI(c,t,4)-1.4274;
        tg[0]=cos(alpha);
        tg[1]=sin(alpha);
        n[0]=tg[1];
        n[1]=-tg[0];

diff_coef=C_1*f_mu_tau(c,t)*C_R(c,t)*U_inf(c,t)*delta_w(c,t)/1000*pow(-
log(1-C_UDSI(c,t,g)),(1-m)/m);

gr[0]=(C_U(c,t)*C_DUDX(c,t)+C_V(c,t)*C_DVDX(c,t))/sqrt(pow(C_U(c,t),2)+p
ow(C_V(c,t),2));

gr[1]=(C_U(c,t)*C_DUDY(c,t)+C_V(c,t)*C_DVDY(c,t))/sqrt(pow(C_U(c,t),2)+p
ow(C_V(c,t),2));

Yg=C_3*diff_coef*sqrt(pow(C_U(c,t),2)+pow(C_V(c,t),2))/pow(U_inf(c,t),2)
*(C_UDSI_G(c,t,3)[0]*n[0]+C_UDSI_G(c,t,3)[1]*n[1])*(-
30*pow(C_UDMI(c,t,1),5)/pow(delta_w(c,t)/1000,6))/pow(1+5*pow(C_UDMI(c,t
,1)/(delta_w(c,t)/1000),6),2); /* Dissipation term from Steelant and
Dick*/
            /* second paranthesis is dc/dn and third paranthesis is
d(gamma)/dn*/
        /*Message("Yg= %g\n", Yg);*/

        if (C_UDMI(c,t,4)<0.207)

            dg_mindS=0;
        else
            /*dg_mindS=67.46*(C_UDMI(c,t,4)-0.207)*exp(-
pow((C_UDMI(c,t,4)-0.207)/(0.284-0.207),2));*/
            dg_mindS=0.08*(1+cos((C_UDMI(c,t,4)-0.32)/(0.32-
0.207)*3.1415));
            /*dg_mindS=1.9352*C_UDMI(c,t,4)-0.4299;
            /*dg_mindS=-
4932.3*6*pow(C_UDMI(c,t,4),5)+3900.7*5*pow(C_UDMI(c,t,4),4)-
1019.4*4*pow(C_UDMI(c,t,4),3)+105.74*3*pow(C_UDMI(c,t,4),2)-
3.6505*2*C_UDMI(c,t,4)-0.0051;
            /*dg_mindS=1.9352;*/

        dg_maxdS=153.78*(C_UDMI(c,t,4)-0.102)*exp(-pow(-(C_UDMI(c,t,4)-
0.102)/(0.153-0.102),2));

        dg_avgdS=50*(C_UDMI(c,t,4)-0.104)*exp(-pow(-(C_UDMI(c,t,4)-
```

```
0.104)/(0.189-0.104),2)); /*the constant was 142.22 and 53.148*/

        dgdS=dg_mindS;
        /*dgdS=(dg_maxdS-dg_mindS)*exp(-pow(beta*tt/tau,2))+dg_mindS;

        /*dSdx=25.7073*pow(xc[0],2)-3.2834*xc[0]+1.1841;*/
        dSdx=C_UDSI_G(c,t,2)[0];
        /*if (xc[0]>0.041)

            dSdy=-1440720*pow(xc[1],5)+632695*pow(xc[1],4)-
103812*pow(xc[1],3)+7860.6*pow(xc[1],2)-275.4*xc[1]+5.123;
        else

            dSdy=119.076*xc[1]-3.2334;*/

        dSdy=C_UDSI_G(c,t,2)[1];

            Sg1=C_R(c,t)*C_U(c,t)*dgdS*dSdx;
            Sg2=C_R(c,t)*C_V(c,t)*dgdS*dSdy;

        dgdn=C_UDSI_G(c,t,6)[0]*(-
sin(alpha))+C_UDSI_G(c,t,6)[1]*cos(alpha);

            Sg3=C_R(c,t)*C_U(c,t)*dgdn*C_UDSI_G(c,t,5)[0];
            Sg4=C_R(c,t)*C_V(c,t)*dgdn*C_UDSI_G(c,t,5)[1];
        dS[eqn]=0;

    /*return 0.0*Pt+1*(Sg1+Sg2)+(Sg3+Sg4)*1-Yg;*/
    return
C_R(c,t)*(C_U(c,t)*C_UDSI_G(c,t,7)[0]+C_V(c,t)*C_UDSI_G(c,t,7)[1]);
}

/*================================================*/
/*===============DIFFUSIVITY=====================*/
/*================================================*/

DEFINE_DIFFUSIVITY(k_diff, c, t, eqn){

    real diff;
    real xc[ND_ND];

    C_CENTROID(xc,c,t);

    switch(eqn){

        case k:

            /* Equation 4.66 */
            diff=C_MU_L(c,t)+C_MU_T(c,t)/sigma_k;

            /* the following diff is for SST k omega and not standard K
omega
            diff=(C_MU_L(c,t)+(sigma_k1*F1(c,t)+sigma_k2*(1-
F1(c,t)))*C_MU_T(c,t))/C_R(c, t);
            */
            break;

        case g:
```

```
        /*if (xc[0]>0 && xc[0]<0.246)*/

/*diff=1*MAX(0.1,C_1*f_mu_tau(c,t)*C_R(c,t)*U_inf(c,t)*delta_w(c,t)*pow(
-log(1-C_UDSI(c,t,g)),(1-m)/m));   /*equation 9 from Steelant and Dick
(C_1)*/
                diff=C_R(c,t)*(C_MU_L(c,t)/5+C_MU_T(c,t)/0.23);

        /*else
                diff=0.1;
                /*diff=diff=C_MU_L(c,t)+C_MU_T(c,t)/sigma_g;*/

        /*Message("diff %g\n", diff);*/

            break;
        case fr:

diff=0.0000001;

    }
            return diff;
}
/*============================================================*/
/*============================MU_T============================*/
/*============================================================*/

DEFINE_TURBULENT_VISCOSITY(mu_eddy,c,t){

    real mu_t;
    real alpha_star, d;

    /* Chalmers Report Eq. 64*/
    /* This is the damping function*/
    alpha_star=(alpha0_star+Ret(c,t)/R_k)/(1+Ret(c,t)/R_k);
    d=C_STRAIN_RATE_MAG(c,t)*F2(c,t)/(0.31*C_O(c,t));

    /* Equation 4.67 *
    mu_t=alpha_star*C_R(c,t)*C_UDSI(c,t,k)/C_UDSI(c,t,w);*/
    mu_t=C_R(c,t)*C_UDSI(c,t,k)/C_O(c,t)/MAX(1/alpha_star, d);

    return mu_t;
}
```